NUMERICAL SIMULATIONS OF CURRENT GENERATION AND DYNAMO EXCITATION IN A MECHANICALLY-FORCED, TURBULENT FLOW

by

R. Adam B. Bayliss

A dissertation submitted in partial fulfillment of
the requirements for the degree of

Doctor of Philosophy

(Physics)

at the

UNIVERSITY OF WISCONSIN–MADISON

2006

ACKNOWLEDGMENTS

I would like to thank J. Wright and R. O'Connell for giving me an introduction to the project and MHD computation. M. Nornberg and E. Spence for excellent discussions and a great deal of assistance with the editing of this work. I thank D. Albers and B. Hudson for many useful conversations, though not all about physics. Many thanks to A. Lefkow for her help in negotiating the "system" and its pitfalls. C. Sovenic, E. Zweibel, C. Hegna, S. Prager, and P. Terry for their excellent teaching and helpful dialogue. C. Forest for his guidance without which none of this would be possible. Most of all I would like to thank C. Johll for his support and concern in helping me through this rewarding but arduous task.

DISCARD THIS PAGE

TABLE OF CONTENTS

DISCARD THIS PAGE

LIST OF FIGURES

Figure Page

NUMERICAL SIMULATIONS OF CURRENT GENERATION AND DYNAMO EXCITATION IN A MECHANICALLY-FORCED, TURBULENT FLOW

R. Adam B. Bayliss

Under the supervision of Assistant Professor Cary B. Forest

At the University of Wisconsin-Madison

The role of turbulence in current generation and self-excitation of a magnetic field has been studied using a three dimensional MHD computation. A simple impeller model drives a flow that can generate a growing magnetic field, depending upon the magnetic Reynolds number $Rm = \mu_0 \sigma V a$ and the fluid Reynolds number $Re = Va/\nu$ of the flow. For $Re < 420$ the flow is laminar and the dynamo transition is governed by a simple threshold in $Rm > 100$, above which a growing magnetic eigenmode is observed that is primarily of a dipole field tranverse to axis of symmetry of the flow. In saturation, the Lorentz force slows the flow such that the magnetic eigenmode becomes marginally stable. For $Re > 420$ and $Rm \sim 100$ the flow becomes turbulent and the dynamo eigenmode is suppressed. The mechanism of suppression is due to a combination of a time varying large-scale flow and the presence of fluctuation-driven currents which effectively enhance the magnetic diffusivity. For higher Rm a dynamo reappears, however the structure of the magnetic field is often different from the laminar dynamo; it is dominated by a dipolar magnetic field which is aligned with the axis of symmetry of the mean-flow, apparently generated by fluctuation-driven currents.

The magnitude and structure of the fluctuation-driven currents has been studied by applying a weak, axisymmetric seed magnetic field to laminar and turbulent subcritical flows. An Ohm's law analysis of the axisymmetric currents allows the fluctuation-driven currents to be identified which show features consistent with predictions from mean field theory. In laminar flow, shear couples with a uniform magnetic field to cause a poloidal current

which give rise to the toroidal magnetic field (the omega-effect) and poloidal flow compresses magnetic flux near the symmetry axis. In turbulent flow, the mean flow is qualitatively similar to the steady state flow in the laminar simulation and features of the laminar fluid limit remain. However, magnetic fields generated by the fluctuations are significant: a dipole moment aligned with the symmetry axis of the mean-flow is generated similar to those observed in the experiment, and toroidal and poloidal flux expulsion are observed.

Cary B. Forest

ABSTRACT

The role of turbulence in current generation and self-excitation of a magnetic field has been studied using a three dimensional MHD computation. A simple impeller model drives a flow that can generate a growing magnetic field, depending upon the magnetic Reynolds number $Rm = \mu_0 \sigma V a$ and the fluid Reynolds number $Re = Va/\nu$ of the flow. For $Re < 420$ the flow is laminar and the dynamo transition is governed by a simple threshold in $Rm > 100$, above which a growing magnetic eigenmode is observed that is primarily of a dipole field tranverse to axis of symmetry of the flow. In saturation, the Lorentz force slows the flow such that the magnetic eigenmode becomes marginally stable. For $Re > 420$ and $Rm \sim 100$ the flow becomes turbulent and the dynamo eigenmode is suppressed. The mechanism of suppression is due to a combination of a time varying large-scale flow and the presence of fluctuation-driven currents which effectively enhance the magnetic diffusivity. For higher Rm a dynamo reappears, however the structure of the magnetic field is often different from the laminar dynamo; it is dominated by a dipolar magnetic field which is aligned with the axis of symmetry of the mean-flow, apparently generated by fluctuation-driven currents.

The magnitude and structure of the fluctuation-driven currents has been studied by applying a weak, axisymmetric seed magnetic field to laminar and turbulent subcritical flows. An Ohm's law analysis of the axisymmetric currents allows the fluctuation-driven currents to be identified which show features consistent with predictions from mean field theory. In laminar flow, shear couples with a uniform magnetic field to cause a poloidal current which give rise to the toroidal magnetic field (the omega-effect) and poloidal flow compresses magnetic flux near the symmetry axis. In turbulent flow, the mean flow is qualitatively similar to the steady state flow in the laminar simulation and features of the laminar fluid

limit remain. However, magnetic fields generated by the fluctuations are significant: a dipole moment aligned with the symmetry axis of the mean-flow is generated similar to those observed in the experiment, and toroidal and poloidal flux expulsion are observed.

Chapter 1

Introduction

Astrophysical and geophysical magnetic fields are generated by complex flows of plasmas or conducting fluids which convert gravitational potential, thermal, and rotational energy into magnetic energy[1, 2]. A comprehensive theory of the magnetohydrodynamic dynamo is elusive since the generating mechanism can vary dramatically from one system to another. The differing mechanisms include the sources of free energy, the conductivity and viscosity of the conducting media, and the geometries. Isolating and understanding the mechanisms by which self-generation occurs, and understanding the role of turbulence in the transition to a dynamo remain important problems.

Dynamo action arises from the electromotive force (EMF) induced by the movement of an electrically-conducting medium through a magnetic field. This motional EMF generates a magnetic field which can either amplify or attenuate the initial magnetic field (depending upon the details of the motion). If the induced field reinforces the initial magnetic field, then the positive feedback leads to a growing magnetic field—a dynamo. The source of energy for this process is the kinetic energy of the moving fluid. The fluid may be driven by many different mechanisms such as thermal convection in a rotating body for the case of the Earth, or by impellers in liquid sodium dynamo experiments.

Turbulence likely plays an important role in the onset and saturated state during the dynamo process and in other current formation in conducting fluids. It is well known that in turbulent fluids, flows can break up into smaller and smaller eddies, a process known as a turbulent cascade. Theories of turbulent MHD predict that in highly conducting fluids,

turbulent currents are produced by small-scale magnetic fields equilibrating with the small-scale eddies in the flow[3]. If the small-scale magnetic fluctuations are helical, the system may undergo an inverse cascade of magnetic helicity from small to large scales. This process may explain observed large-scale magnetic fields[4, 5, 6].

One model for describing the effect of turbulence on current generation is the mean-field theory (MFT), in which magnetic and velocity fields, $\mathbf{B}$ and $\mathbf{v}$, are separated into large-scale, slowly-varying parts associated with mean quantities and small-scale, rapidly-varying parts associated with turbulence. MFT relies on two-scale turbulence, where it is presumed that the length-scales, or time-scales of the turbulent fluctuations are much less than the scales of the mean quantities. The separation of scales allows the magnetic field and flow to be expressed as:

$$\mathbf{B} = \langle \mathbf{B} \rangle + \widetilde{\mathbf{b}} \text{ and } \mathbf{v} = \langle \mathbf{V} \rangle + \widetilde{\mathbf{v}}. \tag{1.1}$$

As is often the convention in MFT, brackets in Eq. 1.1, denote an average over time and the tilde denotes the rms value about the time average. Likewise, the induction equation, Eq. A.17, can be separated into equations for the evolution of the mean magnetic field and fluctuating magnetic field:

$$\frac{\partial \langle \mathbf{B} \rangle}{\partial t} = \nabla^2 \langle \mathbf{B} \rangle + Rm \nabla \times \left[\langle \mathbf{V} \rangle \times \langle \mathbf{B} \rangle + \boldsymbol{\mathcal{E}} \right], \tag{1.2}$$

$$\frac{\partial \widetilde{\mathbf{b}}}{\partial t} = \nabla^2 \widetilde{\mathbf{b}} + Rm \nabla \times \left[\widetilde{\mathbf{v}} \times \langle \mathbf{B} \rangle + \langle \mathbf{V} \rangle \times \widetilde{\mathbf{b}} + \widetilde{\mathbf{v}} \times \widetilde{\mathbf{b}} - \boldsymbol{\mathcal{E}} \right]. \tag{1.3}$$

$\boldsymbol{\mathcal{E}} = \left\langle \tilde{\mathbf{v}} \times \tilde{\mathbf{b}} \right\rangle$ denotes an EMF whereby turbulent fluctuations in the flow and magnetic field interact to drive dynamical variations in the mean large-scale magnetic field. The turbulent flow fluctuations are presumed to be independent of the magnetic field, thus Eq. 1.3 is linear in $\widetilde{\mathbf{b}}$ and can be integrated. The mean turbulent EMF is linear in $\widetilde{\mathbf{b}}$, but also depends on $\langle \mathbf{V} \rangle, \widetilde{\mathbf{v}}, and \langle \mathbf{B} \rangle$. Nonetheless it can also be determined. Alternatively, the turbulent EMF can be expanded about the mean magnetic field using a Taylor expansion in space and time. The induction equation for the mean field, Eq. 1.2 is then substituted for temporal

derivatives. Using index notation:

$$\mathcal{E}_i = \alpha_{ij} \left\langle \mathrm{B} \right\rangle_j + \beta_{ijk} \frac{\partial \left\langle \mathrm{B} \right\rangle_j}{\partial x_k} + ... \tag{1.4}$$

where α_{ij}, β_{ijk} are pseudotensors (thus do not reverse sign under spatial inversions [7]) and depend only on the properties of the flow. The series expansion for $\widetilde{\mathbf{b}}$ employed in Eq. 1.4 converges at low order in $\partial^n \left\langle \mathbf{B} \right\rangle / \partial \mathbf{x}^n$ since the length-scale of the mean field is assumed large. Dividing the α-tensor into symmetric and antisymmetric components, the symmetric component, through helical turbulence, produces currents in the direction of the mean field, while the antisymmetric component, arising from anisotropies in the turbulence, produces currents which reduce the mean field in a manner similar to diamagnetism [8]. A toroidal magnetic field can easily be produced from differential rotation within a toroidal flow (the Ω-effect), however the discovery of the EMF induced via the α_{ij}-term was significant. The α_{ij} term provides a mechanism for the production of poloidal magnetic fields from the toroidal magnetic field. The β_{ijk}-term generally augments the resistive dissipation of the mean magnetic field, however exceptions in which β_{ijk} enhances the mean magnetic field are postulated[1]. For isotropic homogeneous turbulence in a reference frame moving with the mean flow, α_{ij} and β_{ijk} reduce to scalars and induce an EMF of the form

$$\mathcal{E} = \alpha \left\langle \mathbf{B} \right\rangle + \beta \nabla \times \left\langle \mathbf{B} \right\rangle . \tag{1.5}$$

where $\alpha = \left\langle \widetilde{\mathbf{v}} \cdot \widetilde{\boldsymbol{\omega}} \right\rangle \tau_c/3$, $\beta = \left\langle \widetilde{\mathbf{v}}^2 \right\rangle \tau_c/3$, and τ_c is the correlation time of the turbulence. Eq. 1.5 is derived from a direct integration of Eq. 1.3 presuming $\widetilde{\mathbf{b}}$ is induced on scales larger than the resistive dissipation length by a large-scale field[9]. Additionally, if there is significant anisotropy in the turbulence (provided, for instance, by the Coriolis force in a rotating system) the antisymmetric component of α_{ij}, gives rise to an EMF of the form $\boldsymbol{\gamma} \times \left\langle \boldsymbol{B} \right\rangle$ where $\boldsymbol{\gamma} \propto \nabla \widetilde{\mathbf{v}}^2$ [8].

MFT, as presented above, is limited in its scope. The requirement of $\widetilde{\mathbf{b}}$ to be a linear functional of $\left\langle \mathbf{B} \right\rangle$ in the derivation of Eq. 1.4 does not account for the influence of the magnetic field on the flow. As such, the above description is limited to weak magnetic fields.

However, Alfvén waves are induced by a weak mean magnetic field and introduce anisotropy. Thus the flow fluctuations will not satisfy the requirement of being statistically independent of the large scale field (the Alfvén effect [10]). Efforts to extend MFT beyond purely linear solutions of Eq. 1.3 have shown that the feedback of the turbulent EMF on the large-scale magnetic field through helical turbulence may saturate at a relatively low magnitude of the induced magnetic field [11, 12], though the matter is not settled [13]. Additionally the two-scale turbulence requirement is stringent for the formation of a large scale magnetic field via the α term in Eq. 1.5 since the turbulent helical fluctuations must locally reorganize the small-scale magnetic field to directly reinforce the large-scale mean field. Despite its limitations, MFT provides a framework for discussion of the role of turbulence in current generation. For example, in systems with an imposed scale separation (such as in pipe-flow experiments), MFT has been used with great success [14, 15]. Currents induced by turbulence can still be projected in terms of the mean magnetic field and the coefficients of this expansion compared to those predicted in the homogeneous, isotropic, two-scale approach. Turbulence induced EMFs qualitatively predicted by MFT may still be present even when the two-scale requirement is relaxed.

Exact treatment of current generation in electrically-conducting fluids requires solving the MHD equations governing the magnetic and velocity fields:

$$\frac{\partial \mathbf{B}}{\partial t} = \frac{1}{\mu_0 \sigma} \nabla^2 \mathbf{B} + \boldsymbol{\nabla} \times \mathbf{v} \times \mathbf{B} \tag{1.6}$$

$$\rho \left[\frac{\partial \mathbf{v}}{\partial t} + (\mathbf{v} \cdot \boldsymbol{\nabla}) \mathbf{v} \right] = \mathbf{J} \times \mathbf{B} + \rho \nu \boldsymbol{\nabla}^2 \mathbf{v} - \boldsymbol{\nabla} p + \mathbf{F}, \tag{1.7}$$

Here ρ is the density, σ is the conductivity, ν is the viscosity, and p is the pressure. $\mathbf{F}$ is a driving term annotating a plethora of sources of free energy in the flow. For example, when the flow is driven by thermal and compositional buoyancy, the mechanism for magnetic field generation is called a convective dynamo [16]. Alternatively, the energy for the flow and field could come be driven by rotation, as in the Balbus-Hawley mechanism for accretion disks [17]. In experimental liquid-sodium dynamos impellers provide the energy input.

Early dynamo theory focused on solving only Eq. 1.6 in the kinematic dynamo problem where the linear magnetic field stability of prescribed velocity fields was calculated to determine if magnetic field growth was possible[18, 19, 20], often using analytic expressions for the MFT coefficients in Ohm's law. Due to advances in computing power, during the last decade great progress has been made by performing direct numerical simulations (DNS) of dynamos, which simultaneously solve the non-linear MHD equations (Eqns. 1.6 and 1.7). Broadly speaking, these studies break into two separate classes. First, there are global simulations which attempt to model geophysical or astrophysical dynamos such as the Earth and the Sun [21, 22, 23, 24, 25, 26]. These models include as much detail of the physical processes as possible, though not at the resolution sufficient to match actual systems. Second, simplified models are constructed in which the geometry was made simple enough to uniquely identify particular physical effects. These models often use a periodic-box geometry (where spectral calculations can be efficiently carried out) and have been quite useful for understanding generic properties of MHD turbulence [27, 11, 28].

The numerical formulation of the spherical dynamo problem solved in planetary and solar models was influenced by the hydrodynamics community's interest in characterizing the fluid instability between differentially rotating cylinders, called Taylor-Couette flow. Since planetary and stellar conducting regions are presumed to be confined between two spherical boundaries, substantial work already has been done in understanding fluid flow and the formation of boundary layers in the spherical Couette problem[29]. As the rapid appreciation of the linear dynamo problem progressed, the need for fully dynamic solutions of the MHD problem between spheres increased [30]. Some of the first successful models employed to solve the stellar convection problem were developed by and described in G. Glatzmaier's work with spectral methods [21]. These same methods were later applied with striking success to the geomagnetic problem by Glatzmaier and Roberts [22] and also by Kuang and Bloxham [31]. The spectral methods were extended to the incompressible spherical shell problem Couette flow by R. Hollerbach [32].

Perhaps the most impressive of the global simulations of the last decade have been those of the geodynamo. Three-dimensional, time-dependent, dynamically self-consistent numerical models have simulated global-scale, laminar convection and magnetic field generation in a rotating fluid shell [22]. Several different geodynamo models, using very different parameters, have produced qualitatively similar global scale magnetic fields at the surface of the model Earth. They have a westward drift similar to that seen in the geomagnetic field over the last couple of hundred years. Some models spontaneously undergo magnetic dipole reversals on the time scales seen in the Earth's paleomagnetic reversal record.

Despite their success, there are major problems with these numerical simulations. No global convective dynamo simulation has yet been able to afford the spatial resolution required to simulate strongly-turbulent convection, which must exist in the low-viscosity fluid interiors of stars and planets, including the Earth's liquid outer core. All have employed greatly-enhanced eddy-viscosity to stabilize the numerical solutions and thus crudely account for the transport and mixing by the unresolved turbulence. Given these limitations, the fact that the fields appear similar to the geomagnetic field may be fortuitous.

Simplified models have also been used to great effect, often providing insight into the basic processes not possible with the global simulations. The earliest of these models, carried out in a periodic box geometry, demonstrated the existence of an inverse cascade of magnetic energy from small scales to large scales in helical turbulence [27], validating key predictions of earlier analytical work on MHD turbulence theory [3, 33]. Similar simulations lead to systematic studies of the MFT, in particular, the saturation of the α-effect by increasing the applied magnetic field strength [11]. The anisotropy of MHD turbulence has also been studied [28, 34]. And most recently, the role of the magnetic Prandtl number (quantifying the ratio of magnetic diffusivity to viscosity) on threshold conditions for magnetic field growth has been studied in periodic boxes and cylindrical geometries [35, 36, 37].

The box models are useful for several reasons. First, they are computationally efficient and easy to implement. The equations are solved on a three-dimensional rectangular grid using spectral methods, making a fast Fourier transform possible for each coordinate. Second,

boundary effects are removed by assuming either periodic boundary conditions or frozen-flux conditions. These simulations are particularly good at modeling infinite, homogeneous turbulence, though these conditions are rarely, if ever, realized in actual astrophysical or planetary contexts.

To address the more realistic models of astrophysical turbulence, research has turned to experiments. Early dynamo experiments were constructed of moving solid conductors embedded in a larger stationary conductor[38, 39]. More recently, experiments at Riga[40, 41, 42] and Karlsruhe[43, 44, 15] use pumps to create flows of liquid metal through helical pipes. These experiments are designed to be laminar *kinematic dynamos*, *i.e.* the average velocity field of the liquid metal is designed (through impeller and pipe geometry) to produce a magnetic field instability. The motivation for using liquid metal in the Riga and Karlsruhe experiments is to allow helical flows— topology not possible with solid conductors. Dynamos in simply-connected geometries, where the flow is unconstrained have yet to be demonstrated in an experiment.

The self-excitation threshold of the Riga and Karlsruhe experiments is governed by the magnetic Reynolds number, $Rm = \mu_0 \sigma L V_0$, where L is a characteristic size of the conducting region, and V_0 is the peak speed. The kinematic theory predicts a critical magnetic Reynolds number, Rm_{crit}, for self-excitation such that a dynamo transition is observed when $Rm > Rm_{crit}$ for particular flow geometries. An important result from the Riga and Karlsruhe experiments is that the measured Rm_{crit} at which the dynamo action occurs is essentially governed by the mean velocity field. Turbulence, which is governed by the magnitude of the fluid Reynolds number $Re = V_0 \ell / \nu = (\ell / L)(Rm/Pm)$, where ℓ is the characteristic size of the channel constraining the flow and $Pm = 10^{-5}$ for liquid sodium, apparently played little role.

A kinematic theory utilizing only the mean flow neglects the role of fluid turbulence, and in simply-connected dynamo experiments the turbulent fluid motion will be pronounced. According to measurements in hydrodynamic experiments, the turbulent velocity fluctuations scale linearly with the mean velocity such that $\tilde{v} = C \langle V \rangle$. MFT predicts that turbulence can

modify the effective conductivity of the liquid metal. Random advection creates a turbulent or anomalous resistivity governed by the spatial and temporal scales of the random flow. A reduction in conductivity due to turbulent fluctuations was observed at low magnetic Reynolds number in liquid sodium[45]. The scaling of this turbulent resistivity is readily obtained by iterating on the magnetic field in the nonlinearity of Eq. 1.6, and looking at the term that depends on gradients of $\mathbf{B}$. For large Rm in a fluid with homogeneous, isotropic turbulence, the turbulent resistivity is proportional to $\widetilde{v}^2\tau_c = \tilde{v}\ell_v$, and combines with the conductivity of the liquid metal to produce a turbulent conductivity given by:

$$\sigma_T = \frac{\sigma}{1 + CRm\ell_v/L}, \tag{1.8}$$

where ℓ_v is a characteristic eddy size (presumed to be some fraction of L). Whereas MFT makes assumptions regarding the specific scale separation between mean quantities and turbulence, the turbulent resistivity, as described above, operates even if there is no clear scale separation, or if mean quantities are not zero. The turbulent conductivity should be used for estimating the dynamo threshold: $Rm = \mu_0\sigma_T V_0 L > Rm_{crit}$ results in a dynamo. Thus, the onset condition in a turbulent flow is governed by

$$Rm > \frac{Rm_{crit}}{1 - C\ell_v Rm_{crit}/L}. \tag{1.9}$$

Note that the potentially singular denominator imposes a requirement on the effectiveness of a particular flow pattern for self-excitation; dynamos will only occur if $Rm_{crit} < \frac{L}{C\ell_v}$.

The small Pm of liquid metals implies large fluctuation levels and a turbulent conductivity. The influence of turbulent conductivity on self-excitation enters through the dimensionless number $CRm_{crit}\ell_v/L$. Through fluid constraints, the flow-dependent parameters C, ℓ_v and Rm_{crit} can be manipulated. In the Karlsruhe experiment[46], for example, ℓ_v is set by the pipe dimensions, rather than the device size hence ℓ_v/L can be taken to be a fraction of the ratio of the pipe dimensions to the device size. An upper bound would be $\ell_v/L = 0.06$. We take $C < 0.1$, and $Rm_{crit} \sim 40$, hence $CRm_{crit}\ell_v/L < 0.24$. We expect therefore that dynamo onset would be governed mainly by laminar predictions, as found experimentally.

Turbulence will likely play a much greater role in governing self-excitation in geophysical and solar dynamos since there are no boundaries to keep small-scale flow from influencing the conducting region and due to the extremely low values of Pm in the Earth's core and in the convection zone of the Sun ($Pm \sim 10^{-5}$ to 10^{-6} and 10^{-7} respectively)[16, 47]. This is also likely to be the case in several experiments now underway which investigate magnetic field generation in more turbulent configurations [48, 49]. One such experiment, at the University of Wisconsin - Madison, uses two impellers in a 1 m diameter spherical vessel, to generate flows (with $\langle V \rangle >$ 15 ms^{-1}). These flows are predicted by laminar theory to be dynamos. [50] The Madison experiment is expected to achieve $Rm > 150$ which exceeds Rm_{crit} by a factor of two. Such experiments have prompted a number of theoretical investigations into whether magnetic field generation is possible for the small Prandtl numbers of liquid metals in experiments without a mean flow[37, 35].

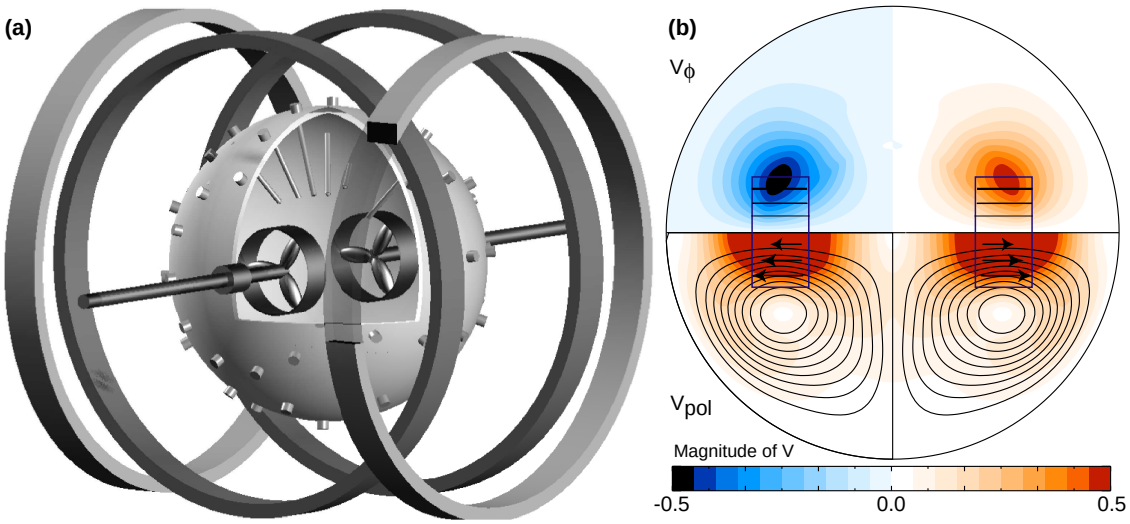

Figure 1.1 (a) a schematic of the Madison Dynamo Experiment. The sphere is 1 m in diameter and filled with 105–110 °C liquid sodium. High speed flows are created by two counter rotating impellers. Two sets of coils, one coaxial and one transverse to the drive shafts, are used to apply various magnetic fields for probing the experiment. (b) contours of the toroidal velocity v_ϕ and contours of the poloidal flow stream function, Φ, where $\mathbf{v}_{pol} = \nabla\Phi \times \nabla\phi$, of the axisymmetric double vortex flow generated by the impeller model. The region of forcing is shown schematically along the symmetry axis.

In this thesis, 3-D direct numerical simulations of the spherical dynamo experiment at the University of Wisconsin are reported. The Madison Dynamo Experiment uses a simple two vortex flow which, according to a laminar kinematic theory, produces a transverse dipole magnetic field. The experiment presents a unique opportunity to test the numerical models: the spherical geometry makes it particularly well-suited to being simulated, and the magnetic fields, at the Rm of the experiment, can be fully resolved, though the fluid turbulence, at the values of Re of the experiment, cannot be fully resolved by simulation. For example, in homogeneous isotropic turbulence [51], it is necessary to resolve scales where energy damped through viscosity is equal to inertial transport occuring at $L_\nu \sim L_0 Re^{-3/4}$. Yet, for a fluid Reynolds number of $O(10^7)$ this would require length scales from the size of the experiment down to micrometers to be resolved. Assuming a rough correspondence between spectral mode number and wavenumber, L^{-1}, 10^{15} spectral modes would be required, wildly exceeding the capabilities of the world's largest computers. While the experimental flow cannot be fully resolved via a direct numerical simulation, the simulations can be used to predict signals measured in the experiment and allow comparisons not possible between geodynamo codes and Earth observations.

Described in Chapter 2, two key features distinguish the present MHD model from other simulations, and firm the link between the simulation and the experiment: forcing and the resolution of flows and magnetic fields through the origin. In the geodynamo, forcing is prescribed by rotation of the boundaries, temperature gradients, and gravity, the respective roles of which cannot be fully ascertained due to imprecision in measurements. In the Madison Dynamo Experiment the boundary is stationary, gravity plays little role in determining the flow and the temperature is constant, thus to the extent the impellers can be numerically represented, the experiment and simulation can directly compared. Much computational effort was made to produce a similar flow to the impellors with a consistent treatment of fluid dynamics. Many models simulate spherical Couette flow, however, the experiment has no inner sphere so using a geodynamo code was ruled out and a means of resolving flow through the origin of a sphere was developed.

The simulated flow is qualitatively similar to the experimental flow and therefore provides an excellent model for investigating dynamo self-excitation in laminar and turbulent regimes. Chapter 4 describes results from $Pm \sim 1$ simulations where the flow is laminar which shows the growth, and saturation of the magnetic field and the mechanism by which the saturation occurs.

As mentioned above, the assertion that this experimental setup will result in a dynamo is based on an extrapolation from linear theory. It is important to determine how the mean flow driven dynamo instability is affected by the presence of turbulence. Producing a growing magnetic field in turbulent flow, and subsequently observing the mechanism which ceases growth will be important results for the experiment. Chapter 5 describes simulations at lower Pm where the flows become turbulent. Results show that the threshold for magnetic excitation increases with flow fluctuations which is consistent with the turbulent conductivity predicted by MFT.

The magnetic configuration of the saturated turbulent-dynamo varies wildly making the calculation of the mean magnetic field in Eq. 1.1 dynamically varying and unsuited to MFT. A more direct test of MFT can be done when the large-scale magnetic field is applied. Chapter 6 presents simulations from applying a uniform magnetic field to the turbulent flow which show a turbulence induced EMF anti-parallel to the applied field.

Chapter 7 provides a summary of the thesis and presents a suggested course for future study.

Chapter 2

Numerical Model

In this section, the numerical model which solves the MHD equations in the experimental geometry is described. This code differs from other codes written to solve the spherical MHD equations since it resolves flow through the origin of the sphere and uses a specially designed drive to simulate the impellers. The driving term used in the simulations that follow is described along with a driving term designed to reproduce exact flow configurations. The experimental parameters motivating the MHD model are discussed and the discretization is presented.

The code addresses salient features of the liquid sodium experiment. Sodium, at 100 °C, is an electrically conducting fluid fully described by the incompressible, resistive, viscous MHD equations. Sodium, as a liquid, is highly collisional. As such, many of the manifestations of MHD dynamics observed in plasmas can be tested in liquid sodium without complications from two-fluid effects or particle dynamics. However, compared to a typical plasma, sodium is a poor conductor. While the resistivity of a typical 1 keV plasma is 2.94×10^{-8} Ωm the resistivity of liquid sodium is roughly 10×10^{-7} Ωm so a 1 keV plasma is roughly 3 times more conducting. Hence, on laboratory scales the resistive term will be important. For instance, the magnetic diffusivity will determine whether, given appropriate conditions, the magnetic field will grow, and how quickly it will grow. Since a slow dynamo evolves on the resistive time-scale, t, is scaled to $\tau_\sigma = \mu_0 \sigma L^2$. The maximum velocity, V_0 is adopted as the characteristic velocity. There are two dissipation mechanisms present in the equations, magnetic and viscous. Their relative importance is expressed by Pm. The fluid is driven at

subsonic speeds. The magnetic energy densities are at most on the order of kinetic energy densities, and the magnetic field, when fully developed, is in rough equipartition with the large scale flows and so Alfvén waves are monitored. The dimensionless equations which govern fluid momentum, magnetic induction, and solenoidal field constraints from Appendix A, Eqns. A.16 and A.17:

$$\frac{\partial \mathbf{v}}{\partial t} + Rm(\mathbf{v}\cdot\boldsymbol{\nabla})\mathbf{v} = -Rm\boldsymbol{\nabla}P + Pm\nabla^2\mathbf{v} + Rm\mathbf{F} + Rm\mathbf{J}\times\mathbf{B}, \tag{2.1}$$

$$\frac{\partial \mathbf{B}}{\partial t} = Rm\boldsymbol{\nabla}\times\mathbf{v}\times\mathbf{B} + \boldsymbol{\nabla}^2\mathbf{B}, \tag{2.2}$$

$$\boldsymbol{\nabla}\cdot\mathbf{v} = \boldsymbol{\nabla}\cdot\mathbf{B} = 0. \tag{2.3}$$

The vector field $\mathbf{F}$ is a stirring term modeling the impellers. Letting the radius of the sphere, $a = 0.55$ m, be the size of the conducting region, $Rm = V_0 a\mu_0\sigma$, and $P_m = \nu\mu_0\sigma$. At $Rm = 100$ then, the speed is roughly 15 ms^{-1}.

Since the fluid is incompressible, the pressure provides an elliptic coupling on the fluid with each fluid element constrained by the rest of the fluid through an infinite sound speed. Other numerical representations of a spherical MHD system solve for the pressure as a constraint on the flow [52], especially in systems like stellar convection zones where compressibility is part of the dynamics. [21] This simulation does not involve an explicit pressure advance and correction on the flow. Instead it solves for the vorticity. However, the elliptic coupling between fluid elements is recovered in the inversion of the curl for the flow. Taking the curl of Eq. 2.1, the expression for the time evolution of the vorticity is,

$$\frac{\partial \boldsymbol{\omega}}{\partial t} = R_m\nabla\times\mathbf{v}\times\boldsymbol{\omega} + R_m\nabla\times\mathbf{J}\times\mathbf{B} + P_m\nabla^2\boldsymbol{\omega} + Rm\nabla\times\mathbf{F}, \tag{2.4}$$

$$\mathbf{v} = (\nabla\times)^{-1}\boldsymbol{\omega}. \tag{2.5}$$

The spectral decomposition is that of Bullard and Gellman, in which the velocity field is described by a spherical harmonic expansion of toroidal and poloidal stream functions [18]

$$\mathbf{v} = \boldsymbol{\nabla}\times(\mathrm{t}\vec{\boldsymbol{r}}) + \boldsymbol{\nabla}\times\boldsymbol{\nabla}\times(\mathrm{s}\vec{\boldsymbol{r}}), \tag{2.6}$$

and the magnetic field is described by an expansion of flux functions

$$\mathbf{B} = \boldsymbol{\nabla}\times(\mathrm{T}\vec{\boldsymbol{r}}) + \boldsymbol{\nabla}\times\boldsymbol{\nabla}\times(\mathrm{S}\vec{\boldsymbol{r}}), \tag{2.7}$$

where s, t, S and T are scalar functions of r, θ , and ϕ. This representation automatically satisfies Eq. 2.3. To decompose Eq. 2.7, each scalar function is projected onto a spherical harmonic basis set, normalized by $N_{\ell,m} = \sqrt{(2\ell+1)(\ell-m)!}/\sqrt{4\pi(\ell+m)!}$: $Y_{\ell,m}(\theta,\phi) = N_{\ell,m}P_\ell^m(\cos\theta)e^{im\phi}$. $Y_{\ell,m}$ is summed from $m = 0, ..., \ell$ and extra factor of $\sqrt{2}$ in $N_{\ell,m}$ for $m \neq 0$ since the flux function represents a real field. The result for the magnetic field is

$$\mathrm{T}(r,\theta,\phi,t) = N_{\ell,m}\sum_{\ell=1}^{\infty}\sum_{m=0}^{m=\ell}\mathrm{T}_{\ell,m}(r,t)P_\ell^m(\cos\theta)e^{im\phi} \tag{2.8}$$

$$\mathrm{S}(r,\theta,\phi,t) = N_{\ell,m}\sum_{\ell=1}^{\infty}\sum_{m=0}^{m=\ell}\mathrm{S}_{\ell,m}(r,t)P_\ell^m(\cos\theta)e^{im\phi} \tag{2.9}$$

and similarly for the flow scalars, t and s.

One advantage of the Bullard-Gellman (BG) representation is that multiple curls, which appear with every poloidal component of the vector fields, reduce to Laplacians. Taking the curl of a general solenoidal vector-field, $\mathbf{W}$, in BG formalism, is represented by two scalar functions of position, e and f. Letting, $\mathbf{W} = \boldsymbol{\nabla}\times\boldsymbol{\nabla}\times e\vec{\boldsymbol{r}} + \boldsymbol{\nabla}\times f\vec{\boldsymbol{r}}$, the curl of $\mathbf{W}$ is

$$\boldsymbol{\nabla}\times\boldsymbol{\nabla}\times g\vec{\boldsymbol{r}} + \boldsymbol{\nabla}\times h\vec{\boldsymbol{r}} = \boldsymbol{\nabla}\times\left[\boldsymbol{\nabla}\times\boldsymbol{\nabla}\times e\vec{\boldsymbol{r}} + \boldsymbol{\nabla}\times f\vec{\boldsymbol{r}}\right]. \tag{2.10}$$

This reduces to a simple relationship between the scalar representation of the curl of the vector field:

$$\begin{aligned} g &= f \\ h &= -\nabla^2 e. \end{aligned} \tag{2.11}$$

To determine the discretized version of the vorticity equations, Eq. 2.4 is expressed in terms of the toroidal-poloidal representation:

$$\boldsymbol{\omega} = \boldsymbol{\omega}_{\mathbf{S}} + \boldsymbol{\omega}_{\mathbf{T}} = \boldsymbol{\nabla}\times\boldsymbol{\nabla}\times\Pi\vec{\boldsymbol{r}} + \boldsymbol{\nabla}\times\Theta\vec{\boldsymbol{r}}. \tag{2.12}$$

Using Eq. 2.11, the equation describing the relationship between vorticity and flow is

$$\Pi = \mathrm{t}, \tag{2.13}$$

$$\Theta = -\nabla^2\mathrm{s}. \tag{2.14}$$

By substituting Eqns. 2.13 and 2.14 into Eq. 2.4, the need to determine boundary conditions on the vorticity is eliminated. The evolution equations for the flow advance become

$$\frac{\partial \Pi}{\partial t} - Pm\nabla^2 \Pi = \frac{\partial \mathrm{t}}{\partial t} - Pm\nabla^2 \mathrm{t} = Rm\,[G]_{\mathbf{S}} + [\boldsymbol{\nabla} \times \mathbf{F}]_{\mathbf{S}} \tag{2.15}$$

$$\frac{\partial \Theta}{\partial t} - Pm\nabla^2 \Theta = \frac{\partial \nabla^2 \mathrm{s}}{\partial t} + Pm\nabla^4 \mathrm{s} = Rm\,[G]_{\mathbf{T}} + [\boldsymbol{\nabla} \times \mathbf{F}]_{\mathbf{T}}\,, \tag{2.16}$$

where G signifies the sum of the advection and Lorentz forces. Since the fourth-order derivative can be computed by consecutive Laplacian operators, the elliptical coupling required by the pressure equation is recovered through the inversion of a Laplacian on s.

The Crank-Nicolson method is used to advance the linear terms. This method implicitly averages the diffusive terms and computes a temporal derivative accurate to second order. The fluid advection term has a hyperbolic character due to the propagation of inertial waves, making it advantageous to use an explicit advancement for nonlinear terms. An explicit second-order Adams-Bashforth predictor-corrector scheme is used to advance the pseudospectral nonlinear terms.

The pseudospectral or collocation method computes a function in real space and then decomposes it in spectral space. Pseudospectral methods avoid the complications of the full-spectral methods which rely on term-by-term integrations of spectral components (such as in the Galerkin method) and in general are much faster than full-spectral methods [53]. The pseudospectral method has the disadvantage of introducing discretization error through aliasing. This error is addressed by padding and truncating the spectrum[53]. When the nonlinearities in the system are quadratic the collocation method the solution produced by the collocation method is formally equivalent to the fully spectral calculation. Since the nonlinear terms in Eqs. 2.1, and 2.2 are quadratic, it is clear that the collocation method will produce the same result as the spectral method.

The discretized form of the modified vorticity equation for a timestep $n+1$, in terms of a predictor step $*$ and previous timestep n, is

$$\begin{aligned}
(\frac{1}{\Delta_t} - P_m\nabla^2)\mathrm{t}^* &= (\frac{1}{\Delta_t} + P_m\frac{\nabla^2}{2})\mathrm{t}^n + \nabla\times\mathbf{F} + [G]_{\mathrm{s}}^{[n,n-1]},\\
-(\frac{\nabla^2}{\Delta_t} - P_m\nabla^4)\mathrm{s}^* &= (\frac{-\nabla^2}{\Delta_t} - P_m\frac{\nabla^4}{2})\mathrm{s}^n + \nabla\times\mathbf{F} + [G]_{\mathrm{t}}^{[n,n-1]},\\
(\frac{1}{\Delta_t} - P_m\nabla^2)\mathrm{t}^{n+1} &= (\frac{1}{\Delta_t} + P_m\frac{\nabla^2}{2})\mathrm{t}^n + \nabla\times\mathbf{F} + [G]_{\mathrm{s}}^{[n,*]},\\
-(\frac{\nabla^2}{\Delta_t} - P_m\nabla^4)\mathrm{s}^{n+1} &= (-\frac{\nabla^2}{\Delta_t} - P_m\frac{\nabla^2}{2})\mathrm{s}^n + \nabla\times\mathbf{F} + [G]_{\mathrm{t}}^{[n,*]},
\end{aligned} \tag{2.17}$$

with the nonlinear terms given by

$$G_{\mathrm{s}}^{[n,n-1]} \equiv \frac{3}{2}\big(\boldsymbol{\nabla}\times\mathbf{v}\times\boldsymbol{\omega}\big)_{\mathrm{s}}^{n} - \frac{1}{2}\big(\boldsymbol{\nabla}\times\mathbf{v}\times\boldsymbol{\omega}\big)_{\mathrm{s}}^{n-1} + \frac{3}{2}\big(\boldsymbol{\nabla}\times\mathbf{J}\times\mathbf{B}\big)_{\mathrm{s}}^{n} - \frac{1}{2}\big(\boldsymbol{\nabla}\times\mathbf{J}\times\mathbf{B}\big)_{\mathrm{s}}^{n-1} \tag{2.18}$$

$$G_{\mathrm{s}}^{[*,n]} \equiv \frac{1}{2}\big(\boldsymbol{\nabla}\times\mathbf{v}\times\boldsymbol{\omega}\big)_{\mathrm{s}}^{*} + \frac{1}{2}\big(\boldsymbol{\nabla}\times\mathbf{v}\times\boldsymbol{\omega}\big)_{\mathrm{s}}^{n} + \frac{3}{2}\big(\boldsymbol{\nabla}\times\mathbf{J}\times\mathbf{B}\big)_{\mathrm{s}}^{*} - \frac{1}{2}\big(\boldsymbol{\nabla}\times\mathbf{J}\times\mathbf{B}\big)_{\mathrm{s}}^{n}. \tag{2.19}$$

The radial derivatives in the diffusive terms are computed through finite differencing on a nonuniform mesh derived in Appendix B. The finite difference coefficients for the ∇^2 and ∇^4 operators result in a nonsymmetric band diagonal matrix. The boundary conditions are folded into the matrix defined by the implicit linear operators with Gauss-Jordan reduction to ensure the matrix remains band-diagonal for ease of inversion. Using an optimized LU decomposition, the radial evolution is solved independently for each spectral harmonic. The scalar fields are then converted to real space and the nonlinear cross products are updated during predictor and corrector steps.

The temporal evolution loops over a spectral harmonic index, thus individual boundary conditions for the respective harmonics are separately applied. The highest-order radial derivative in Eq. 2.17 is fourth order, requiring four boundary conditions on the poloidal flow scalar. Since the velocity must permit a uniform flow through the origin, coordinate regularity implies, from Appendix C, Eqns. C.21 and C.22 imply:

$$\begin{aligned}
\mathrm{s}(r=0),\ \mathrm{t}(r=0),\ \frac{\partial \mathrm{s}(r=0)}{\partial r} = 0 \quad &\text{for } \ell \neq 1\\
\mathrm{s}(r=0),\ \mathrm{t}(r=0),\ \frac{\partial^2 \mathrm{s}(r=0)}{\partial r^2} = 0 \quad &\text{for } \ell = 1.
\end{aligned} \tag{2.20}$$

For better numerical stability, the more stringent requirement s, $\mathrm{t} \to r^{\ell}$ as $r \to 0$ is applied to turbulent simulations.

The other boundary conditions are given by assumptions of a solid, no-slip boundary. For the poloidal flow Appendix C, Eq. C.16 and C.17 are:

$$\mathrm{s}_{\ell,m}(a) = 0, \tag{2.21}$$

$$\frac{\partial \mathrm{s}_{\ell,m}(a)}{\partial r} = 0. \tag{2.22}$$

While for the toroidal flow Appendix C, Eq. C.18 shows:

$$\mathrm{t}_{\ell,m}(a) = 0. \tag{2.23}$$

The discretization of the induction equation is straightforward in light of the method presented for the flow. Using the magnetic field given by Eq. 2.7, the induction term in Eq. 2.2 is projected into toroidal and poloidal components, grouping toroidal and poloidal contributions. The discretized expressions for the magnetic advance are:

$$\left(\frac{1}{\Delta_t} - \nabla^2\right) \mathrm{T}^{*} = \left(\frac{1}{\Delta_t} + \frac{\nabla^2}{2}\right) \mathrm{T}^{n} + RmN_{\mathrm{T}}^{[n,n-1]}, \tag{2.24}$$

$$\left(\frac{1}{\Delta_t} - \nabla^2\right) \mathrm{S}^{*} = \left(\frac{1}{\Delta_t} - \frac{\nabla^2}{2}\right) \mathrm{S}^{n} + RmN_{\mathrm{S}}^{[n,n-1]}, \tag{2.25}$$

$$\left(\frac{1}{\Delta_t} - \nabla^2\right) \mathrm{T}^{n+1} = \left(\frac{1}{\Delta_t} + \frac{\nabla^2}{2}\right) \mathrm{T}^{n} + RmN_{\mathrm{T}}^{[n,*]}, \tag{2.26}$$

$$\left(\frac{1}{\Delta_t} - \nabla^2\right) \mathrm{S}^{n+1} = \left(\frac{1}{\Delta_t} - \frac{\nabla^2}{2}\right) \mathrm{S}^{n} + RmN_{\mathrm{S}}^{[n,*]}, \tag{2.27}$$

where N is the spectral transform of the inductive term in the BG representation. Coordinate regularity gives the conditions for the magnetic flux functions $\mathrm{S}_{\ell,m}(r=0),\ \mathrm{T}_{\ell,m}(r=0) = 0$.

The highest-order derivative of the magnetic advance is $\mathcal{O}(r^2)$. Given the conditions on the magnetic field at the origin, a boundary condition on the magnetic field is needed at the wall. The outer surface of the Madison Dynamo Experiment is stainless steel, modeled in the simulation as a solid insulating wall. The remaining boundary conditions are solved by matching the poloidal magnetic field to a vacuum field via a magnetostatic scalar potential,

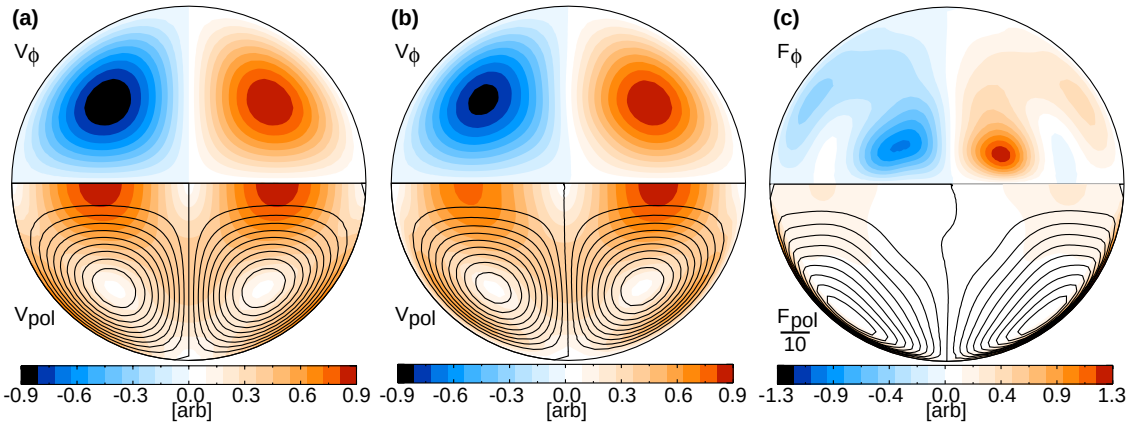

Figure 2.1 (a) A two cell roll flow designed by Dudley *et. al.*[54]. (b) The flow resulting from a fixed force hydrodynamic simulation with $Rm = Re = 100$. (c) The force used in (b).

and noting the toroidal field at the wall must be zero. Appendix C, Eq. C.9 shows

$$\left.\frac{\partial \mathrm{S}_{\ell,m}}{\partial r}\right|_{r=a} + \frac{(\ell+1)}{a}\mathrm{S}_{\ell,m}(a) = A, \tag{2.28}$$

$$\mathrm{T}_{\ell,m}(a) = 0. \tag{2.29}$$

In Eq. 2.28, A=0 if there are no currents in the surrounding medium, but can also be finite to represent a magnetic field applied by external sources.

The timestepping, while unconditionally stable for the diffusive problem, is advectively-limited by an empirically-determined temporal resolution requirement of $\Delta t \leq 5(\Delta x)^2$ for a given spatial resolution. The spectral transform is the most computationally-intensive portion of the code requiring roughly 80% of the CPU time. Due to memory limitations, the upper bound on the spatial resolution is: $N_\theta \sim 64$, $N_\phi \sim 128$, $N_r \sim 400$ which gives, with dealiasing, $\ell_{MAX} = 42$, or nearly 1000 modes.

Two types of driving terms were used in the simulations. The first emphasized matching an exact flow, such as the linearly optimized profile shown in Fig. 1.1 (b). The second relaxed the restriction on reproducing the optimized profile exactly and focused on producing a force more like impellers with the region of forcing confined to a small part of the volume.

To solve for the force required to produce a given flow, an integral drive, derived from the Proportional-Integral-Differential (PID) control algorithm was used. Setting the force to

$$\mathbf{F_I} = G \int_0^{t_0} \boldsymbol{\delta} dt, \tag{2.30}$$

where $\delta = \mathbf{v} - \mathbf{v}_D$ and $\mathbf{v}_D$ is the desired flow. The simulation is started with the fluid at rest and the drive evolves until the simulation reaches a hydrodynamic steady state where:

$$\frac{\partial \boldsymbol{\omega}}{\partial t} = 0 = Rm \nabla \times \mathbf{v} \times \boldsymbol{\omega} + \frac{Rm}{Re} \nabla^2 \boldsymbol{\omega} + Rm \nabla \times \mathbf{F_I'}. \tag{2.31}$$

When the system has reached the steady state, Eq. 2.31), the forcing term is fixed, and the flow is stopped. The system is then driven only with the fixed $\mathbf{F_I'}$ determined from Eq. 2.31. As expected, the system reaches the steady state where:

$$\frac{\partial \boldsymbol{\omega_D}}{\partial t} \;=\; 0 \;=\; Rm \nabla \times \boldsymbol{v_D} \times \boldsymbol{\omega_D} + \frac{Rm}{Re} \nabla^2 \boldsymbol{\omega_D} + Rm \nabla \times \mathbf{F_I'} \tag{2.32}$$

and $\boldsymbol{\omega_D} \;=\; \nabla \times \mathbf{v_D}$. As an example, using a two cell roll flow developed by Dudley *et. al.*[54] shown in Fig. 2.1(a), the force $\mathbf{F_I'}$, was calculated using Eq. 2.32. This force was then fixed and used in a hydrodynamic simulation, the steady state solution of which is shown in Fig. 2.1(b). This driving term, while able to exactly reproduce any physical flow, suffered from two main drawbacks. A hydrodynamic simulation must be undertaken to recompute $\mathbf{F_I'}$ whenever any quantity in Eq. 2.32 is changed or the resolution is altered. The spatial dependence of $\mathbf{F_I'}$ bore little resemblance to a realistic impeller profile, as shown in Fig. 2.1(c).

An alternative forcing method was developed. The forcing term, localized to the location of the impellers in the experiment, drives the flow. The equations governing this forcing term are

$$F_\phi(r,z) \;=\; \rho^2 \sin(\pi \rho b) + \delta \;\; 0.25a < |z| < 0.55\,a, \;\; \rho < 0.3\,a, \tag{2.33}$$

$$F_Z(r,z) \;=\; \epsilon \sin(\pi \rho c) + \gamma, \tag{2.34}$$

where ρ is the cylindrical radius and ϵ, the impeller pitch, changes the ratio of toroidal (F_ϕ) to poloidal (F_Z) force. The constants δ and γ control the axial force, and in this thesis are

zero in all but applied-field runs where stronger axial forcing is useful. The sign of F_Z is positive for $z > 0$ and negative for $z < 0$ creating the counter-rotation between the flow cells. $\mathbf{F}$ is constant, which allows the input impeller power $\mathbf{F} \cdot \mathbf{v}$ to vary. The region of the impellers and an example of the resulting flow are shown in Fig. 1.1. These flows are topologically-similar to the ad hoc flows in several kinematic dynamo studies [54, 55, 20], but are hydrodynamically consistent.

Chapter 3

Benchmarking

This chapter shows how the DYNAMO code was benchmarked against prior work. The numerical formulation of the magnetic field evolution, described by Eq. 2.24 was checked for prescribed flows and in the limit of zero conductivity. The evolution of the flow was tested in a similar fashion to the magnetic benchmarking described below.

The code was first tested for consistency in the truncation and roundoff error of the radial grid and spectral formulation. The finite-difference operators, constructed in Appendix B, were tested on functions with known derivatives. The spectral decomposition was tested by constructing flows and testing the output against the analytically computed decomposition. The pseudospectral operation was checked by using the code to compute $\boldsymbol{\nabla} \times \mathbf{V} \times \boldsymbol{\omega}$ in spectral and real space and comparing to an analytic result.

After checking the differential operators, the code was benchmarked against codes which solve the induction equation as a linear eigenvalue problem with $\mathbf{V}$ given. Taking the reported flows, the flow evolution was turned off and Eq. 2.24 was evolved. For a sequence of Rm with $\mathbf{V}$ fixed, the eigenvalue of the dominant eigenfunction was determined. Fig. 3.1 shows agreement with the results obtained by Dudley *et. al.*[54] for the flow given by:

$$\mathrm{s} = r \sin \pi r Y_{2,0} \tag{3.1}$$

$$\mathrm{t} = 0.14 r \sin \pi r Y_{2,0}. \tag{3.2}$$

and shown in Fig. 2.1. The results of convergence studies for the critical Reynold's number are shown in Table 3.

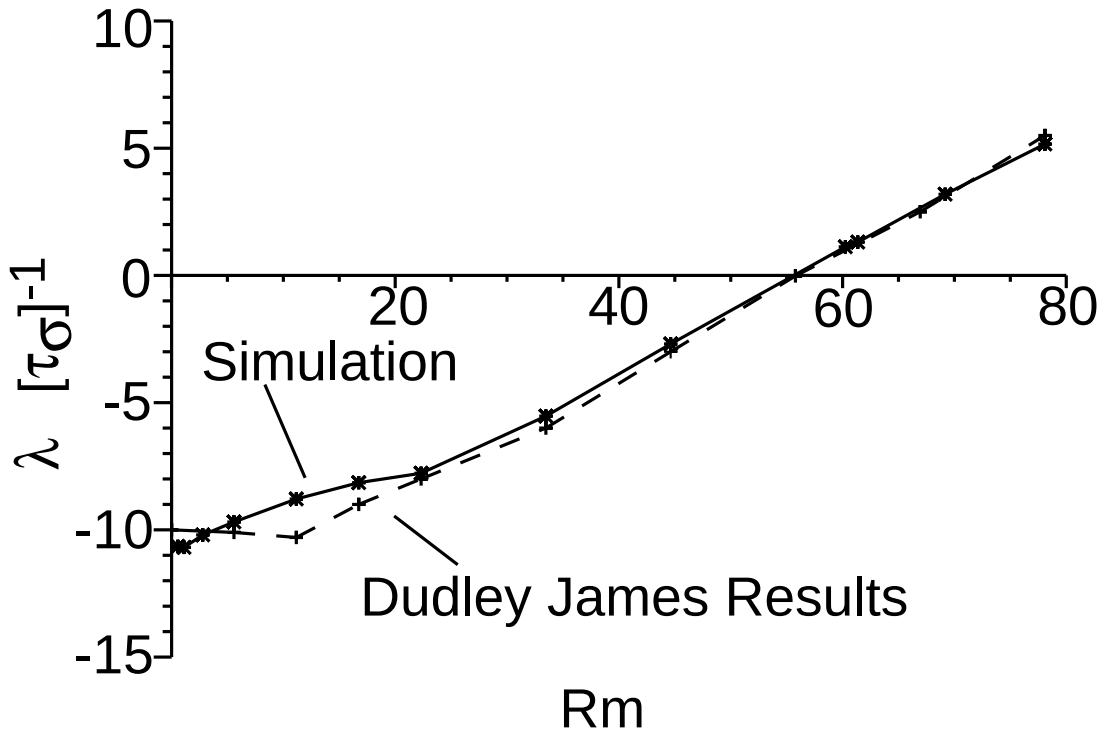

Figure 3.1 The linear growth rates of calculated by the DYNAMO code compared to those reported by Dudley *et. al.* [54].

Benchmark of Critical Reynold's number: $Rm_{crit} = 54$				
Lmax	Nlat	Nlong	Nr	Rm_{crit}
2	4	8	100	70.899
2	10	16	60	70.419
4	6	16	60	50.6412
14	22	32	80	51.6391
14	22	32	80	51.4743∗

Another check on the evolution is afforded by monitoring the conservation of energy through examining the contribution of each dynamic term to power balance. Taking $\mathbf{v} \cdot [Momentum\ Equation]$ and $\boldsymbol{B} \cdot [Induction]$ gives the energy conservation equations for $\boldsymbol{B}$

and $\mathbf{v}$. Integrating the result over an infinite volume

$$\begin{aligned}
\frac{\partial}{\partial t}\int_V d\tau\ \frac{1}{2}B^2 &= -Rm\oint_V d\tau\ \mathbf{v}\cdot(\boldsymbol{J}\times\boldsymbol{B}) - \oint_V J^2, \\
\frac{\partial}{\partial t}\int_V d\tau\ \frac{1}{2}V^2 &= Rm\oint_V d\tau\ \mathbf{v}\cdot(\boldsymbol{J}\times\boldsymbol{B}) - P_m\oint_V d\tau\ \omega^2 \\
&\quad + \oint_V d\tau\ \mathbf{v}\cdot\boldsymbol{F}.
\end{aligned} \tag{3.3}$$

To test the magnetic advancement, the linear resistive magnetic problem, with $\mathbf{v} = 0$, is evolved. Using Eq. 2.2 with a stationary fluid, the evolution equations for the magnetic spectral scalar functions are

$$\tfrac{\partial}{\partial t}\mathrm{S} = \nabla^2\mathrm{S} \tag{3.4}$$

$$\tfrac{\partial}{\partial t}\mathrm{T} = \nabla^2\mathrm{T}, \tag{3.5}$$

which are linear in t. Expanding Eqns. 3.4 and 3.5

$$\mathrm{S} = \sum_{\ell,m} R_{\ell,m}(r)Y_{\ell,m}(\theta,\phi)e^{-\lambda_{\mathrm{S}}t}, \mathrm{T} = \sum_{\ell,m} R'_{\ell,m}(r)Y'_{\ell,m}(\theta,\phi)e^{-\lambda_{\mathrm{T}}t}, \tag{3.6}$$

where λ_{S} and λ_{T} are decay rates. Then Eqns. 3.4 and 3.5 are,

$$-\lambda_{\ell,\mathrm{S}}\mathrm{S}(r,\theta,\phi,t) = \nabla^2\mathrm{S}(r,\theta,\phi,t), \tag{3.7}$$

$$-\lambda_{\ell,\mathrm{T}}\mathrm{T}(r,\theta,\phi,t) = \nabla^2\mathrm{T}(r,\theta,\phi,t). \tag{3.8}$$

Derived in Appendix F, $\lambda_{\ell,\mathrm{S}} = x^2_{\ell,\mathrm{S}}$ and $\lambda_{\ell,\mathrm{T}} = x^2_{\ell,\mathrm{T}}$, where $x_{\ell,\mathrm{S}}$ and $x_{\ell,\mathrm{T}}$ solve $\mathrm{J}_{\ell-\frac{1}{2}}(x) = 0$ and $\mathrm{J}_{\ell+\frac{1}{2}}(x) = 0$ respectively.

Since the decay rate is proportional to the square of the zero of the spherical Bessel function, only the smallest zero, for a given ℓ will be present in the simulation after a diffusive time. These zeros are stated with limited precision in common mathematical handbooks [56], however a root-finding algorithm using Newton's method was written to determine them to more significant digits.

Comparing the analytic calculations of the decay modes to the numerics in Figs. 3.2, and 3.3 shows agreement for small spatial resolution and that error is minimized for the typical

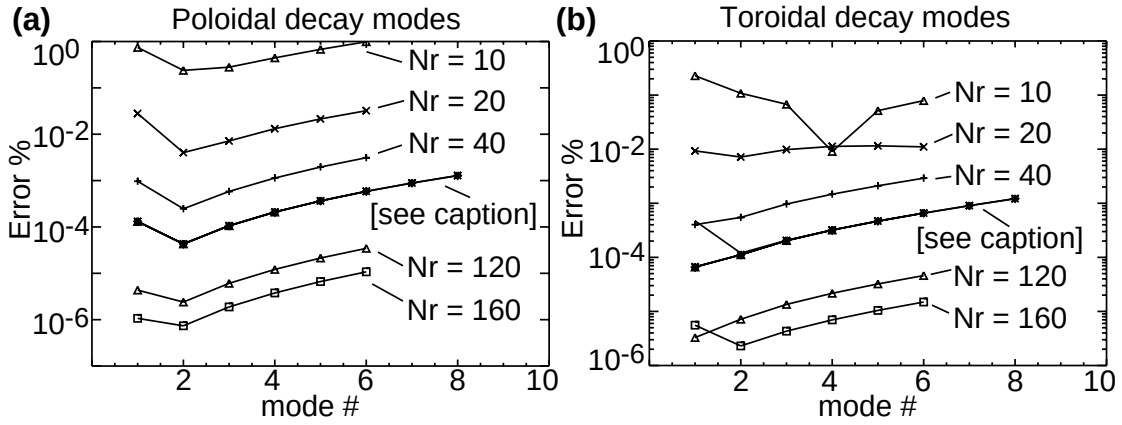

Figure 3.2 Decay modes are computed in purely diffusive runs with fixed timesteps and varying spatial resolution. (a) shows the spatial convergence of poloidal decay modes. Note the black line in the middle is acutually several curves: $(Nr : 60,\ N\theta : 10,\ N\phi : 16)$, $(Nr : 60,\ N\theta : 12,\ N\phi : 32)$, $(Nr : 60,\ N\theta : 20,\ N\phi : 32)$, $(Nr : 80,\ N\theta : 12,\ N\phi : 16)$. The aforementioned line also has a curve with $(Nr : 60,\ N\theta : 10,\ N\phi : 16, L_{MAX} : 8)$ and the increase in the number of Legendre and Fourierr modes has no effect on accuracy in this linear simulation. (b) shows the spatial convergence of toroidal decay modes.

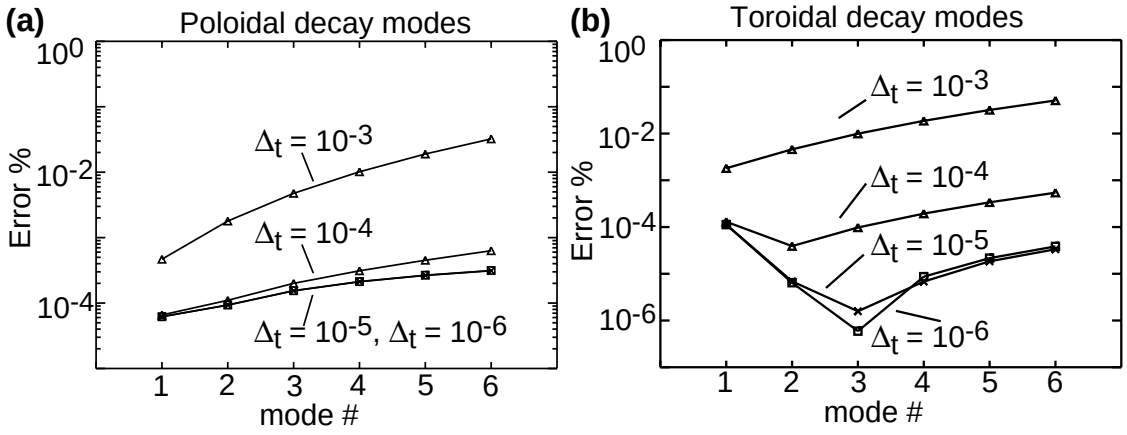

Figure 3.3 Decay modes are computed in purely diffusive runs with differing fixed time-steps. In (a) the temporal convergence of poloidal decay modes is shown for a fixed spatial grid with increasing temporal resolution. (b) shows the temporal convergence of toroidal decay modes.

resolution of linear and nonlinear runs (where $nr \sim 60 - 300,\ n\theta \sim 10 - 32,$ and $n\phi \sim 16 - 128$). The spatial convergence study Fig. 3.2 the increasing accuracy of the finite difference scheme with radial intervals, and that convergence is independent of the number of spherical harmonics used in the spectral representation. While the spectral resolution is important in high Re simulations it is negligible when the nonlinear term is small. Fig. 3.3 is a temporal scan with fixed spatial resolution and shows rapid convergence with decreasing time-steps.

Chapter 4

Laminar Dynamos

Using the impeller model described by Eqns. 2.33 and 2.34 to drive the fluid, analysis is presented from laminar dynamo simulations. By keeping Re low the fluid is hydrodynamically stable and the onset, and $m = 1$ equatorially dominant structure of the dynamo are consistent with kinematic analysis. The effect of the growing magnetic field on the flow as the field becomes large is shown to be a combination of Lorentz braking and increasing the required Rm for the dynamo.

For sufficiently-strong forcing and $Pm \sim 1$, the code, using the impeller model predicts dynamo action, as seen in Fig. 4.1. Starting from a stationary liquid metal, the evolution is observed to go through several phases. Initially, the maximum speed (and Rm) increases from zero to a level at which dynamo action is expected from kinematic theory. The magnetic field energy then increases exponentially with time. The measured growth rate agrees with the growth rate predicted by a kinematic eigenvalue code using the generated velocity fields. After this linear-growth phase, a backreaction of the magnetic field on the flow is observed leading to saturation of the magnetic field. In this saturated state, the generated magnetic field is predominantly a dipole oriented transverse to the symmetry axis, as shown in Fig. 4.6(a). The energy of the first nonaxisymmetric mode ($m = 1$) is plotted in Fig. 4.1(b) showing that the laminar dynamo is entirely nonaxisymmetric.

The orientation of the generated dipole is not constrained by geometry and is observed to vary between simulations. When the saturation state is oscillating, (or damped with

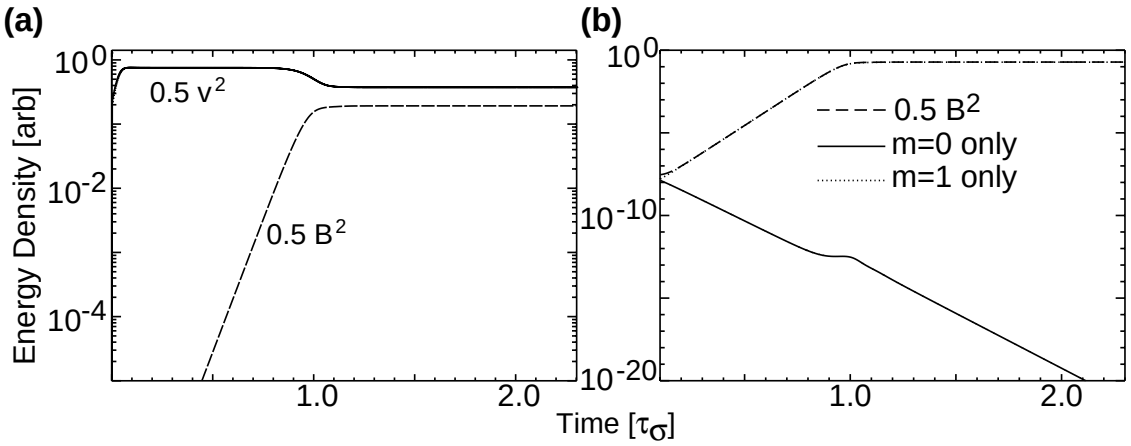

Figure 4.1 (a) The kinetic and magnetic energy densities shown versus time with Rm =159 and $Pm = 1$. The time is in units of the resistive time τ_σ. (b) The contributions to the total magnetic energy density from the $m = 1$ transverse dipole and the axisymmetric $m = 0$ modes.

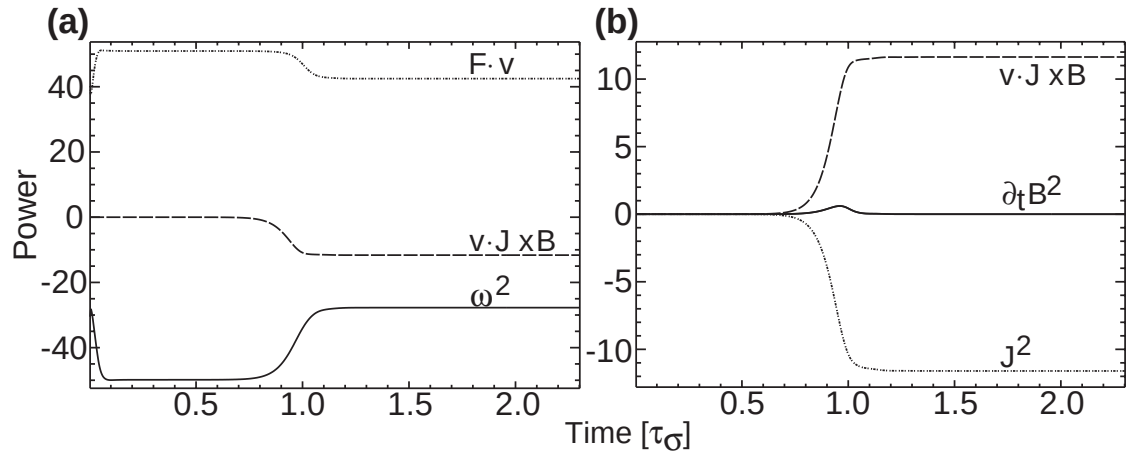

Figure 4.2 For a flow with $Rm = 159$ and $Pm = 1$, (a) The hydrodynamic power, where a constant force balances viscous forces until the growth of the magnetic field changes the flow. Viscous forces are depleted by Lorentz braking and rearrangement of the flow. (b) The magnetic field growth is balanced by resistivity.

oscillations as shown in the $Pm = 0.5$ case in Fig. 5.1) the dipole drifts around the equator and also undergoes 180° reversals.

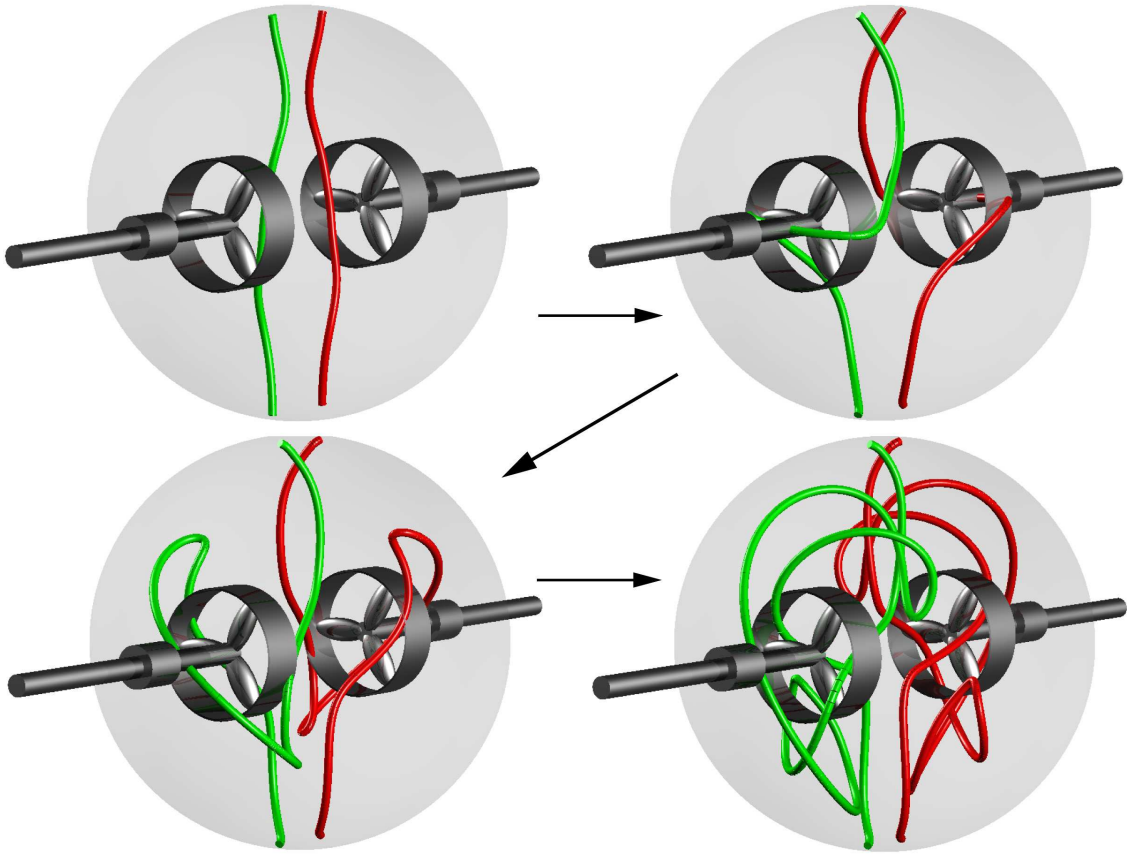

Figure 4.3 The stretch-twist-fold mechanism of field generation in a laminar double-vortex flow is modeled in the frozen flux limit ($Rm \to \infty$). A field line directed through the equator is stretched by the axial flow towards the pole and then twisted back onto itself by the toroidal flow.

Self-excitation depends on the shape of the flow as well as the magnitude of Rm. An ideal ratio of poloidal to toroidal thrust exists (parameterized by ϵ in Eq. 2.34) for which the critical magnetic Reynolds number is minimized as seen in Fig. 4.4.

Minimizing Rm_{crit} makes the flow easier to attain experimentally, This optimal ratio can be understood from a simple frozen flux model describing the stretch-twist-fold cycle of the dynamo, as illustrated in Fig. 4.3 (for an elaboration on the kinematic properties of this flow

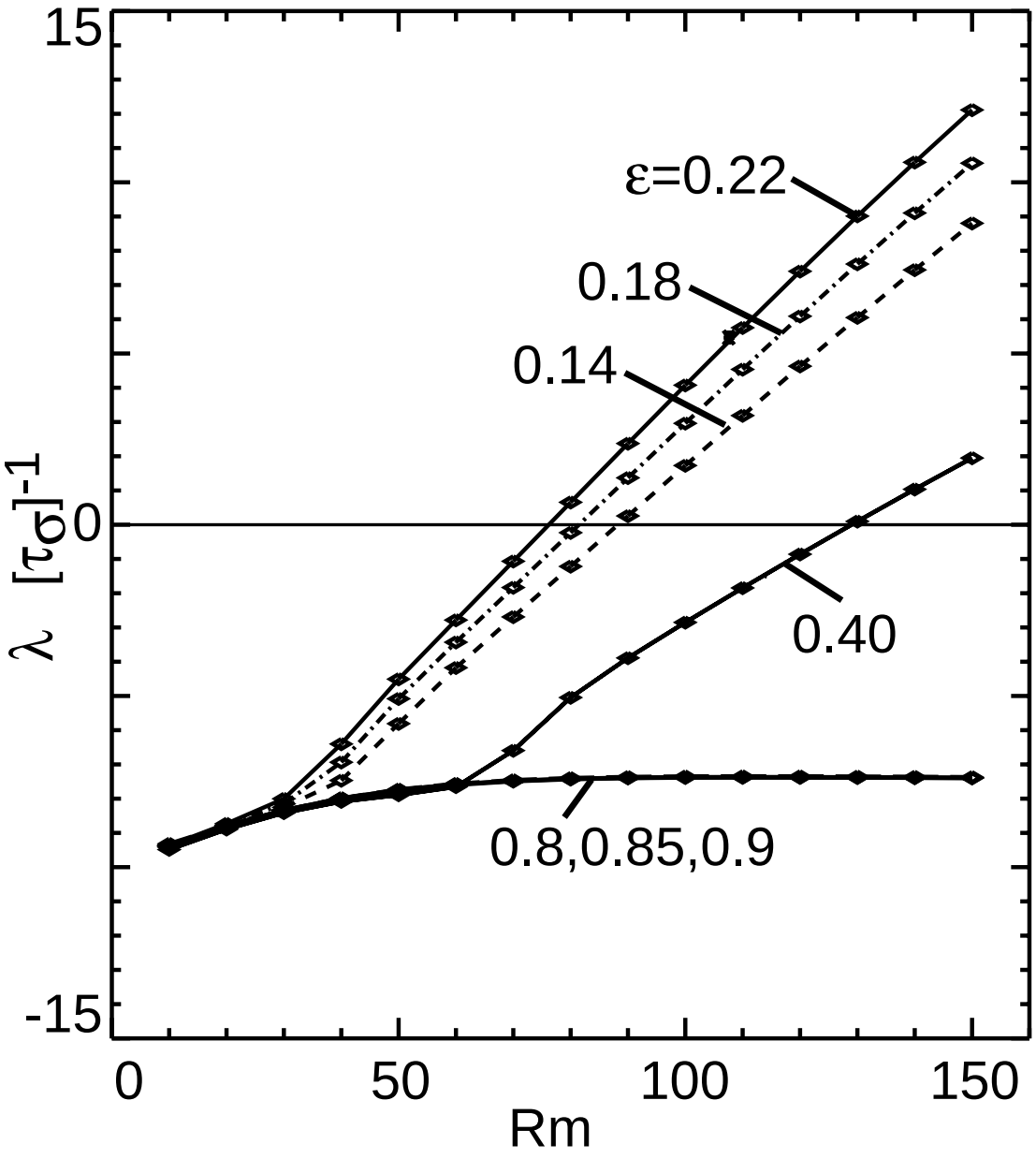

Figure 4.4 The dependance of the linear growth rate of the least-damped magnetic eigenmode on impeller pitch ϵ. The transition from damped to growing ($\lambda = 0$ point) defines the critical magnetic Reynolds number; $Rm < Rm_{crit}$ to a growing magnetic eigenmode.

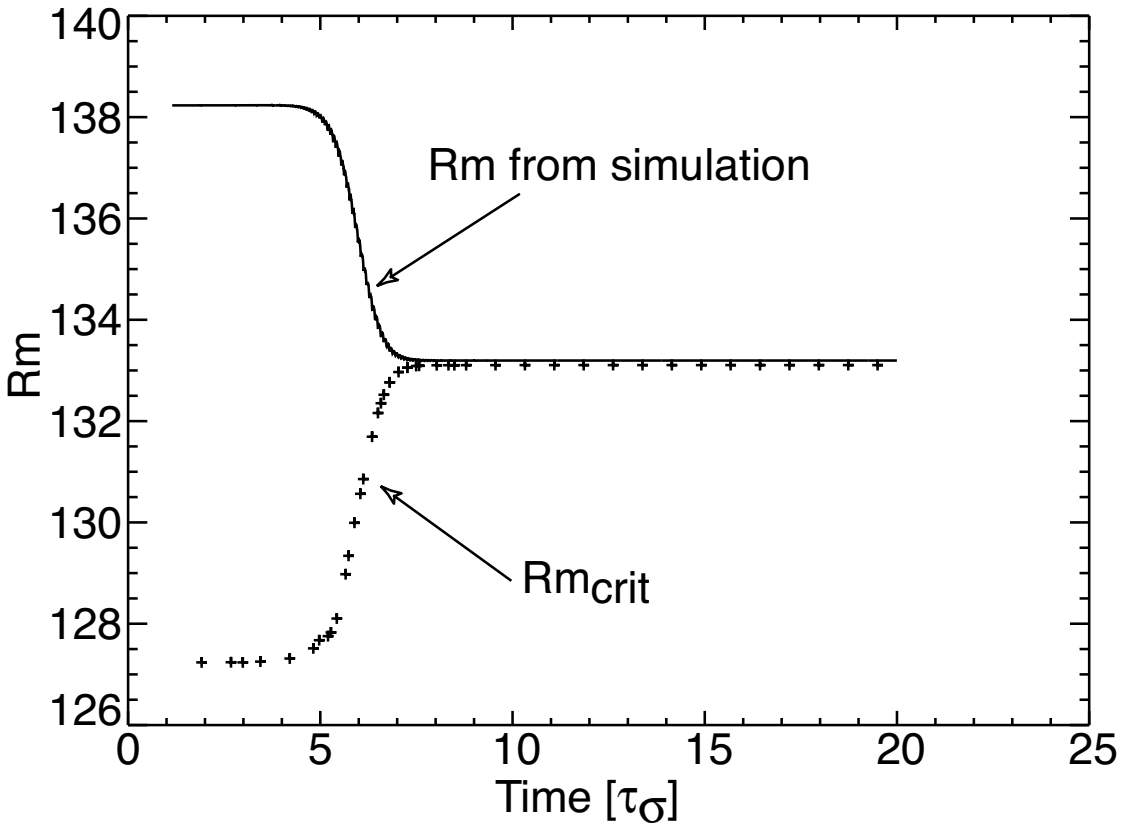

Figure 4.5 Rm and Rm_{crit} evolution during the saturation phase of a laminar dynamo. Rm_{crit} is calculated from linear stability for each velocity field during the simulation. In saturation, $Rm = Rm_{crit}$.

see Ref. [50]). If the toroidal rotation is either too fast or too slow relative to the poloidal flow, the advected field is not folded back on to the initial field.

For laminar flows, the backreaction is the result of two effects. First, an axisymmetric component of the Lorentz force is generated by the dynamo, slowing the flow and reducing Rm. Second, the flow geometry is changed such that the value of Rm_{crit} is increased. In saturation the growth rate is decreased to zero, as the confluence of Rm and Rm_{crit} in Fig. 4.5 shows.

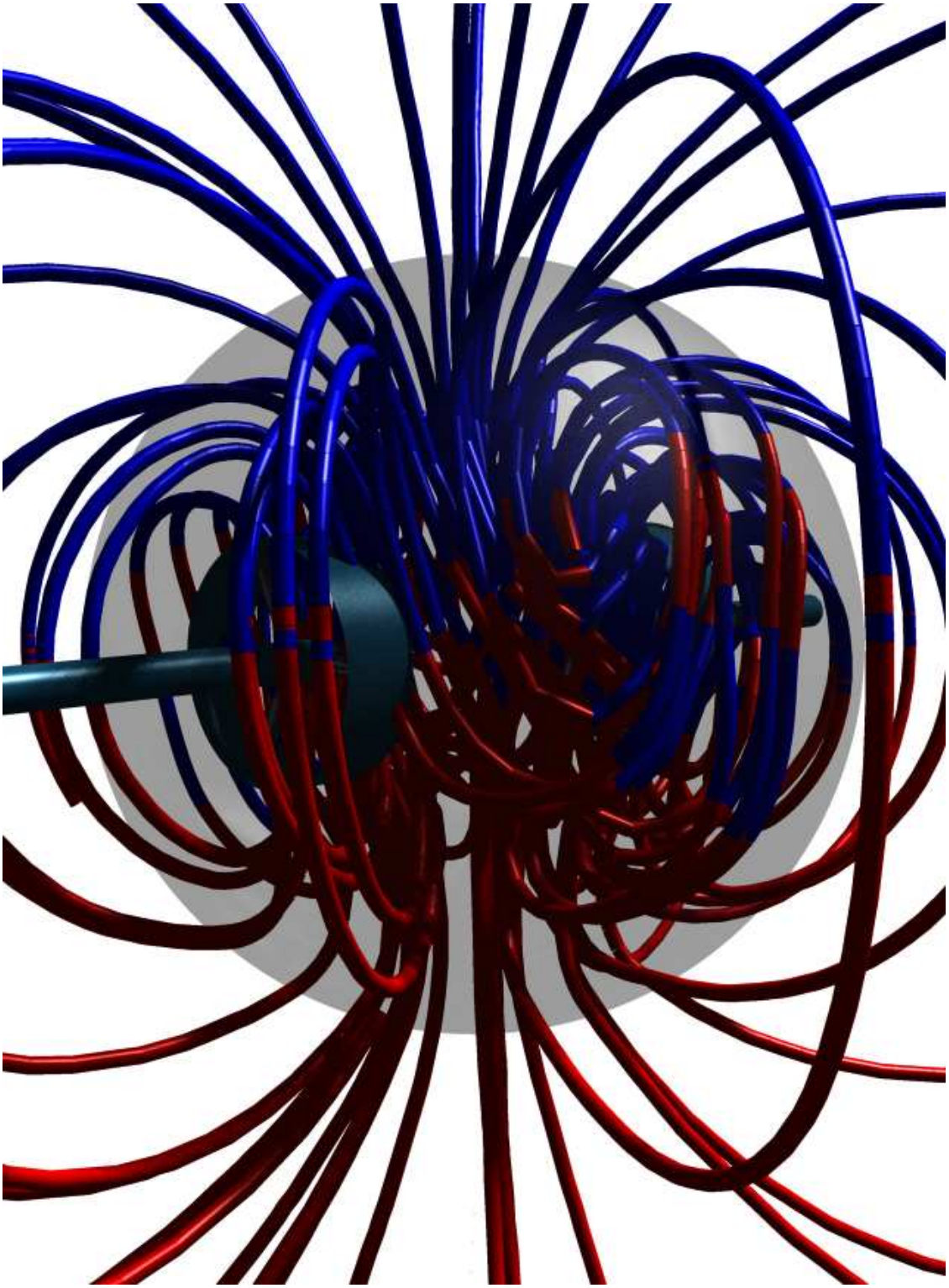

Figure 4.6 Magnetic field lines of a saturated dynamo state for a laminar flow with $Rm = 150$ and $Pm = 1$.

Chapter 5

Turbulent Dynamos

The presence of turbulence alters the onset and saturated state of the dynamo. Through the process of Lorentz braking described in Chapter 4, the magnetic field in saturation can relaminarize an otherwise turbulent fluid. When turbulence persists in the saturated state a turbulent EMF is produced which alters the magnetic field from an $m = 1$ equatorial dipole to a predominantly axisymmetric $m = 0$ dynamo, a state not possible without a fluctuating fluid. As Re is increased, the flow becomes more turbulent and larger Rm is required to stimulate dynamo action.

The flow changes from laminar to turbulent at $Re \approx 420$. Above this value, a hydrodynamic instability grows exponentially on the eddy-correlation time (τ_c) with an $m = 2$ spatial structure through nonlinear coupling; the instability quickly leads to strongly-fluctuating turbulent flows. Fluctuations about the mean flow exist at all scales, including variations in the large-scale flow responsible for the dynamo. The turbulence is inhomogenous with boundary layers, localized forcing regions, and strong shear layers.

The effect of these fluctuations on the dynamo onset conditions and on the resulting saturation mechanism depends sensitively upon the viscosity (parameterized by Pm). Fig. 5.1 shows an example of the broad range of dynamics exhibited by decreasing Pm, for an approximately fixed value of Rm. The magnetic field dynamics fall into several regimes depending on Re: the laminar dynamo, a dynamo which relaminarizes the saturated flow, a turbulent dynamo, and finally a turbulent flow with no dynamo. At $Pm = 1$, the viscosity is large enough to keep both the magnetic field and velocity field fully laminar. The spectrum

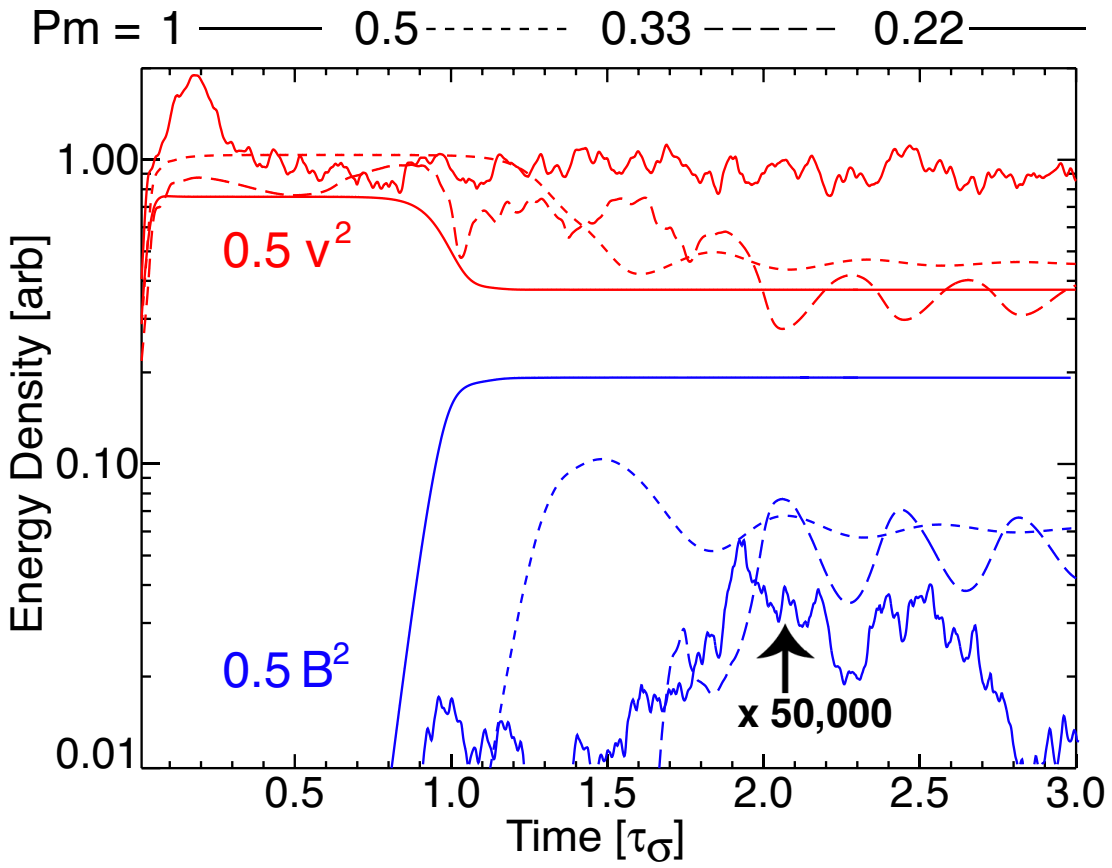

Figure 5.1 The magnetic and kinetic energy densities for runs with fixed Rm ($Rm = 165 \pm 3\%$) but different Pm versus time in τ_σ. Note that $Pm = 0.33$ shows a relaminarization of turbulent flow while $Pm = 0.22$ is barely amplifying the initial noise and is shown multiplied by 50,000.

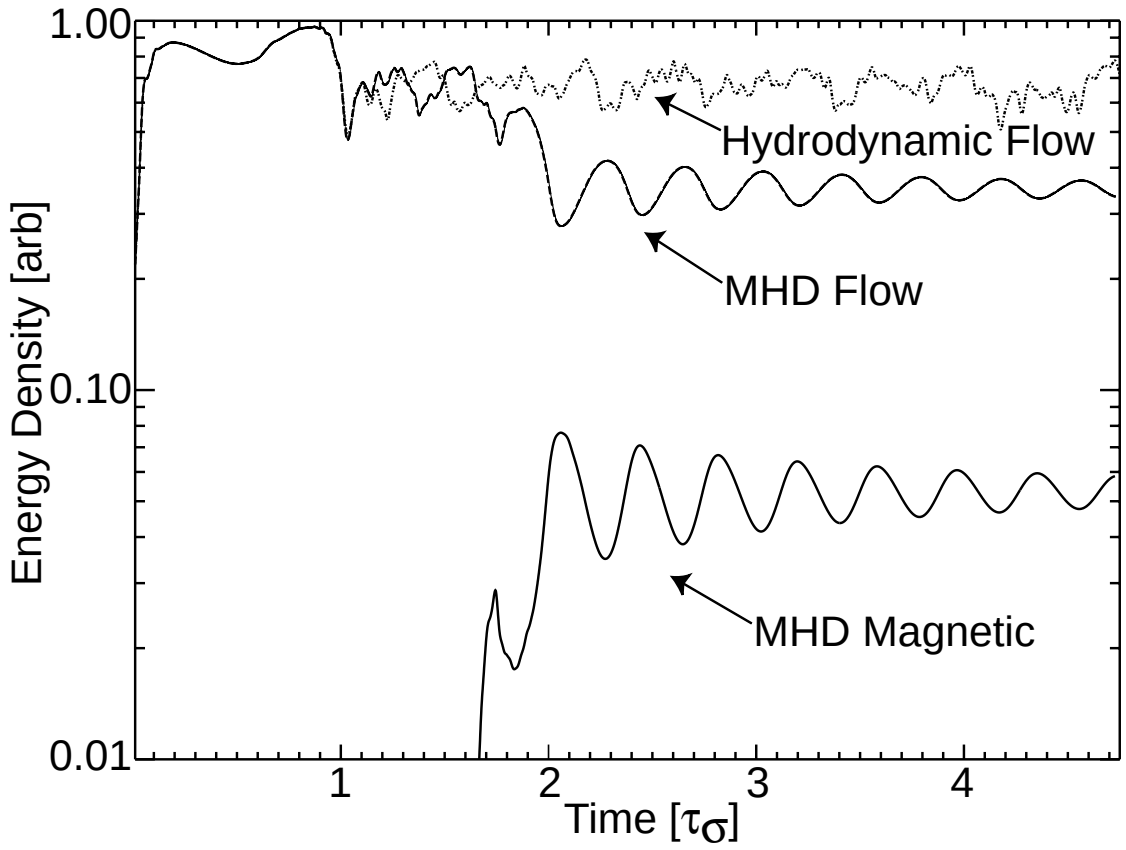

Figure 5.2 Kinetic energy densities from a hydrodynamic simulation are shown with the energy densities from an MHD simulation with the same simulation parameters, $Pm = 0.33$.

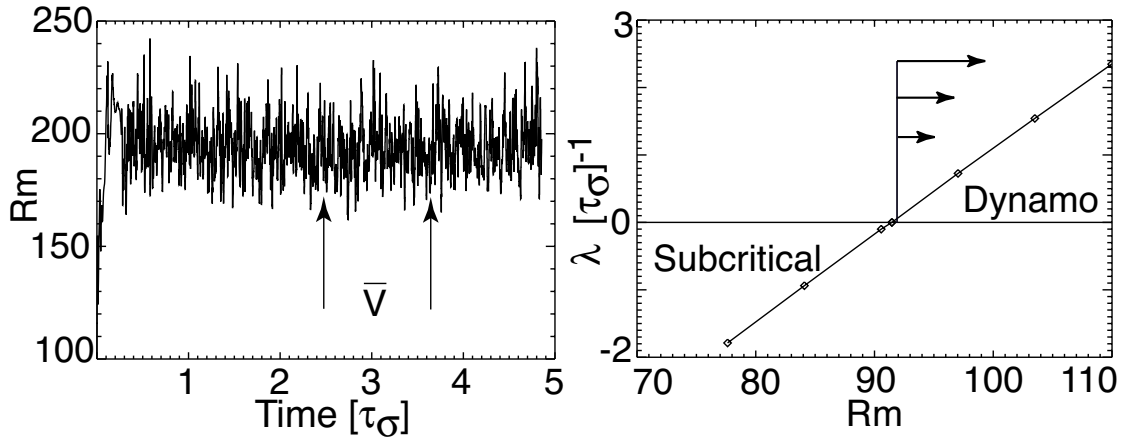

Figure 5.3 (a) Rm as a function of time. Taking a series of flows over the range shown the mean flow is calculated giving $Rm = 193$ and $Re = 863$. (b) The kinematic analysis of the average flow, where a magnetic field only evolution is done, varying Rm, to determine $Rm_{crit} = 91.5$.

is dominated by the driven velocity field and by the magnetic eigenmode, and the saturation mechanism is the toroidal braking and modification to the flow mentioned above.

For $Pm = 0.33$, Fig. 5.2 shows a flow that is initially turbulent, but the saturated state is laminar. The hydrodynamic case evolves the flow with $\mathbf{B} = 0$, while the MHD case evolves both $\mathbf{v}$ and $\mathbf{B}$. The turbulent saturation of the magnetic field results in a reduction in the fluctuations of the flow since the Lorentz braking has reduced Re below the hydrodynamic instability threshold (decreasing Re from 496 to 320). The hydrodynamic case shows that flow turbulence persists without the addition of a magnetic field into the system. The Re threshold distinguishing the turbulent saturated state from a relaminarized saturation is $Re \sim 630$.

If Rm is fixed at near the experimental maxima and Re is increased beyond 700 no dynamo is observed. Despite the fact that the mean flow still satisfies the requirements of a kinematic dynamo, the turbulent flow does not produce a growing magnetic field. It is the turbulent fluctuations about the mean flow that prevent field growth. Using the mean flow (averaged over several resistive times) for the $Pm = 0.22$ (with Rm=190, Re=863) as a prescribed flow in a kinematic evolution of the induction equation gives $Rm_{crit} \approx 93$,

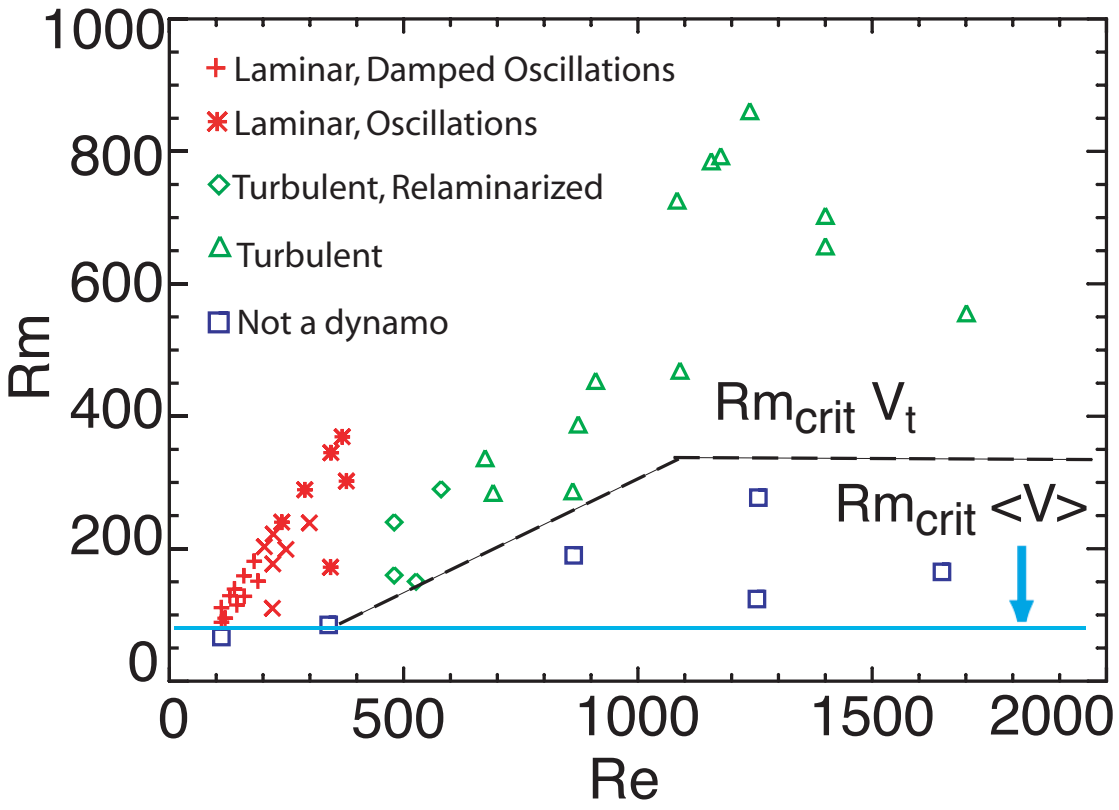

Figure 5.4 $Re - Rm$ phase diagram. A number of simulations whose hydrodynamic and final saturated states are documented in Fig. 5.1. Rm_{crit} for the mean flow $\langle \mathbf{V} \rangle$ is essentially independent of Re, while the effective dynamo threshold grows with Re. The dashed line shows the qualitative behavior of the dynamo threshold in turbulent flows (V_t).

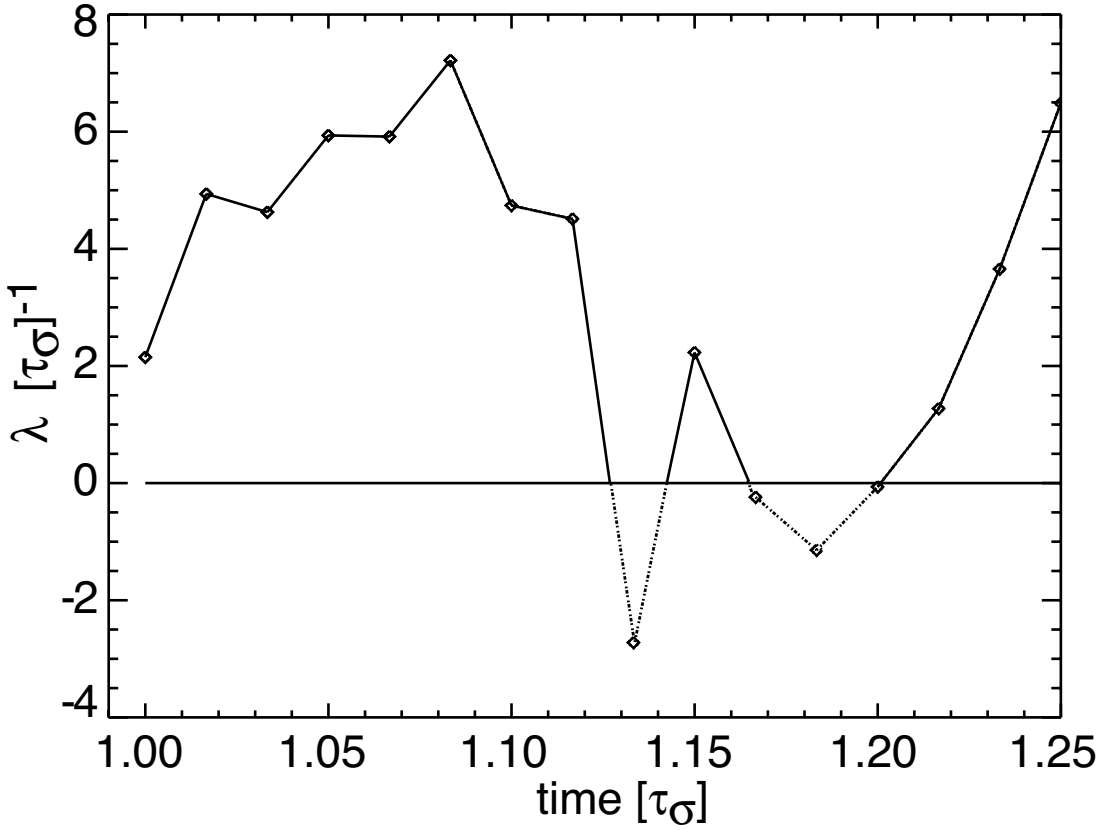

Figure 5.5 The growth rate of the dominant eigenmode calculated for a time-series of flow profiles.

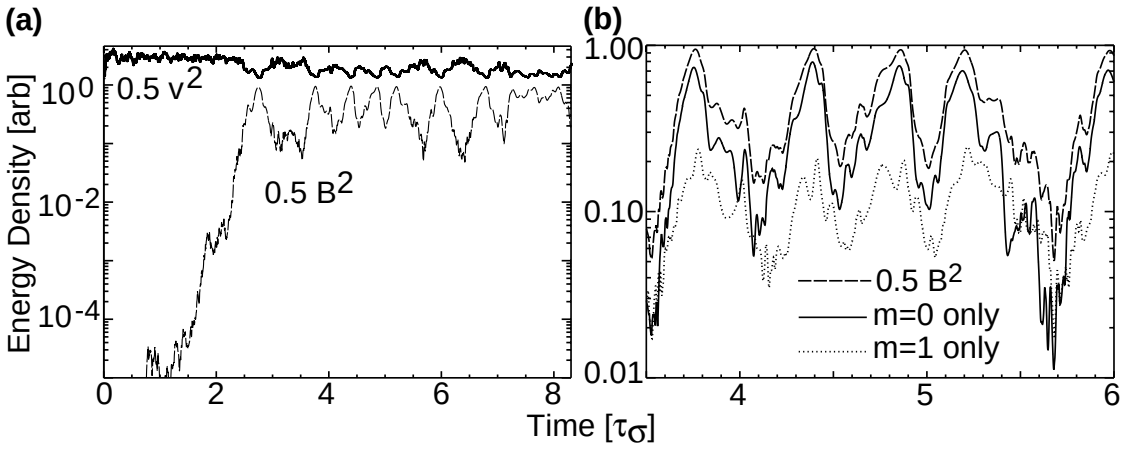

Figure 5.6 (a) The energy density of a turbulent dynamo with $Rm = 337$ and $Re = 674$. (b) The energy density of the axisymmetric magnetic field ($m = 0$) and the nonaxisymmetric dynamo ($m = 1$).

as shown in Fig. 5.3. Even though the average flow has Rm well above Rm_{crit} there is no dynamo. However, when the conductivity is doubled such that $Rm = 388$ a turbulent dynamo reemerges in the simulation. Hence, an empirical critical magnetic Reynolds number, $Rm_{crit,T}$ can be defined which depends on Re through the degree of turbulent fluctuations in the flow.

The results suggest the turbulent velocity fluctuations may govern the dynamo transition in a manner consistent with the turbulent resistivity of Eq. 1.8. From analysis of the simulation results, τ_c, the eddy scale size ℓ_v, and fluctuation levels $C = \tilde{v}/V_0$ have been determined in order to estimate the parameters in σ_T under the assumption that the homogeneous turbulence results roughly apply to this bounded, inhomogeneous flow. Typical volume averaged values measured in the $Rm = 190$, $Re = 863$ simulation are: $\ell_v = 0.022a$, $C = 0.45$, and $\tau_{corr} = 0.041\tau_\sigma$, which yields a volume-averaged conductivity reduction of $\sigma_T/\sigma = 0.461$. The diminished conductivity yields $Rm_{crit,T} = 238$. The results from all of the simulations are summarized in Fig. 5.4 which shows that an increasing Rm, at fixed Re reestablishes field growth where turbulent fluctuations had previously prohibited the dynamo. The dashed line in Fig. 5.4 shows that the correlation length and constant C increase with Re and eventually asymptote when the conductivity is effectively reduced by 70 %.

The effect of turbulence is described above in terms of a turbulent resistivity that assumed no *de facto* scale separation. The α effect requires a length scale separation between small scale turbulent mechanical helical fluctuations and a large scale magnetic field since α scales inversely with length scale. The β effect is under no such constraint, turbulent advection of flux should exist on any scale. If such a separation of scales does not exist, the α effect should disappear, while the β effect may be observable. Since no such scale separation exists in the simulations, the beta effect may be present where the alpha effect is absent.

An alternative viewpoint, consistent with the phenomenological interpretation of enhanced resistivity put forward here, is that the large scale variations in the velocity field are continuously changing the spatial structure and growth rates of the magnetic eigenmodes of the system. Two effects can be important. First, the instantaneous growth rate of the least

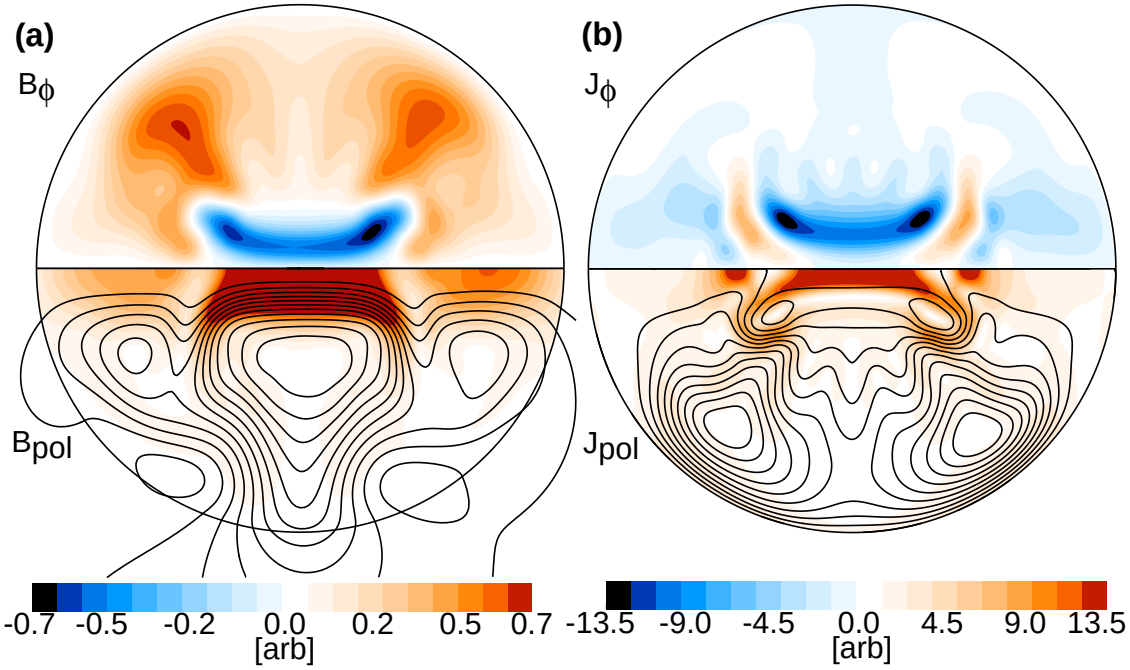

Figure 5.7 (a) The axisymmetric part of the magnetic field at $t = 6.02$ during the simulation shown in Fig. 5.6. The saturated plot of the poloidal magnetic field has a maximum of 1.7 . (b) The axisymmetric current at time $t = 6.02$. The saturated plot of the poloidal current has a maximum of 21.0 .

damped eigenmode fluctuates between growing and damped. For a run with $Rm = 193$, $Re = 893$ and $\epsilon = 0.4$, shown in Fig. 5.5, a dynamo occurs only when the flow spends sufficient time in phases which are kinematic dynamos. The kinematic growth rate is most often positive, consistent with the time averaged flow having growing magnetic field solutions, yet the modifications made to the flow during the subcritical periods is sufficient to stop the dynamo. Second, the turbulence couples energy from the growing magnetic eigenmode into spatially-similar damped eigenmodes. As the flows evolve, the spatial structure of the eigenmodes change. The magnetic field structure of a single eigenmode at some previous instant in time must be described in terms of several modes after the flow changes. This transfer of energy from the primary mode is equivalent to enhanced dissipation.

An example of a saturated turbulent magnetic field shows evidence of a turbulence induced EMF that may be similar to the one described in Chapter 6. A simulation with

$Rm = 337$ and $Re = 674$ shows that the $m = 1$ transverse dipole field is excited by the mean flow, however, in saturation a turbulent EMF gives rise to an $m = 0$ magnetic field, shown in Fig. 5.6(b). That turbulence drives the observed magnetic field is inferred from its axisymmetrically dominant structure which is prohibited for purely axisymmetric motion by Cowling's theorum [57].

The plot of the magnetic energy of the $Pm = 0.22$ simulation in Fig. 5.1 shows that near $Rm_{crit,T}$ the magnetic field is not fully resistively damped, and in fact has intermittent periods of sustained field growth. This effect is consistent with the intermittent excitation of the dynamo eigenmode by the mean flow. The peak magnetic energy is limited by the magnitude of the initialized noise the simulation is started with instead of the backreaction with the flow. This effect is especially relevant when the magnetic field is sustained by an external source as shown in Chapter 6.

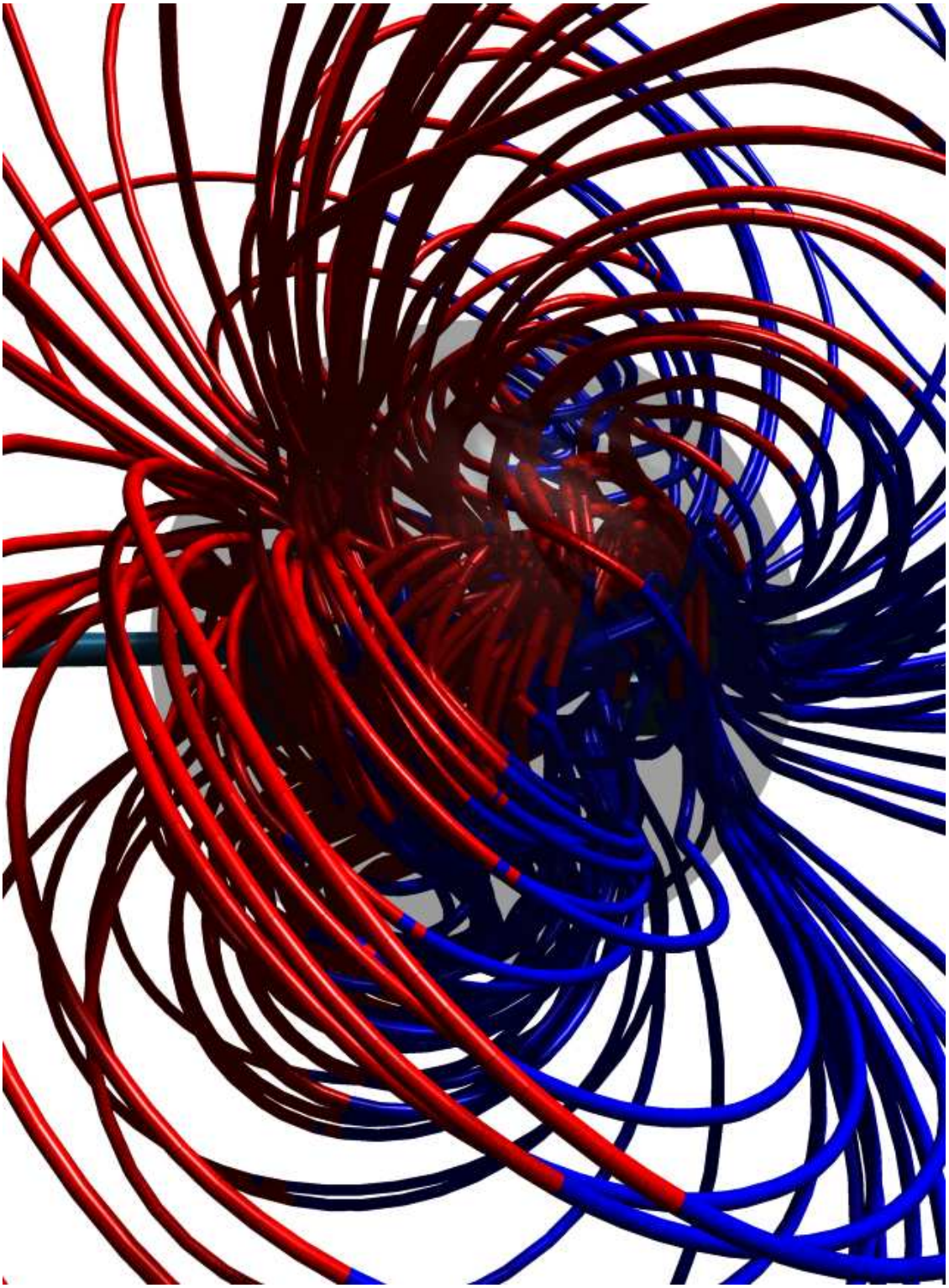

Figure 5.8 Magnetic field lines of the turbulent saturated dynamo with $Rm = 337$ and $Pm = 0.5$

Chapter 6

Simulations of a subcritical turbulent flow with a weak, externally-applied magnetic field

As a means of further investigating the role of fluctuation-driven currents, simulations have been performed for flows which are subcritical, i.e. the flows have $Rm < Rm_{crit}$ and are not expected to lead to self-excited magnetic fields. The MHD behavior is investigated by applying a magnetic field which is generated by currents flowing in coils external to the sphere. The configuration studied is similar to the set of experiments described by Spence *et al.* [58] and Nornberg *et al.* [59]

The numerical technique employed is similar to the dynamo simulations described above in all but one respect, namely a different boundary condition is employed on the poloidal scalar for the magnetic field:

$$\frac{\partial \mathrm{S}_{\ell,m}}{\partial r} + \frac{(\ell+1)}{a}\mathrm{S}_{\ell,m} = \frac{2\ell+1}{\ell+1}C_{\ell,m}. \tag{6.1}$$

These boundary conditions match the magnetic field to a scalar magnetic potential, $\mathbf{B} = -\nabla\Phi_m$, which solves Laplace's equation for the magnetic field in the region between the surface of the sphere and the external magnets. Its solution is well known:

$$\Phi_m(r,\theta,\phi) = \sum_{\ell,m}\left(A_{\ell,m}r^{\ell} + D_{\ell,m}r^{-(\ell+1)}\right)Y_{\ell}^{m}(\theta,\phi), \tag{6.2}$$

where $Y_{\ell}^{m}(\theta,\phi)$'s are the spherical harmonics. The $D_{\ell,m}$ terms represent the magnetic field generated by currents in the sphere, and the coefficients $A_{\ell,m}$ can be chosen to describe a magnetic field of arbitrary shape and orientation. In this paper and in the simulations described below, a uniform magnetic field is applied along the symmetry axis of the forcing

terms, and is characterized by a single coefficient $A_{1,0}$; all higher order terms being zero. The applied magnetic field, $B_{1,0}$ is weak enough so that it does not alter the large-scale flow. The strength of the applied magnetic field is moderated by keeping the Stuart number $N \equiv \sigma a B_{1,0}^2/\rho \mathbf{v}_0 < 0.1$. In sodium, with a $Rm \sim 100$, $N \sim 0.1$ would correspond to an applied field of 156 gauss. The applied field for these simulations corresponds to 57 gauss with $N \sim 10^{-2}$. However, since the velocity fluctuations decrease with scale, so too does the Stuart number, indicating the Lorentz force may influence small-scale fluid motion. Examples of such simulations are shown in Fig. 6.1, where the kinetic energy and magnetic energy are shown for laminar and turbulent runs.

For the laminar flow, the induced currents and resulting magnetic field are purely due to magnetic field interacting with the mean flow as seen in Figs. 6.2(a) and (b). Two main effects are observed. First, induced toroidal currents compress lines of poloidal magnetic field near the axis of the device. The lines are pulled outward at the poles and inward at the equator. The net result is a reduction of the poloidal field strength at the equator in the outer region, and a large amplification at the axis (the peak poloidal field is 18 times the applied field). Second, poloidal currents generate a toroidal magnetic field. These currents are generated by the well-known omega-effect of dynamo theory whereby differential toroidal rotation of the fluid is able to stretch the field into the toroidal direction [1]. The amplitude of the peak toroidal field is greater than 6 times the applied field.

The transition to turbulence is still characterized by the same $Re \sim 420$ threshold described above, since the Stuart number for the applied magnetic field is small. Below this threshold, the nonaxisymmetric part of the flows are negligible while above this threshold nonaxisymmetric fluctuations in both $\mathbf{B}$ and $\mathbf{V}$ can be as large as 40% of the mean values. The geometry of the simulations (axisymmetric drive terms aligned with the applied magnetic field) makes it possible to separate mean, axisymmetric quantities and fluctuating quantities,

$$\mathbf{B} = \langle \mathbf{B} \rangle + \widetilde{\mathbf{b}} \text{ and } \mathbf{v} = \langle \mathbf{V} \rangle + \widetilde{\mathbf{v}}, \tag{6.3}$$

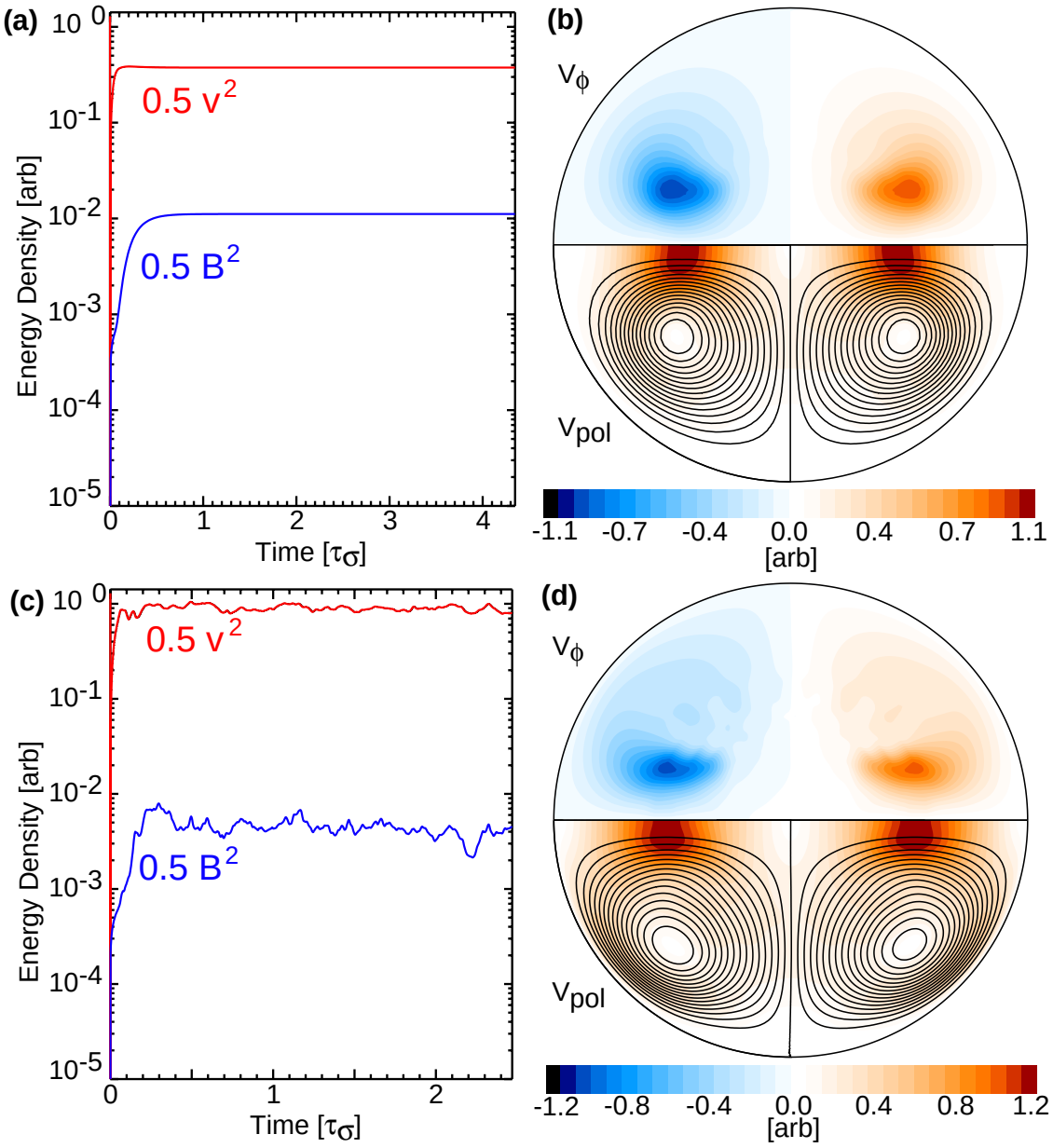

Figure 6.1 Simulations with an externally-applied, axisymmetric magnetic field. (a) Kinetic and magnetic energy densities for a Re=116 (laminar), Rm= 70 (subcritical) simulation. (b) The resulting flow. (c) Kinematic and magnetic energy densities for an Re=1803 (turbulent), Rm= 108 (subcritical) simulation. (d) The axisymmetric, time averaged velocity field for the turbulent simulation. The time average is over a large number of decorrelation times 2.1 $\tau\sigma \sim 30\tau_c$. The applied field in both cases is uniform and along the impeller axis with a magnitude of $B_0 \sim$ 51.3 G.

where the brackets denote a time average over several resistive times. In practice, $\langle \mathbf{B} \rangle$ and $\langle \mathbf{V} \rangle$ are axisymmetric for sufficiently long time averages. Using these definitions, the time-averaged magnetic fields and currents can be computed for laminar and turbulent flows, shown in Fig. 6.2.

Both laminar and turbulent flows demonstrate toroidal field production and expulsion of poloidal flux. Laminar and turbulent results differ in several important ways, however, which are attributable to the currents being driven by MHD fluctuations. First, the toroidal field is greatly reduced in the turbulent run. The induced toroidal field is 6 times the applied field strength in the laminar flow and is only twice the applied field in the turbulent case. The peak poloidal field is halved in the turbulent run, as shown in Fig. 6.2 (a). Second, there is a net magnetic dipole moment associated with the induced field which is not present in the laminar case. Both of these differences are the result of a change in the mean flow and a change in the mean-field Ohm's law, i.e. turbulence- generated currents are modifying the large scale, mean magnetic field.

The turbulent EMF is due to magnetic field and flow fluctuations consistent with the passive advection of the applied magnetic field by the Kolmogorov-like turbulence in the velocity field. If flow fluctuations are advected by the mean flow without substantial distortion by the mean flow then dispersion relation between temporal and spatial variations in the flow is $\omega \sim k\mathbf{V}$. Fig. 6.4 shows the wavenumber spectrum as estimated from the frequency spectrum of the fluctuations at a fixed point in the simulation. It is clear that both the velocity field and magnetic field have an inertial range ($k^{-5/3}$) and a dissipation scale, although the dissipation range begins at different values of k. The $k^{-5/3}$ scaling of the velocity field (the inertial range) is expected from the Kolmogorov theory of hydrodynamic turbulence. The dissipation scale for the fluid turbulence is expected to be at $k_\nu \sim Re^{-3/4} = 235$ which is roughly the position of the viscous cutoff shown in Fig. 6.4. The limited inertial range at low k, is primarily due to constraints on long-time averages of the data imposed by computational speed.

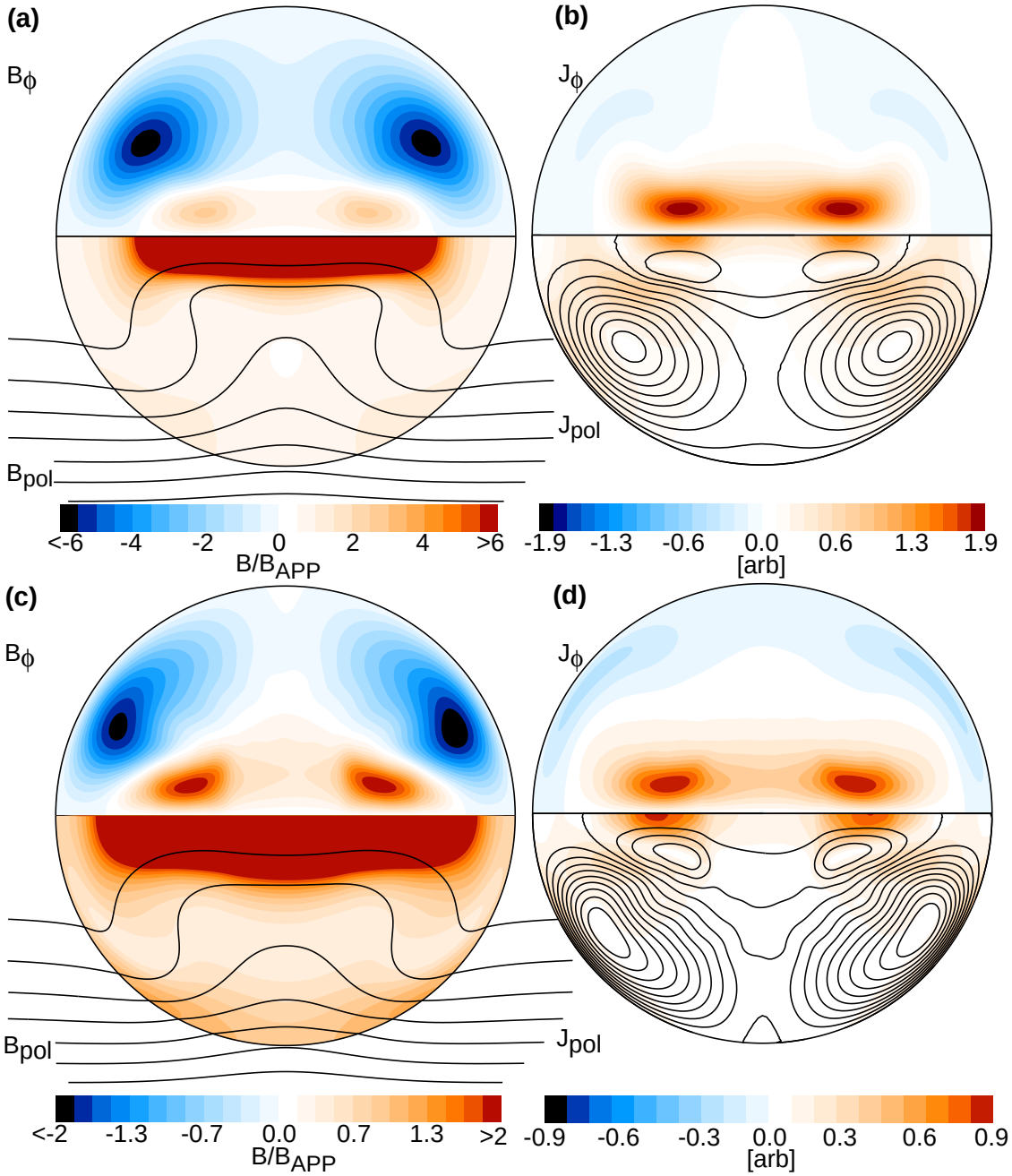

Figure 6.2 The top shows magnetic field and induced current for a laminar flow described in Fig. 6.1 [Rm=70 (subcritical), Re=116] . (a) The resulting total magnetic field (the sum of the externally applied field and those generated by the currents in the liquid metal) as a multiple of the applied magnetic field. (b) The mean current density. The bottom shows the time-averaged currents and magnetic fields for a turbulent flow [Rm=107 (subcritical), Re=1803] with externally generated magnetic field applied along the symmetry axis during the time interval 0.3-2.4 τ_σ. (c) The time-averaged magnetic field scaled to the applied field. The peak internal poloidal magnetic field is 9.3 times larger than the applied field. (d) The mean toroidal (upper half) poloidal current (lower half).

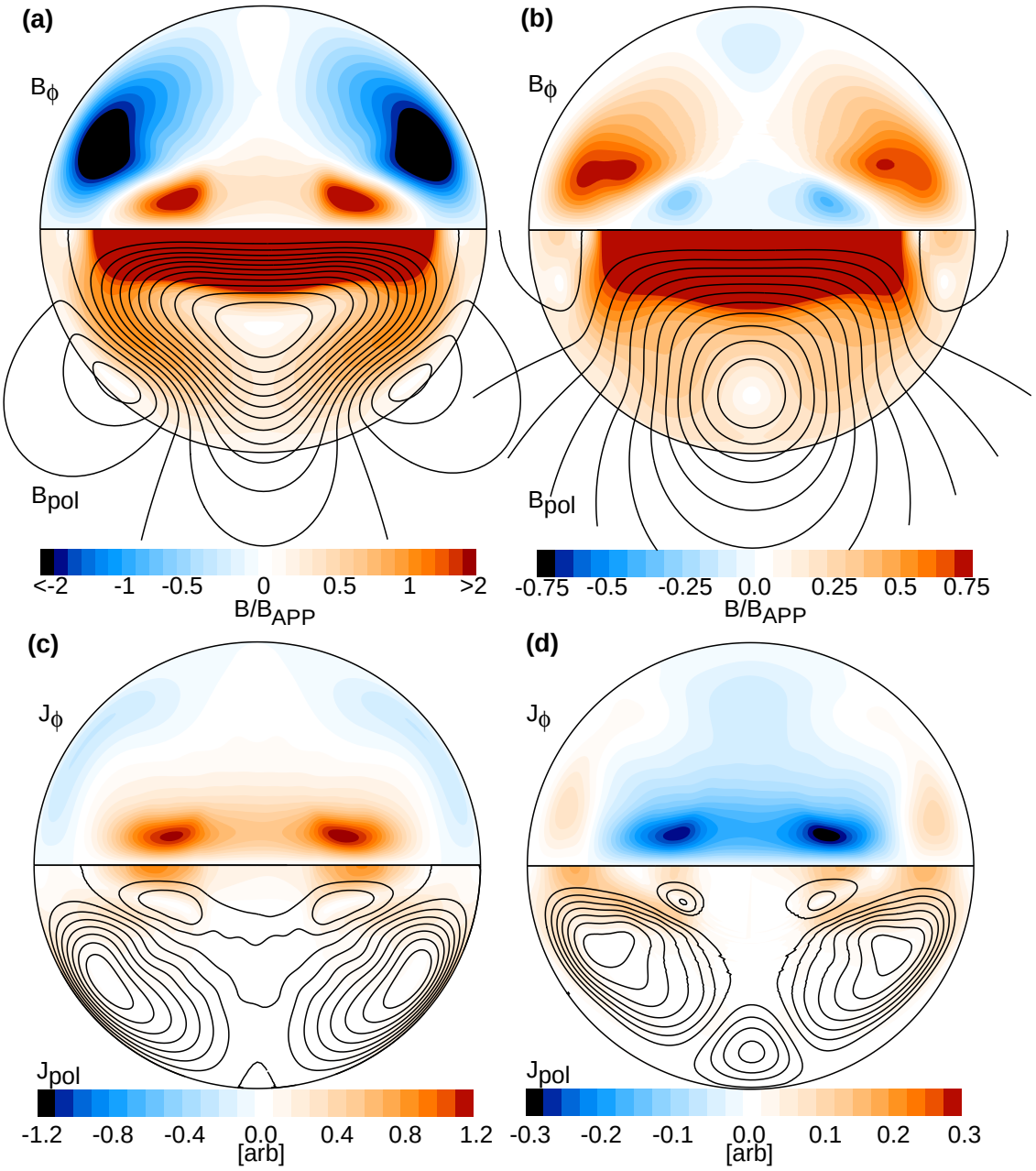

Figure 6.3 The time-averaged currents and magnetic fields for a turbulent flow [Rm=107 (subcritical), Re=1803] with externally generated magnetic field applied along the symmetry axis during the time interval 0.3-2.4 τ_σ. (a) The magnetic produced by the mean flow EMF. The peak internal poloidal magnetic field is 11.2 times larger than the applied field. (b) The magnetic field generated by the turbulent EMF scaled to the applied field. (c) The upper hemisphere shows the average value of $\sigma \langle \boldsymbol{V} \rangle \times \langle \boldsymbol{B} \rangle_\phi$. The bottom hemisphere shows the poloidal currents resulting from the mean-field EMF. (d) The upper hemisphere shows the average value of $\sigma \left\langle \widetilde{\mathbf{v}} \times \widetilde{\mathbf{b}} \right\rangle_\phi$. The bottom hemisphere shows the poloidal currents resulting from the fluctuations.

The $k^{-5/3}$ scaling of the magnetic field corresponds to the weak-field approximation in which the induced magnetic fluctuations are due to advection of the mean magnetic field by the mean flow [59] for $k < k_\sigma \sim Rm/a$. While the $k^{-11/3}$-spectrum results from the balance between the mean magnetic field advected by turbulence and the resistive dissipation of magnetic fluctuations.

The dissipation scale is evident from the knee in the wave number spectrum of Fig. 6.4. The spectrum is constructed from the power spectrum of the value of B_r near the equator. Consequently, the magnetic field gains structure at smaller scales as Rm increases, down to scale sizes of $\ell_\sigma = 2\pi/k_\sigma = 4.5\,\mathrm{cm}$ at $Rm = 140$.

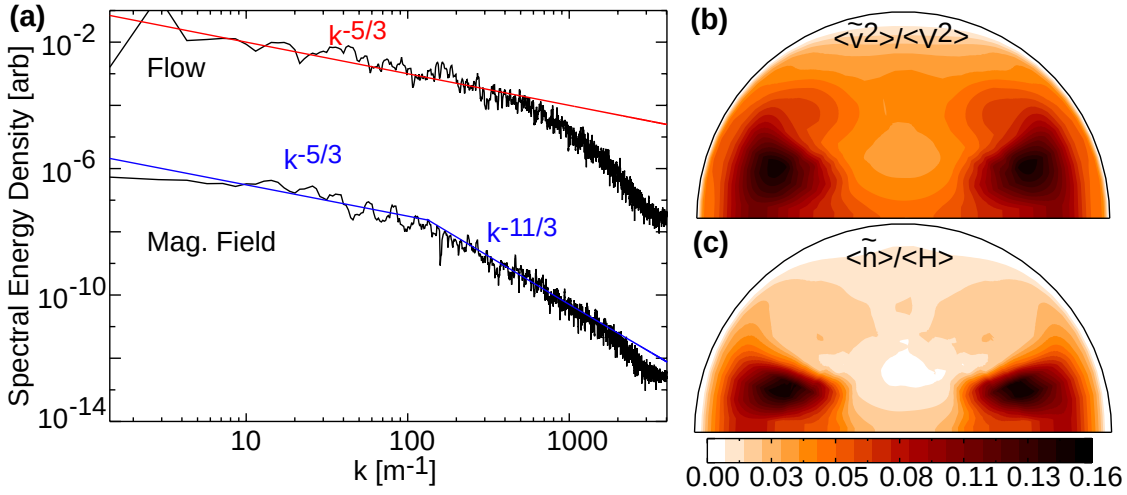

Figure 6.4 (a) The wavenumber spectrum computed from frequency spectrum of fluctuations from $6\tau_\sigma$ of flow (fitted with the red $k^{-5/3}$ curve) output at a position ($r \sim 0.75\ a$, $\theta \sim \pi/2$, ϕ=0) with a weak applied magnetic field of $B_0 \sim 51.3$ G, fitted with the blue $k^{-5/3}$ at low k and $k^{-11/3}$ at large k. For this simulation, $Rm = 130$, and $Re = 1450$ and fluctuations are assumed to be due to convection of spatial variations in the field. The dispersion relation is $\omega = k\,\langle V\rangle$. (b) The average of the squared turbulent fluctuations as a multiple of the peak squared mean flow. (c) The time average of the kinetic helicity fluctuations as a multiple of the helicity due to the mean flow.

The simultaneous fluctuating magnetic and velocity fields can potentially drive current in a mean-field sense. The motional EMF can be written as

$$\mathbf{v} \times \mathbf{B} = \langle \mathbf{V} \rangle \times \langle \mathbf{B} \rangle + \langle \mathbf{V} \rangle \times \widetilde{\mathbf{b}} + \widetilde{\mathbf{v}} \times \langle \mathbf{B} \rangle + \widetilde{\mathbf{v}} \times \widetilde{\mathbf{b}}, \tag{6.4}$$

where the mean-fields have been separated from the fluctuating parts. The time averages must be taken over times long compared to a turbulent decorrelation time and comparable to the resistive diffusion time. Since the turbulent decorrelation time, τ_C in the simulations is $\sim 0.05\tau_\sigma$, integrating the induction term over several resistive times yields

$$\langle \mathbf{v} \times \mathbf{B} \rangle = \langle \mathbf{V} \rangle \times \langle \mathbf{B} \rangle + \left\langle \widetilde{\mathbf{v}} \times \widetilde{\mathbf{b}} \right\rangle . \tag{6.5}$$

An important question, then, is whether the currents generated in the simulation are due to the EMF from the mean flow and magnetic field, $\langle \mathbf{V} \rangle \times \langle \mathbf{B} \rangle$, or by a turbulence EMF $\left\langle \widetilde{\mathbf{v}} \times \widetilde{\mathbf{b}} \right\rangle$. This can be investigated by examining the various terms in Ohm's Law

$$\mathbf{E} = \eta \mathbf{J} - \langle \mathbf{V} \rangle \times \langle \mathbf{B} \rangle + \left\langle \widetilde{\mathbf{v}} \times \widetilde{\mathbf{b}} \right\rangle \tag{6.6}$$

from the simulation results. Considering first, the toroidal currents generated in the turbulent runs, it is clear that in steady-state there can be no inductive electric field in the toroidal direction since the poloidal flux is constant. Axisymmetry precludes an electrostatic potential from driving current in the toroidal direction, and so the toroidal current can only be generated by the mean-flow and the turbulent EMF. The electric field is irrelevant. Thus any currents driven in the toroidal direction, contribute to the poloidal magnetic field. Fig. 6.3 shows the currents driven by these fluctuations, and their corresponding magnetic field. The fluctuation-induced magnetic field is 3.5 times larger than the applied field and comprises a third of the total field strength.

It has been recently shown that an axisymmetric flow and and axial magnetic field cannot induce a dipole moment in any simply-connected bounded system[58]. This is essentially due to the fact that the flow outside the conducting region is zero, while the streamlines of flow perpendicular to the magnetic flux are closed and bounded within the conducting region. Only a turbulent EMF can create the dipole moment. With a weak applied field in a turbulent fluid, averaging over several eddy turnover times and averaging along $\hat{\boldsymbol{\phi}}$ eliminates the nonaxisymmetric component of the current, therefore the only nontrivial component of the dipole moment is

$$\mu_Z = \oint d^3x r \sin\theta J_\phi. \tag{6.7}$$

The toroidal current generated by the turbulent fluctuations, $\langle \mathbf{v} \times \mathbf{b} \rangle$ from Eq. 6.5 is shown in Fig. 6.3 forming a dipole moment antiparallel to the external field, while the EMF due to $\mathbf{V}$ and $\mathbf{B}$ gives rise to a quadrupole magnetic field. The resulting poloidal field reduces the surface magnetic field by 20%. The largest values of the turbulent toroidal current occur where the omega-effect is also large. With the omega-effect providing a toroidal magnetic field, and the turbulent toroidal current causing a poloidal magnetic field this may be an $\alpha\Omega$-magnetic field. The turbulence is nonmirrorsymmetric, since the kinetic helicity due to fluctuations, shown in Fig. 6.4(c), is non-zero. However, the turbulent toroidal current is large where $\langle V \rangle \times \langle B \rangle$ is large and opposes the laminar toroidal current, and is thus consistent with a β-effect.

The poloidal current in Eq. 6.6 requires a treatment of the poloidal electric field. The time-averaged electric field is independent of the magnetic vector potential and in the low-frequency MHD limit charge is conserved so that $\boldsymbol{\nabla} \cdot \mathbf{J} = 0$ giving:

$$\boldsymbol{\nabla} \cdot \mathbf{E} = -\nabla^2 \Phi - \nabla^2 \tilde{\Phi} = \boldsymbol{\nabla} \cdot \left(\langle \mathbf{V} \rangle \times \langle \mathbf{B} \rangle + \left\langle \widetilde{\mathbf{v}} \times \widetilde{\mathbf{b}} \right\rangle \right), \tag{6.8}$$

where Φ and $\tilde{\Phi}$ are electrostatic potentials due to the stationary EMF, and turbulent EMF respectively. Fig. 6.2(d) shows the poloidal current is qualitatively similar to the current produced in a laminar simulation (Fig. 6.2(c)) since the mean flows are similar.

The simulations indicate there is a strong poloidal current associated with the fluctuations that acts to greatly reduce the toroidal magnetic field generated by a comparable laminar flow. Fig. 6.3 shows that there is a strong fluctuation-driven poloidal current near the vessel wall. This reduces the strength of the toroidal field in the core. This resembles the diamagnetic γ-effect, due to gradients in the turbulence intensity. The α-effect is the diagonal terms of a mean-field tensor: $\mathbf{J} = \sigma \boldsymbol{\alpha} \cdot \mathbf{B}$. The off-diagonal terms can also be written so that $\mathbf{J} = \sigma \boldsymbol{\gamma} \times \mathbf{B}$. Fig. 6.4 shows the squared velocity fluctuations decrease away from the axis of symmetry with the polar radius, ρ. For isotropic turbulence, the inhomogeneity in the fluctuations would give rise to a γ-effect of the form $-\sigma \boldsymbol{\gamma}(\rho) \times \mathbf{B_T}$ with $\boldsymbol{\gamma} \propto \boldsymbol{\nabla} \mathrm{v}^2$. The poloidal current due to turbulent diamagnetism would counteract the toroidal magnetic field caused by the omega-effect. Comparison between Fig. 6.4(b) with Fig.6.3(b) shows

that regions of steep gradients in the turbulent fluctuations correspond to regions of strong fluctuation induced poloidal current.

Chapter 7

Summary

The role of turbulence in generating current and moderating the growth of magnetic fields was studied for the Madison Dynamo experiment using a simple forcing term in a three-dimensional MHD computation. Two regimes were explored: one with an external applied magnetic field and flow subcritical to the dynamo instability and one with no external field and super-critical flow. Both cases showed significant deviations from the laminar expectations mandating a consistent treatment of the fluid turbulence. However, the manifestation of the turbulent currents for the two cases was markedly different.

The onset conditions for the dynamo instability are governed by the Pm of the system. At $Pm \sim 1$, the transition and saturation agree with laminar predictions and are considered laminar dynamos. At lower Pm the threshold for the dynamo excitation, Rm_{crit}, increases which is consistent with a reduction in conductivity due to turbulent fluctuations. The Pm values in the simulations is still orders of magnitude larger than in liquid-metal experiments (and for geo and solar dynamos) due to memory and speed limitations of computers, and so results from experiments are critical for verifying these results.

However, we believe the simulations capture the dominant effect since the fluctuations at the largest scales are the strongest contributers to the turbulent resistivity by the following argument. In Kolmogorov turbulence the spectrum is $E(k) \propto \epsilon^{2/3} k^{-5/3}$, where ϵ is the energy dissipation rate. Thus the turbulent resistivity goes as $[\int_{k_0}^{k_\nu} q^{-2} E(q) dq]^{-1/2} \sim \epsilon^{1/3} k_0^{-4/3}$, where k_0 is the wavenumber of the large scale eddies and k_ν is the dissipation scale wavenumber. Since $k_\nu \propto Re^{3/4}$, as Re becomes large in comparison to Rm, the effect of turbulent

fluctuations on conductivity will asymptote to a fixed value. We note that the simple dimensional analysis used here to obtain the scaling of the turbulent resistivity reflects isotropic, homogenous, mirror-symmetric turbulence and is derived in the limit that there is no mean flow; the dynamo relies almost entirely on the presence of a mean flow. Nonetheless, the turbulent resistivity model provides an order of magnitude estimate for the effect of turbulent fluctuations on magnetic energy growth, and is consistent with the results of simulations, other numerical studies with different conditions, and measurements in some liquid sodium experiments.

To quantify currents driven by fluctuations in the experiment, simulations of subcritical flows have been performed, and the currents driven by the turbulent fluctuations have been observed directly. The main effect of the turbulence on an externally-applied magnetic field is the reduction of field strength compared those computed for laminar flows. The laminar two-vortex flow compresses the applied poloidal magnetic flux near the axis of symmetry and through toroidal flow shear creates a strong toroidal field. Both effects are suppressed in turbulent flow. The mean flow produced at large Reynolds numbers differs from its laminar counterpart which accounts for some of the discrepancy between the build-up of toroidal field and flux compression of the poloidal field observed in the laminar and turbulent fluids. However, the poloidal magnetic field is also reduced because the turbulent flow gives rise to an EMF which induces a dipole moment in the opposite direction from the applied field.

Since the code is currently incapable of exceeding $Re \sim 2000$ without prohibatively long run-times, the code should be parallelized. By breaking the spectral decomposition into radial blocks, and utilizing parallel FFT's, substantial gains in speed for high resolution simulations should feasible. Also, in high Re simulations the subviscous scales may have little influence over the magnetic spectra since $k_\sigma << k_\nu$. A hyperviscosity or advanced fluid closure such as those employed in Large-Eddy simulations might be implemented to alleviate the need to resolve subviscous scales, though it is still unclear how close the simulation must be to experimental parameters to correctly resolve the turbulence.

While comparisons of flows output by the code with the measurements taken from a water-based experiment showed moderate agreement, more work could be done to model large scale flows and the properties of the hydrodynamic turbulence in the experiment.

The large scale flow could be more carefully constructed through the use of an empirical finite-element code such as FLUENT to fine-tune the impeller model used in the DYNAMO code. Additionally, an adequate truncation should be chosen on the forcing term to prevent resolution-dependent forcing.

To address the turbulent statistics of the flow, passive advection of a scalar by the fluid (material line element analysis) could be employed to help determine the nonlinear fluid characteristics. The values of Lyapunov exponents could be used to determine whether the statistics of an increasingly turbulent flow are asymptoting to some qualitative state independent of Re.

The backreaction of the turbulent dynamo remains substantially uncharacterized. While it is now known that Lorentz braking, and dynamic alterations in the magnetic eigenmode work in concert to cease magnetic field growth, a more robust mechanism is desirable. It may be possible to use the Ohm's law analysis presented in Chapter 6 to recast the backreaction of the turbulent dynamo into the language of MFT.

To further explore the turbulent current generated in the weak applied-field simulation a more exact treatment of tensors implied by the expansion of the turbulent induction for MFT is warranted. Since the α-effect requires the flow to be nonmirrorsymmetric, simulations with co-rotating impellers leading to a helicity-free $t_1^0 s_1^0$ flow should be finished. In absence of isotropy, turbulent statistics leading to the psuedo-scalars α, andβ can be calculated using two point correlation and analysis of the structure functions. While computationally expensive, this exact treatment may be the only way to definitively show the source of the turbulent current.

More effort must also be made to determine if the phenomenological interpretation of the increase in Rm_{crit} as being roughly synonymous with an decrease in the effective conductivity due to turbulence is adequate. The suppression of the dynamo as being an reduction in

conductivity due to turbulent fluctuations may not be the same as suppression due to altering of the kinematic eigenfunction by the instantaneous flow. If the threshold increase can be seen as merely decreasing the conductivity, the resistive scale should move toward larger scales or the rate of energy transfer to smaller-scales should increase. With a decreased conductivity, growth rates for the turbulent dynamo should be smaller than the laminar dynamo. If the ceasing of dynamo action occurs only through the alteration of large scale fluid flow the magnetic diffusive scale should be independent of fluctuation strength and the kinematic growth rate will depend only on the instantaneous kinematic growth rate. So far, the code has shown that neither interpretation prevails. No decrease in the growth rate is observed for the turbulent dynamo, and the growth rate depends only on the instantaneous value of the kinematic growth rate. Changing the conductivity at a fixed Re causes the dynamo to reappear. As of yet, nothing meaningful can be said of the exact position of the magnetic diffusive scale except that it does not coincide with the fluid diffusive scale. This distinction may be important since recent work suggests that the suppressed dynamo can be recovered through preferentially decreasing the large- scale fluctuations and increasing small-scale fluctuations in the flow[60].

LIST OF REFERENCES

[1] H. Moffatt, *Magnetic field generation in electrically conducting fluids* (Cambridge University Press, Cambridge, 1978).

[2] S. Childress and A. Gilbert, *Stretch, Twist, Fold: The fast dynamo* (Springer, Berlin, 1995).

[3] R. Kraichnan and S. Nagarajan, Phys. Fluid **10**, 859 (1967).

[4] U. Frisch, A. Pouquet, J. Léorat, and A. Mazure, J. Fluid Mech. **68**, 769 (1975).

[5] A. Pouquet and G. Patterson, J. Fluid Mech. **85**, 305 (1978).

[6] A. Alexakis, P. Mininni, and A. Pouquet, On the inverse cascade of magnetic helicity, 2005.

[7] J. Jackson, *Classical Electrodynamics*, 3rd ed. (John Wiley and Sons, New York, 1999), p. 270.

[8] K. Krause and K. Rädler, *Mean–field Magnetohydrodynamics and Dynamo Theory* (Pergamon Press, Oxford, 1980).

[9] D. Biskamp, *Nonlinear Magnetohydrodynamics* (Cambridge University Press, Cambridge, 1993).

[10] A. Pouquet, U. Frisch, and J. Léorat, J. Fluid Mech. **77**, 321 (1976).

[11] F. Cattaneo and D. Hughes, Phys. Rev. E **54**, 4532 (1996).

[12] A. Gruzinov and P. Diamond, Phys. Rev. Lett. **72**, 1651 (1994).

[13] E. Blackman and G. Field, Physical Review Letters **89**, 265007 (2002).

[14] K.-H. Rädler, M. Rheinhardt, E. Apstein, and H. Fuchs, Nonlinear Processes in Geophysics **9**, 171 (2002).

[15] U. Müller and R. Stieglitz, J. Fluid Mech. **498**, 31 (2004).

[16] P. Roberts and G. Glatzmaier, Rev. Mod. Phys. **72**, 1081 (2000).

[17] S. Balbus and J. Hawley, Rev. Mod. Phys. **70**, 1 (1998).

[18] E. Bullard and H. Gellman, Phil. Trans. R. Soc. Lond. A **247**, 213 (1954).

[19] P. H. Roberts, Phil. Trans. Roy. Soc. London A **272**, 60 (1972).

[20] D. Gubbins, Phil. Trans. R. Soc. Lond. A **274**, 493 (1973).

[21] G. Glatzmaier, J. Comp. Phys. **55**, 481 (1984).

[22] G. Glatzmaier and P. Roberts, Phys. Earth Plan. Int. **91**, 63 (1995).

[23] G. Glatzmaier, Ann. Rev. Earth Planet. Sci. in press (2002).

[24] A. Kageyama and T. Sato, Phys. Plasmas **2**, 1421 (1995).

[25] A. Kageyama and T. Sato, Phys. Plasmas **4**, 1569 (1997).

[26] W. Kuang and J. Bloxham, Nature **389**, 371 (1997).

[27] M. Meneguzzi, U. Frisch, and A. Pouquet, Phys. Rev. Lett. **47**, 1060 (1981).

[28] W. Müller, D. Biskamp, and R. Grappin, Phys. Rev. E **67**, 066302 (2003).

[29] S. Dennis and S. Singh, J. Comp. Phys **28**, 297 (1978).

[30] P. Roberts and A. Soward, Annu. Rev. Fluid Mech. **24**, 459 (1992).

[31] W. Kuang and J. Bloxham, J. Comp. Phys. **153**, 51 (1999).

[32] R. Hollerbach, Int. J. Numer. Meth. Fluids **32**, 773 (2000).

[33] P. Iroshnikov, Sov. Astron. **7**, 566 (1964).

[34] S. Boldyrev, Astrophys. J. Lett. **626**, (2005).

[35] S. Boldyrev and F. Cattaneo, Phys. Rev. Lett. **92**, 144501 (2004).

[36] Y. Ponty, P. Mininni, D. Montgomery, J. Pinton, H. Politano, and A. Pouquet, Phys. Rev. Lett. **94**, 164502 (2005).

[37] A. Schekochihin, S. Cowley, J. Maron, and J. McWilliams, Phys. Rev. Lett. **92**, 054502 (2004).

[38] F. Lowes and I. Wilkinson, Nature **198**, 1158 (1963).

[39] F. Lowes and I. Wilkinson, Nature **219**, 717 (1968).

[40] A. Gailitis, A. Lielausis, E. Platacis, S. Dement'ev, A. Cifersons, G. Gerbeth, T. Gundrum, F. Stefani, M. Christen, H. Hänel, and G. Will, Phys. Rev. Lett. **84**, 4365 (2000).

[41] A. Gailitis, A. Lielausis, E. Platacis, S. Dement'ev, A. Cifersons, G. Gerbeth, T. Gundrum, F. Stefani, M. Christen, and G. Will, Phys. Rev. Lett. **86**, 3024 (2001).

[42] A. Gailitis, A. Lielausis, E. Platacis, G. Gerbeth, and F. Stefani, Phys. Plasmas **71**, 2838 (2004).

[43] R. Stieglitz and U. Müller, Phys. Fluids **13**, 561 (2001).

[44] U. Müller and R. Stieglitz, Phys. Fluids **16**, (2004).

[45] A. Reighard and M. Brown, Phys. Rev. Lett. **86**, 2794 (2001).

[46] U. Müller and R. Stieglitz, Nonlinear Processes in Geophysics **9**, 165 (2002).

[47] F. Cattaneo, in *Modeling of Stellar Atmospheres*, Vol. S-210 of *ASP Conference Series*, edited by N. Piskunov, W. Weiss, and D. Gray (IAU Publications, Paris, 2002), .

[48] F. Pétrélis, M. Bourgoin, L. Marié, J. Burguete, A. Chiffaudel, F. Daviaud, S. Fauve, P. Odier, and J.-F. Pinton, Phys. Rev. Lett. **90**, 174501 (2003).

[49] N. Peffley, A. Cawthorne, and D. Lathrop, Phys. Rev. E **61**, 5287 (2000).

[50] R. O'Connell, R. Kendrick, M. Nornberg, E. Spence, A. Bayliss, and C. Forest, in *Proceedings of the NATO Advanced Research Workshop on Dynamo and Dynamics, a Mathematical Challenge, Cargése, France*, Vol. 26 of *Nato Science Series*, edited by P. Chossat, D. Armbustier, and I. Oprea (Kluwer, Dordrecht, 2001), p. 59.

[51] A. Kolmogorov, Dokl. AN SSSR **30**, 299 (1941).

[52] L. Quartapelle and M. Verri, Computer Physics Communications **90**, 1 (1995).

[53] C. Canuto, M. Hussaini, A. Quarteroni, and T. Zang, *Spectral Methods in Fluid Dynamics* (Springer-Verlag, Berlin, 1988), p. 84.

[54] M. Dudley and R. James, Proc. R. Soc. Lond. A **425**, 407 (1989).

[55] R. Holme and J. Bloxham, J. Geophys. Res. **101**, 2177 (1996).

[56] M. Abramowitz and I. Stegun, *Handbook of Mathematical Function* (National Bureau of Standards Applied Mathematics Series - 55, Washington DC, 1972).

[57] T. Cowling, Mon. Not. R. astr. Soc. **94**, 39 (1933).

[58] E. Spence, M. Nornberg, R. Kendrick, and C. Forest, Observation of a Turbulence-Generated Large Scale Magnetic Field, 2005.

[59] M. Nornberg, E. Spence, R. Kendrick, and C. Forest, Measurements of the Magnetic Field Induced by a Turbulent Flow of Liquid Metal, 2005.

[60] J. Laval, P. Blaineau, N. Leprovost, B. Dubrulle, and F. Daviaud, Influence of turbulence on the dynamo threshold, 2006.

[61] D. J. Acheson, *Elementary Fluid Dynamics* (Oxford University Press, Oxford, 2001), p. 187.

[62] W. Cheney and D. Kincaid, *Numerical Mathematics and Computing* (Brooks/Cole, Pacific Grove, CA, 1985).

[63] S. Chandrasekkar, *Hydrodynamic and hydromagnetic stability* (Dover, New York, 1961).

Appendix A: The MHD model and Nondimensionalization

The MHD equations which are solved in the DYNAMO code are derived from the more general incompressible, resistive viscous MHD equations. The equations are the nondimensionalized into parameters relevant for the Madison Dynamo experiment. Neglecting the displacement current, the governing equations are,

$$\text{Fluid Momentum:} \quad \rho_0\big(\frac{\partial \mathbf{v}}{\partial t} + (\mathbf{v}\cdot\boldsymbol{\nabla})\mathbf{v}\big) = \boldsymbol{\nabla}\cdot\underline{\underline{\mathbf{T}}} + \mathbf{F} + \mathbf{J}\times\mathbf{B}, \tag{A.1}$$

$$\text{Ampere's Law:} \quad \mu_0\mathbf{J} = \boldsymbol{\nabla}\times\mathbf{B}, \tag{A.2}$$

$$\text{Faraday's Law:} \quad -\frac{\partial \mathbf{B}}{\partial t} = \boldsymbol{\nabla}\times\mathbf{E}, \tag{A.3}$$

$$\text{Ohm's Law:} \quad \sigma\left(\mathbf{E} + \mathbf{v}\times\mathbf{B}\right) = \mathbf{J}, \tag{A.4}$$

$$\text{Incompressibility:} \quad \boldsymbol{\nabla}\cdot\mathbf{v} = 0, \tag{A.5}$$

$$\boldsymbol{\nabla}\cdot\mathbf{B} = 0, \tag{A.6}$$

where quantities are defined in the typical way as any nonlinear MHD treatment such as that found in Biskamp [9] and $\mathbf{F}$ is a stirring term. Assuming single fluid MHD and using the incompressibility condition (Eq. A.5) the divergence of the stress tensor is:

$$\boldsymbol{\nabla}\cdot\underline{\underline{\mathbf{T}}} = \boldsymbol{\nabla}P - \mu\nabla^2\mathbf{v}, \tag{A.7}$$

where P is the pressure and μ is the fluid viscosity. Using single fluid Ohm's law, Eq. A.4, to eliminate the electric field from Ampere's law, Eq. A.2, gives

$$-\sigma\frac{\partial \mathbf{B}}{\partial t} = \boldsymbol{\nabla}\times\big(\mathbf{J} - \sigma\mathbf{v}\times\mathbf{B}\big). \tag{A.8}$$

Temperature is constant on the timescales of the magnetic evolution thus the conductivity is assumed constant, and the first term on the right hand side of Eq. A.8 expands as

$$\boldsymbol{\nabla}\times\mathbf{J} = \boldsymbol{\nabla}\times\boldsymbol{\nabla}\times\frac{\mathbf{B}}{\mu_0} = \frac{1}{\mu_0\sigma}\big[\boldsymbol{\nabla}(\boldsymbol{\nabla}\cdot\mathbf{B}) - \boldsymbol{\nabla}^2\mathbf{B}\big] \text{ where } \eta \equiv \frac{1}{\mu_0\sigma}. \tag{A.9}$$

Here η is the magnetic diffusivity [1] Lastly, using Eq. A.6 gives the induction equation:

$$\frac{\partial \mathbf{B}}{\partial t} = \boldsymbol{\nabla}\times\mathbf{v}\times\mathbf{B} + \eta\nabla^2\mathbf{B} \tag{A.10}$$

[1]The magnetic diffusivity of sodium at 100 $^\circ C$ is roughly $1/(4\pi) = 0.080 m^2 s^{-1}$.

The nondimensional parameters are

$$\mathbf{x} \;=\; L\mathbf{x'}\;,\; t \;=\; \tau_\sigma t' = t'\frac{L^2}{\eta},\; Pm = \frac{\nu}{\eta},\; \mathbf{v} \;=\; v_0\mathbf{v'} \tag{A.11}$$

where L denotes a characteristic spatial scale choosen to be the size of the conducting region ($L = 0.55m$)

Using Eq. A.2, the units of the current density in terms of the magnetic field units are $J_0 = B_0/\mu_0 L$. Comparing the dimensions of the Lorentz force to the advection term in Eq. A.1, the magnetic field scales as $v_0^2\rho_0/L = J_0B_0$, which implies $B_0 = v_0\sqrt{\mu_0\rho_0}$. Similar analysis shows that the nondimensional pressure and stirring term, are $P_0 = v_0^2\rho_0$ and $F_0 = \rho_0 v_0^2/L$.

Rewriting the momentum equation with these substitutions gives:

$$\rho_0\left(\frac{v_0}{\tau_\sigma}\frac{\partial}{\partial t'}\mathbf{v'} \;+\frac{v_0^2}{L}\;(\mathbf{v'}\cdot\boldsymbol{\nabla'})\mathbf{v'}\right) \;=\; -\frac{P_0}{L}\boldsymbol{\nabla'}P \;+\; \frac{\nu v_0}{L^2}\nabla'^2\mathbf{v'} \;+\; F_0\mathbf{F'} \;+\; J_0B_0\mathbf{J}\times\mathbf{B}. \tag{A.12}$$

Multipling through by $\tau_\sigma/v_0\rho_0$ and substituting the nondimensional variables derived above yields

$$\frac{\partial}{\partial t'}\mathbf{v'} \;+\frac{v_0L}{\eta}\;(\mathbf{v'}\cdot\boldsymbol{\nabla'})\mathbf{v'} \;=\; -\frac{v_0a}{\eta}\boldsymbol{\nabla'}P' \;+\frac{\nu}{\eta}\nabla'^2\mathbf{v'} \;+\; \frac{v_0L}{\eta}\mathbf{F'} \;+\; \frac{v_0L}{\eta}\mathbf{J'}\times\mathbf{B'}. \tag{A.13}$$

The common coefficient in Eq. A.13 is the magnetic Reynold's number, Rm; the meaning of this quantity is apparent in the nondimensionalization of Eq. A.10 with

$$\frac{B_0}{\tau_\sigma}\frac{\partial\mathbf{B'}}{\partial t'} = \frac{v_0B_0}{L}\boldsymbol{\nabla}\times\mathbf{v'}\times\mathbf{B'} + \frac{\eta B_0}{L^2}\boldsymbol{\nabla}'^2\mathbf{B'} \;\rightarrow\; \frac{\partial\mathbf{B'}}{\partial t'} = Rm\boldsymbol{\nabla}\times\mathbf{v'}\times\mathbf{B'} + \boldsymbol{\nabla}'^2\mathbf{B'}, \tag{A.14}$$

the magnetic Reynold's number moderates the ratio:

$$\frac{|\boldsymbol{\nabla}\times\mathbf{v'}\times\mathbf{B'}|}{|\boldsymbol{\nabla}'^2\mathbf{B'}|} \sim Rm. \tag{A.15}$$

Fourier decomposition of this equation for a single wave shows that, in absence of a flow, the $\boldsymbol{\nabla}'^2\mathbf{B'}$ term can only resulting in decaying magnetic field while $\mathbf{v'}\times\mathbf{B'}$ is the emf. Qualitatively then, the magnetic Reynolds number denotes the ratio of advective effects to resistive effects on $\mathbf{B'}$.

Table A.1

Conversions for Nondimensional Quantities		
Nondimensional Quantity	Multiplicative Factor	SI Units
v	$\frac{Rm\eta}{L}$	$[m \cdot s^{-1}]$
B	$\sqrt{\mu_0\rho_0}\frac{Rm\eta}{L}$	$[T]$
J	$\sqrt{\frac{\rho_0}{\mu_0}}\frac{Rm\eta}{L^2}$	$Amp \cdot m^{-3}$
E	$\sqrt{\mu_0\rho_0}\left(\frac{Rm\eta}{L}\right)^2$	$V \cdot m^{-3}$

Having nondimensionalized most of the equations listed above, the primed notation is dropped and the data is presented in nondimensional format except where a direct comparison to experiment is desired. The nondimensionalized momentum and induction equations are

$$\frac{\partial \mathbf{v}}{\partial t} + Rm(\mathbf{v}\cdot\boldsymbol{\nabla})\mathbf{v} = -Rm\boldsymbol{\nabla}P + Pm\nabla^2\mathbf{v} + Rm\mathbf{F} + Rm\mathbf{J}\times\mathbf{B}, \tag{A.16}$$

$$\frac{\partial \mathbf{B}}{\partial t} = Rm\boldsymbol{\nabla}\times\mathbf{v}\times\mathbf{B} + \boldsymbol{\nabla}^2\mathbf{B}. \tag{A.17}$$

The means to converting all nondimensional variables back to SI units is given in Table A.1.

Since the electric field and potential are often calculated as a post-processing step it is useful to have a nondimensional expression for Eq. A.4 so it is assumed that the field quantities can be represented as a dimensional scalar multiplied by unitless tangential vectors so that:

$$E_0\mathbf{E}' = -v_0B_0(\mathbf{v}'\times\mathbf{B}') + \eta J_0\mathbf{J}', \tag{A.18}$$

where $E_0,\ v_0,\ B_0,\ J_0$ are dimensions of their respective variables. From Faraday's law, Eq. A.3 the scaling for the electric field, E_0, is

$$\boldsymbol{\nabla}\times\mathbf{E} = -\frac{\partial\mathbf{B}}{\partial t} \implies E_0 = \frac{\sqrt{\mu_0\rho}\ v_0L}{\tau_\sigma}. \tag{A.19}$$

Substituting these dimensionless expressions into Eq. A.4 gives

$$\frac{\sqrt{\mu_0\rho}\ v_0L}{\tau_\sigma}\mathbf{E}' = -\sqrt{\mu_0\rho}\ v_0^2(\hat{\mathbf{v}}\times\mathbf{B}') + \frac{\eta\sqrt{\mu_0\rho}\ v_0}{\mu_0L}\mathbf{J}'. \tag{A.20}$$

Multiplying by $\tau_\sigma/\sqrt{\mu_0\rho}\ v_0 L$

$$\mathbf{E}' = -\frac{v_0\tau_\sigma}{L}(\mathbf{v}' \times \mathbf{B}') + \frac{\eta\tau_\sigma}{\mu_0 L^2}\mathbf{J}'. \tag{A.21}$$

Substituting the definition of τ_σ and dropping the primed notation:

$$\mathbf{E}' = -\frac{v_0\mu_0}{\eta}(\mathbf{v}' \times \mathbf{B}') + \mathbf{J}' \implies \mathbf{E} = -Rm(\mathbf{v} \times \mathbf{B}) + \mathbf{J}. \tag{A.22}$$

The means to converting all nondimensional variables to SI units in Table A.1.

Appendix B: Fourth Order Finite Differences on a Nonuniform Grid

This chapter shows how finite differences can be used to obtain accurate numerical representations of radial derivatives. The treatment of regularity conditions at the origin as forward-finite differences is also discussed.

The flow must be zero at the wall by the no-slip requirement, thus a rapid change in the flow occurs as the boundary is approached. The gradients in flow near the wall form boundary layers, where viscous stress dominates. The rough thickness of the boundary layer, δ scales as $\delta \sim Re^{1/2}$[61]. To resolve boundary layers a grid spacing which becomes smaller near the surface is practical. To resolve the viscous effects the momentum advance which requires Laplacian and bi-Laplacian

$$\nabla^2 f = \left(\frac{\partial^2}{\partial r^2} + \frac{2}{r}\frac{\partial}{\partial r} - \frac{p_l}{r^2}\right), \text{ and} \tag{B.1}$$

$$\nabla^4 f = \left(\frac{\partial^4}{\partial r^4} + \frac{4}{r}\frac{\partial^3}{\partial r^3} - \frac{2p_l}{r^2}\frac{\partial^2}{\partial r^2} + \frac{(p_l^2 - 2p_l)}{r^4}\right) f \text{ where } p_l = l(l+1) \tag{B.2}$$

should be expressed to high order in Δr. Finite differences is chosen for the radial grid since it provides a uniform grid-size, Δr, near the origin and $x\Delta r$, where $0 < x \leq 1$ (mesh packing) near the wall. The Laplacian and bi-Laplacian are computed through the Taylor series of five points, around a center point, $f(i)$:

$$\begin{aligned}
f(i-2) &= f(i) - b\frac{\partial f(i)}{\partial r} + \frac{b^2}{2!}\frac{\partial^2 f(i)}{\partial r^2} - \frac{b^3}{3!}\frac{\partial^3 f(i)}{\partial r^3} + \frac{b^4}{4!}\frac{\partial^4 f(i)}{\partial r^4} + \mathcal{O}(\Delta r^5) \\
f(i-1) &= f(i) - c\frac{\partial f(i)}{\partial r} + \frac{c^2}{2!}\frac{\partial^2 f(i)}{\partial r^2} - \frac{c^3}{3!}\frac{\partial^3 f(i)}{\partial r^3} + \frac{c^4}{4!}\frac{\partial^4 f(i)}{\partial r^4} + \mathcal{O}(\Delta r^5) \\
f(i) &= f(i) \\
f(i+1) &= f(i) + d\frac{\partial f(i)}{\partial r} + \frac{d^2}{2!}\frac{\partial^2 f(i)}{\partial r^2} + \frac{d^3}{3!}\frac{\partial^3 f(i)}{\partial r^3} + \frac{d^4}{4!}\frac{\partial^4 f(i)}{\partial r^4} + \mathcal{O}(\Delta r^5) \\
f(i+2) &= f(i) + g\frac{\partial f(i)}{\partial r} + \frac{g^2}{2!}\frac{\partial^2 f(i)}{\partial r^2} + \frac{g^3}{3!}\frac{\partial^3 f(i)}{\partial r^3} + \frac{g^4}{4!}\frac{\partial^4 f(i)}{\partial r^4} + \mathcal{O}(\Delta r^5)
\end{aligned}$$

where $b = [\Delta r(i-1) + \Delta r(i-2)]$, $c = \Delta r(i-1)$, $d = \Delta r(i+1)$, and $g = [\Delta r(i+1) + \Delta r(i+2)]$.

Expressed in matrix form as,

$$\begin{bmatrix} f(i-2) \\ f(i-1) \\ f(i) \\ f(i+1) \\ f(i+2) \end{bmatrix} = \begin{bmatrix} 1 & -b & \frac{b^2}{2} & \frac{-b^3}{6} & \frac{b^4}{24} \\ 1 & -c & \frac{c^2}{2} & \frac{-c^3}{6} & \frac{c^4}{24} \\ 1 & 0 & 0 & 0 & 0 \\ 1 & d & \frac{d^2}{2} & \frac{d^3}{6} & \frac{d^4}{24} \\ 1 & g & \frac{g^2}{2} & \frac{g^3}{6} & \frac{g^4}{24} \end{bmatrix} \begin{bmatrix} f(i) \\ f^{(1)}(i) \\ f^{(2)}(i) \\ f^{(3)}(i) \\ f^{(4)}(i) \end{bmatrix}.$$

Inverting the coefficient matrix gives,

$$\begin{bmatrix} f(i) \\ f^{(1)}(i) \\ f^{(2)}(i) \\ f^{(3)}(i) \\ f^{(4)}(i) \end{bmatrix} = M \begin{bmatrix} f(i-2) \\ f(i-1) \\ f(i) \\ f(i+1) \\ f(i+2) \end{bmatrix},$$

where

$$M =$$

$$\begin{bmatrix} 0 & 0 & 1 & 0 & 0 \\ \frac{c\,d\,g}{b\,(b-c)\,(b+d)\,(b+g)} & -\frac{b\,d\,g}{(b-c)\,c\,(c+d)\,(c+g)} & \frac{1}{b}+\frac{1}{c}-\frac{d+g}{d\,g} & -\frac{b\,c\,g}{d\,(b+d)\,(c+d)\,(d-g)} & \frac{b\,c\,d}{(d-g)\,g\,(b+g)\,(c+g)} \\ \frac{-2\,(-(d\,g)+c\,(d+g))}{b\,(b-c)\,(b+d)\,(b+g)} & \frac{2\,(-(d\,g)+b\,(d+g))}{(b-c)\,c\,(c+d)\,(c+g)} & \frac{2\,(b\,(c-d-g)+d\,g-c\,(d+g))}{b\,c\,d\,g} & \frac{2\,b\,c-2\,(b+c)\,g}{d\,(b+d)\,(c+d)\,(d-g)} & \frac{-2\,b\,c+2\,(b+c)\,d}{(d-g)\,g\,(b+g)\,(c+g)} \\ \frac{6\,(c-d-g)}{b\,(b-c)\,(b+d)\,(b+g)} & \frac{6\,(-b+d+g)}{(b-c)\,c\,(c+d)\,(c+g)} & \frac{6\,(b+c-d-g)}{b\,c\,d\,g} & \frac{6\,(b+c-g)}{d\,(b+d)\,(c+d)\,(d-g)} & \frac{-6\,(b+c-d)}{(d-g)\,g\,(b+g)\,(c+g)} \\ \frac{24}{b\,(b-c)\,(b+d)\,(b+g)} & \frac{-24}{(b-c)\,c\,(c+d)\,(c+g)} & \frac{24}{b\,c\,d\,g} & \frac{24}{d\,(b+d)\,(c+d)\,(d-g)} & \frac{-24}{(d-g)\,g\,(b+g)\,(c+g)} \end{bmatrix}$$

The coefficients for the ∇^4 operator, for example, are determined by taking the inner product of $\underline{\underline{M}}$ with:

$$\nabla^4 f(i) = \begin{bmatrix} \frac{(-2+p_l)p_l}{r^4} & 0 & \frac{-2p_l}{r^2} & \frac{4}{r} & 1 \end{bmatrix} \begin{bmatrix} f(i) \\ f^{(1)}(i) \\ f^{(2)}(i) \\ f^{(3)}(i) \\ f^{(4)}(i) \end{bmatrix}$$

The result is,

$$\nabla^4 f(i) = \begin{bmatrix} \frac{4\left(-(d\,g\,p_l)+c\,(d+g)\,p_l+6\,c\,r-6\,(d+g)\,r+6\,r^2\right)}{b\,(b-c)\,(b+d)\,(b+g)\,r^2} \\ \frac{-4\left(-(d\,g\,p_l)+b\,(d+g)\,p_l+6\,b\,r-6\,(d+g)\,r+6\,r^2\right)}{(b-c)\,c\,(c+d)\,(c+g)\,r^2} \\ \frac{b\,c\,d\,g\,(-2+p_l)\,p_l-4\,(b\,(c-d-g)+d\,g-c\,(d+g))\,p_l\,r^2+24\,(b+c-d-g)\,r^3+24\,r^4}{b\,c\,d\,g\,r^4} \\ \frac{4\,(6\,r\,(-g+r)+c\,(g\,p_l+6\,r)+b\,(-(c\,p_l)+g\,p_l+6\,r))}{d\,(b+d)\,(c+d)\,(d-g)\,r^2} \\ \frac{-4\,(6\,r\,(-d+r)+c\,(d\,p_l+6\,r)+b\,(-(c\,p_l)+d\,p_l+6\,r))}{(d-g)\,g\,(b+g)\,(c+g)\,r^2} \end{bmatrix} \begin{bmatrix} f(i-2) \\ f(i-1) \\ f(i) \\ f(i+1) \\ f(i+2) \end{bmatrix},$$

which form the components of a five-band-diagonal matrix. Note that in the case of a uniform grid where $b = d = \Delta r$ and $g = c = 2 * \Delta r$ the coefficients of say the ∂_r^2 operation are [$\frac{-1}{12\Delta r^2}$, $\frac{16}{12\Delta r^2}$, $\frac{-30}{12\Delta r^2}$, $\frac{16}{12\Delta r^2}$, $\frac{-1}{12\Delta r^2}$], the standard 5-point scheme defined in Cheney and Kincaid[62].

Clearly something else must be done near the origin where centered finite-differences are unusable. Ghost-point evaluation assumes nonexistent points can still maintain the centered finite difference algorithm and incorporate basic boundary conditions on the scalars at the origin. However it is numerically unstable in this geometry when the viscosity is small and the flow becomes turbulent.

The single value boundary conditions required on scalars at the origin correspond to conditions on the ℓ-dependent functions and their derivatives. Poloidal and toroidal scalars, S and T, satisfy $\mathrm{S}(0) = \mathrm{S}'(0) = \mathrm{S}''(0) = 0$ for $\ell \neq 1$, $\mathrm{S}(0) = \mathrm{S}''(0) = 0$ for$\ell = 1$, and $\mathrm{T}(0) = \mathrm{T}'(0) = \mathrm{T}''(0) = 0$ for all ℓ (derived in Appendix C). These boundary conditions used with forward finite-difference derivatives provide one solution to the origin problem. However, using forward finite differences with the same number of points as the second-order accurate centered finite differences are only first-order accurate. For laminar calculations, which are highly viscous, this mismatch in the finite-difference order does not create a problem with numerical stability or convergence. As Re is increased and the flow becomes turbulent the viscous damping at the origin is weak, and the more stringent requirement $\mathrm{S} = r^\ell$ and $\mathrm{T} = r^\ell$ is used at $r = 0$.

Appendix C: Boundary Conditions

The boundary conditions at the wall-vacuum interface and the origin are derived for the spectral scalars used in the Bullard-Gellman formulation. Using no-slip and solid wall boundaries for the flow and requiring a vacuum outside the wall determines the flow and magnetic field boundary conditions respectively. The regularity conditions are given by the requirement that the flow, vorticity, magnetic field, and current density are not multivalued at the origin.

Using the integral form of the imcompressibility condition, $\oint \mathbf{B} \cdot \boldsymbol{da} = 0$, applied to an area element on either side of the insulating boundary oriented outward from the sphere implies,

$$B_{r<} - B_{r>} = 0. \tag{C.1}$$

In the event of an applied field from an external source a nonzero source in the vacuum exists. By assuming the external currents producing the external magnetic field are far away and inalterable by the induced field $\mathbf{J} = 0$ for $r \geq a$, we know by E.1 Using Eqns. E.4 and E.2,

$$B_r = \sum_{\ell m} \frac{\ell(\ell+1)}{a} \mathrm{S}(r=a) Y_\ell^m = \sum_{\ell m} -\ell A_{\ell,m} a^{\ell-1} Y_\ell^m(\theta,\phi) + (\ell+1) \frac{B_{\ell m}}{a^{\ell+2}} Y_\ell^m(\theta,\phi). \tag{C.2}$$

Eq. C.2 implies a condition on the poloidal scalar potential,

$$\sum_{\ell m} \frac{\ell(\ell+1)}{a} \mathrm{S}(a) = \sum_{\ell m} -\ell A_{\ell,m} a^{\ell-1} + (\ell+1) \frac{B_{\ell m}}{a^{\ell+2}}. \tag{C.3}$$

The insulating wall, which permits no surface currents, provides another condition of the poloidal scalar since an Amperian loop running parallel around the surface of the sphere will enclose no net current. This implies B_θ and B_ϕ match the vacuum potential solution. Since B_θ and B_ϕ, noting $T = 0$ for $r > a$, are:

$$B_\theta = \sum_{\ell m} \frac{1}{r}\frac{\partial}{\partial r}(r\mathrm{S}(r))\frac{\partial}{\partial \theta}Y_\ell^m(\theta,\phi) = -\hat{\boldsymbol{\theta}}\cdot\boldsymbol{\nabla}\Phi \tag{C.4}$$

$$B_\phi = \sum_{\ell m} \frac{1}{r\sin\theta}\frac{\partial}{\partial r}(r\mathrm{S}(r))\frac{\partial}{\partial \phi}Y_\ell^m(\theta,\phi) = -\hat{\boldsymbol{\phi}}\cdot\boldsymbol{\nabla}\Phi \tag{C.5}$$

Where

$$-\hat{\boldsymbol{\theta}}\cdot\boldsymbol{\nabla}\Phi = -\frac{1}{r}\sum_{\ell m} A_{\ell,m}r^\ell\frac{\partial}{\partial\theta}Y_\ell^m + B_{\ell m}\frac{1}{r^{\ell+1}}\frac{\partial}{\partial\theta}Y_\ell^m \tag{C.6}$$

$$-\hat{\boldsymbol{\phi}}\cdot\boldsymbol{\nabla}\Phi = -\frac{1}{r\sin\theta}\sum_{\ell m} A_{\ell,m}r^\ell\frac{\partial}{\partial\phi}Y_\ell^m + B_{\ell m}\frac{1}{r^{\ell+1}}\frac{\partial}{\partial\phi}Y_\ell^m \tag{C.7}$$

Equating the expressions at $r = a$ and reducing, both components yield the same equation, namely:

$$\sum_{\ell m}\frac{\partial}{\partial r}(a\mathrm{S}(a)) = -\sum_{\ell m} A_{\ell,m}a^\ell + B_{\ell m}\frac{1}{a^\ell} \tag{C.8}$$

In the experiment, the externally applied magnetic field produced by a set of Helmholtz coils, thus giving the values of the coefficient $A_{\ell,m}$. The response field, produced by the advecting liquid metal, given by the coefficient $B_{\ell m}$ can be eliminated from the specification of the boundary condition on the poloidal scalar potential $P(r)|_{(r=a)}$, yielding:

$$a\frac{\partial P}{\partial r} + (\ell+1)P = -A_{\ell,m}a^\ell\frac{2\ell+1}{\ell+1}. \tag{C.9}$$

For instance, a uniform magnetic field applied oriented parallel to the axis of symmetry is given by:

$$\mathbf{B} = B_0\ \hat{\mathbf{z}} = B_0\big(\cos\theta\hat{\mathbf{r}} - \sin\theta\hat{\boldsymbol{\theta}}\big) \tag{C.10}$$

Which corresponds to a magnetic potential of the form:

$$\Phi = B_0 r\cos\theta = -B_0 r\frac{Y_1^0}{N_1^0} \tag{C.11}$$

where N_1^0 is a normalization factor. This gives a boundary condition of:

$$\left(r\frac{\partial P}{\partial r} + P\right)\Big|_{r=a} = \frac{3}{2}\frac{B_0}{N_1^0} \tag{C.12}$$

Let,

$$\mathbf{v} = \boldsymbol{\nabla} \times \boldsymbol{\nabla} \times \mathrm{s}\vec{\boldsymbol{r}} + \boldsymbol{\nabla} \times \mathrm{t}\vec{\boldsymbol{r}}, \tag{C.13}$$

$$\boldsymbol{\omega} = \boldsymbol{\nabla} \times \boldsymbol{\nabla} \times \Pi\vec{\boldsymbol{r}} + \boldsymbol{\nabla} \times \Theta\vec{\boldsymbol{r}}. \tag{C.14}$$

The components of $\mathbf{v}$ are

$$\begin{aligned}
\mathrm{v}_{\mathrm{s}r}(r,\theta,\phi) &= \frac{l\,(1+l)}{r}\,\mathrm{s}(r)\,Y_l^m & \mathrm{v}_{\mathrm{t}r}(r,\theta,\phi) &= 0 \\
\mathrm{v}_{\mathrm{s}\theta}(r,\theta,\phi) &= \frac{1}{r}\frac{\partial}{\partial r}(r\mathrm{s}(r))\frac{\partial}{\partial\theta}Y_l^m & \mathrm{v}_{\mathrm{t}\theta}(r,\theta,\phi) &= \frac{1}{\sin\theta}\mathrm{t}(r)\frac{\partial}{\partial\phi}Y_l^m \\
\mathrm{v}_{\mathrm{s}\phi}(r,\theta,\phi) &= \frac{1}{r\sin\theta}\frac{\partial}{\partial r}(r\mathrm{s}(r))\frac{\partial}{\partial\phi}Y_l^m & \mathrm{v}_{\mathrm{t}\phi}(r,\theta,\phi) &= -\mathrm{t}(r)\frac{\partial}{\partial\theta}Y_l^m
\end{aligned} \tag{C.15}$$

No slip boundary conditions are imposed on the velocity of the flow at the solid wall. A solid wall implies that the radial component of the flow must be zero which implies that

$$\mathrm{s}_{\ell,m}(r=a) = 0 \text{ for all } \ell \text{ and } m \tag{C.16}$$

The no-slip boundary condition implies that $\mathbf{v}_\theta = \mathbf{v}_\phi = 0$ thus using Eq. C.15 the conditions

$$\frac{\partial \mathrm{s}_{\ell,m}}{\partial r}\Big|_{(r=a)} = 0 \text{ and,} \tag{C.17}$$

$$\mathrm{t}_{\ell,m}(r=a) = 0 \text{ for all } \ell \text{ and } m, \tag{C.18}$$

must be satisfied.

The conditions on variables at the origin are defined so that the velocity, magnetic field, and the vorticity are not multivalued. The constraints are on real-space quantities and must be translated to conditions on spectral variables. Taylor expanding the velocity scalars, s and t near the origin and solving for their real-space counterparts [1].

$$\begin{aligned}
\mathrm{s} &= \mathrm{s}_0 + r\mathrm{s}_0' + \frac{r^2\,\mathrm{s}_0''}{2!} + \frac{r^3\,\mathrm{s}_0^{(3)}}{3!} + \frac{r^4\,\mathrm{s}_0^{(4)}}{4!} \\
\mathrm{t} &= \mathrm{t}_0 + r\,\mathrm{t}_0' + \frac{r^2\,\mathrm{t}_0''}{2} + \frac{r^3\,\mathrm{t}_0^{(3)}}{3!} + \frac{r^4\,\mathrm{t}_0^{(4)}}{4!}
\end{aligned} \tag{C.19}$$

[1] Note that $\mathbf{B}$ and $\mathbf{J}$ also follow the same rules at the origin.

Combining Eqns. C.19 and C.15 gives the expansion of the components of the flow near the origin. For example, with $\mathrm{s}_1^0 = \mathrm{s}(r){Y_1}^0 = \mathrm{s}(r)1/2\sqrt{3/\pi}\cos\theta$ and $\mathrm{t}_1^0 = \mathrm{t}(r){Y_1}^0 = \mathrm{t}(r)1/2\sqrt{3/\pi}\cos\theta$ the real-space spherical components of $\mathbf{V} = \boldsymbol{\nabla}\times\boldsymbol{\nabla}\times\mathrm{s}_1^0\vec{\boldsymbol{r}} + \boldsymbol{\nabla}\times\mathrm{t}_1^0\vec{\boldsymbol{r}}$ are:

$$
\begin{aligned}
\mathrm{V}_{sr} &= \frac{\sqrt{\frac{3}{\pi}}\,\mathrm{s}_0\,\cos\theta}{r} + \sqrt{\frac{3}{\pi}}\,\cos\theta\,\mathrm{s}_0' + \frac{\sqrt{\frac{3}{\pi}}\,r\,\cos\theta\,\mathrm{s}_0''}{2} + \frac{r^2\,\cos\theta\,\mathrm{s}_0^{(3)}}{2\sqrt{3\,\pi}} + \frac{r^3\,\cos\theta\,\mathrm{s}_0^{(4)}}{8\sqrt{3\,\pi}},\\
\mathrm{V}_{tr} &= 0,\\
\mathrm{V}_{s\theta} &= \frac{-\left(\sqrt{\frac{3}{\pi}}\,\mathrm{s}_0\,\sin\theta\right)}{2\,r} - \sqrt{\frac{3}{\pi}}\,\sin\theta\,\mathrm{s}_0'\frac{3\sqrt{\frac{3}{\pi}}\,r\,\sin\theta\,\mathrm{s}_0''}{4} - \frac{r^2\,\sin\theta\,\mathrm{s}_0^{(3)}}{\sqrt{3\,\pi}} - \frac{5\,r^3\,\sin\theta\,\mathrm{s}_0^{(4)}}{16\sqrt{3\,\pi}},\\
\mathrm{V}_{t\theta} &= 0,\\
\mathrm{V}_{s\phi} &= 0,\\
\mathrm{V}_{t\phi} &= \frac{\sqrt{\frac{3}{\pi}}\,\mathrm{t}_0\,\sin\theta}{2} + \frac{\sqrt{\frac{3}{\pi}}\,r\,\sin\theta\,\mathrm{t}_0'}{2} + \frac{\sqrt{\frac{3}{\pi}}\,r^2\,\sin\theta\,\mathrm{t}_0''}{4} + \frac{r^3\,\sin\theta\,\mathrm{t}_0^{(3)}}{4\sqrt{3\,\pi}} + \frac{r^4\,\sin\theta\,\mathrm{t}_0^{(4)}}{16\sqrt{3\,\pi}}.
\end{aligned}
$$

Projecting the spherical vectors into Cartesian components gives an expression for the conditions on the toroidal and poloidal scalars at the origin. The origin boundary condition is due to the fact that no Cartesian component can depend on the angles(θ,ϕ) or the vectors

will be multi-valued at the origin. The Cartesian components of the example flow, $\mathbf{V}$, are

$$\begin{aligned}
V_x &= \frac{\sqrt{\frac{3}{\pi}}\,\mathrm{s}_0\,\cos\theta\,\cos\phi\,\sin\theta}{2\,r} - \frac{\sqrt{\frac{3}{\pi}}\,\mathrm{t}_0\,\sin\theta\,\sin\phi}{2} - \frac{\sqrt{\frac{3}{\pi}}\,r\,\sin\theta\,\sin\phi\,\mathrm{t}_0'}{2} \\
&\quad - \frac{\sqrt{\frac{3}{\pi}}\,r\,\cos\theta\,\cos\phi\,\sin\theta\,\mathrm{s}_0''}{4} - \frac{\sqrt{\frac{3}{\pi}}\,r^2\,\sin\theta\,\sin\phi\,\mathrm{t}_0''}{4} - \frac{r^2\,\cos\theta\,\cos\phi\,\sin\theta\,\mathrm{s}_0^{(3)}}{2\sqrt{3\,\pi}} \\
&\quad - \frac{r^3\,\sin\theta\,\sin\phi\,\mathrm{t}_0^{(3)}}{4\sqrt{3\,\pi}} - \frac{\sqrt{\frac{3}{\pi}}\,r^3\,\cos\theta\,\cos\phi\,\sin\theta\,\mathrm{s}_0^{(4)}}{16} - \frac{r^4\,\sin\theta\,\sin\phi\,\mathrm{t}_0^{(4)}}{16\sqrt{3\,\pi}}. \\
V_y &= \frac{\sqrt{\frac{3}{\pi}}\,\mathrm{t}_0\,\cos\phi\,\sin\theta}{2} + \frac{\sqrt{\frac{3}{\pi}}\,\mathrm{s}_0\,\cos\theta\,\sin\theta\,\sin\phi}{2\,r} + \frac{\sqrt{\frac{3}{\pi}}\,r\,\cos\phi\,\sin\theta\,\mathrm{t}_0'}{2} \\
&\quad - \frac{\sqrt{\frac{3}{\pi}}\,r\,\cos\theta\,\sin\theta\,\sin\phi\,\mathrm{s}_0''}{4} + \frac{\sqrt{\frac{3}{\pi}}\,r^2\,\cos\phi\,\sin\theta\,\mathrm{t}_0''}{4} - \frac{r^2\,\cos\theta\,\sin\theta\,\sin\phi\,\mathrm{s}_0^{(3)}}{2\sqrt{3\,\pi}} \\
&\quad + \frac{r^3\,\cos\phi\,\sin\theta\,\mathrm{t}_0^{(3)}}{4\sqrt{3\,\pi}} - \frac{\sqrt{\frac{3}{\pi}}\,r^3\,\cos\theta\,\sin\theta\,\sin\phi\,\mathrm{s}_0^{(4)}}{16} + \frac{r^4\,\cos\phi\,\sin\theta\,\mathrm{t}_0^{(4)}}{16\sqrt{3\,\pi}}, \\
V_z &= \frac{3\sqrt{\frac{3}{\pi}}\,\mathrm{s}_0}{4\,r} + \frac{\sqrt{\frac{3}{\pi}}\,\mathrm{s}_0\,\cos 2\theta}{4\,r} + \sqrt{\frac{3}{\pi}}\,\mathrm{s}_0' + \frac{5\sqrt{\frac{3}{\pi}}\,r\,\mathrm{s}_0''}{8} - \frac{\sqrt{\frac{3}{\pi}}\,r\,\cos 2\theta\,\mathrm{s}_0''}{8} \\
&\quad + \frac{\sqrt{\frac{3}{\pi}}\,r^2\,\mathrm{s}_0^{(3)}}{4} - \frac{r^2\,\cos 2\theta\,\mathrm{s}_0^{(3)}}{4\sqrt{3\,\pi}} + \frac{7\,r^3\,\mathrm{s}_0^{(4)}}{32\sqrt{3\,\pi}} - \frac{\sqrt{\frac{3}{\pi}}\,r^3\,\cos 2\theta\,\mathrm{s}_0^{(4)}}{32}.
\end{aligned} \tag{C.20}$$

Terms of first order and above in r will be zero as $r \to 0$, however those terms in Eq. C.20 which contain an angular factor and are less than first order must be explicitly zeroed by boundary conditions on the radial functions and their derivatives. From above $\mathrm{s}_0,\ \mathrm{t}_0,\ \mathrm{t}_0' = 0$. Notice that the components in Eq. C.20 do not have factors of p_0' which is the term permitting flow through the origin.

Carrying out the same calculation with the vorticity using,

$$\begin{aligned}
\Pi &= \mathrm{t}, \\
\Theta &= -\nabla^2 \mathrm{s},
\end{aligned}$$

allows the real-space components of the vorticity to be expressed in terms of the streamfunctions of the flow:

$$\begin{aligned}
\boldsymbol{\omega}_{\mathbf{pr}}(r,\theta,\phi) &= \frac{l\,(1+l)}{r}\,t(r)\,Y_l^m, & \boldsymbol{\omega}_{\mathbf{tr}}(r,\theta,\phi) &= 0,\\
\boldsymbol{\omega}_{\mathbf{p\theta}}(r,\theta,\phi) &= \frac{1}{r}\frac{\partial}{\partial r}(rt(r))\frac{\partial}{\partial\theta}Y_l^m, & \boldsymbol{\omega}_{\mathbf{t\theta}}(r,\theta,\phi) &= -\frac{1}{\sin\theta}\nabla^2 p(r)\frac{\partial}{\partial\phi}Y_l^m,\\
\boldsymbol{\omega}_{\mathbf{p\phi}}(r,\theta,\phi) &= \frac{1}{r\sin\theta}\frac{\partial}{\partial r}(rt(r))\frac{\partial}{\partial\phi}Y_l^m, & \boldsymbol{\omega}_{\mathbf{t\phi}}(r,\theta,\phi) &= \nabla^2 p(r)\frac{\partial}{\partial\theta}Y_l^m.
\end{aligned}$$

Converting these components to Cartesian geometry and using the example flow $\mathbf{V}$ gives,

$$\begin{aligned}
\boldsymbol{\omega}_{\mathbf{X}} &= \frac{\sqrt{\frac{3}{\pi}}\,\mathrm{t}_0\,\cos(\theta)\,\cos(\phi)\,\sin(\theta)}{2\,r} - \frac{\sqrt{\frac{3}{\pi}}\,p_0\,\sin(\theta)\,\sin(\phi)}{r^2} + \sqrt{\frac{3}{\pi}}\,\sin(\theta)\,\sin(\phi)\,p_0''\\
&\quad - \frac{\sqrt{\frac{3}{\pi}}\,r\,\cos(\theta)\,\cos(\phi)\,\sin(\theta)\,\mathrm{t}_0''}{4} + \frac{5\,r\,\sin(\theta)\,\sin(\phi)\,p_0^{(3)}}{2\sqrt{3\,\pi}} - \frac{r^2\,\cos(\theta)\,\cos(\phi)\,\sin(\theta)\,\mathrm{t}_0^{(3)}}{2\sqrt{3\,\pi}}\\
&\quad + \frac{3\sqrt{\frac{3}{\pi}}\,r^2\,\sin(\theta)\,\sin(\phi)\,p_0^{(4)}}{8} - \frac{\sqrt{\frac{3}{\pi}}\,r^3\,\cos(\theta)\,\cos(\phi)\,\sin(\theta)\,\mathrm{t}_0^{(4)}}{16}\\
\boldsymbol{\omega}_{\mathbf{Y}} &= \frac{\sqrt{\frac{3}{\pi}}\,p_0\,\cos(\phi)\,\sin(\theta)}{r^2} + \frac{\sqrt{\frac{3}{\pi}}\,\mathrm{t}_0\,\cos(\theta)\,\sin(\theta)\,\sin(\phi)}{2\,r} - \sqrt{\frac{3}{\pi}}\,\cos(\phi)\,\sin(\theta)\,p_0''\\
&\quad - \frac{\sqrt{\frac{3}{\pi}}\,r\,\cos(\theta)\,\sin(\theta)\,\sin(\phi)\,\mathrm{t}_0''}{4} - \frac{5\,r\,\cos(\phi)\,\sin(\theta)\,p_0^{(3)}}{2\sqrt{3\,\pi}} - \frac{r^2\,\cos(\theta)\,\sin(\theta)\,\sin(\phi)\,\mathrm{t}_0^{(3)}}{2\sqrt{3\,\pi}}\\
&\quad - \frac{3\sqrt{\frac{3}{\pi}}\,r^2\,\cos(\phi)\,\sin(\theta)\,p_0\mathrm{t}_0^{(4)}}{8} - \frac{\sqrt{\frac{3}{\pi}}\,r^3\,\cos(\theta)\,\sin(\theta)\,\sin(\phi)\,\mathrm{t}_0^{(4)}}{16}\\
\boldsymbol{\omega}_{\mathbf{Z}} &= \frac{3\sqrt{\frac{3}{\pi}}\,\mathrm{t}_0}{4\,r} + \frac{\sqrt{\frac{3}{\pi}}\,\mathrm{t}_0\,\cos(2\,\theta)}{4\,r} + \sqrt{\frac{3}{\pi}}\,\mathrm{t}_0' + \frac{5\sqrt{\frac{3}{\pi}}\,r\,\mathrm{t}_0''}{8} - \frac{\sqrt{\frac{3}{\pi}}\,r\,\cos(2\,\theta)\,\mathrm{t}_0''}{8}\\
&\quad + \frac{\sqrt{\frac{3}{\pi}}\,r^2\,\mathrm{t}_0^{(3)}}{4} - \frac{r^2\,\cos(2\,\theta)\,\mathrm{t}_0^{(3)}}{4\sqrt{3\,\pi}} + \frac{7\,r^3\,\mathrm{t}_0^{(4)}}{32\sqrt{3\,\pi}} - \frac{\sqrt{\frac{3}{\pi}}\,r^3\,\cos(2\,\theta)\,\mathrm{t}_0^{(4)}}{32}
\end{aligned}$$

From these equations it is clear that more terms must be explicitly zeroed at the origin. Table C.1 shows, through the above analysis, which terms must be eliminated for all harmonics. The requirement that r^ℓ be an eigenfunction of the decay problem near the origin (see Appendix F) gives the general boundary condition that $\mathbf{v}$ and $\mathbf{B}$ be at least $\mathcal{O}(r^\ell)$ as $r \to 0$.

Table C.1 The conditions on variables at the origin

$Y_l^m(\theta,\phi)$	$\mathbf{r_x}, \mathbf{v_y} \rightarrow$	$\mathbf{v_z} \rightarrow$	$\boldsymbol{\omega_x}, \boldsymbol{\omega_y} \rightarrow$	$\boldsymbol{\omega_z} \rightarrow$
Y_1^0	$p_0, \mathrm{t}_0 = 0,\ p_0' \neq 0$	$p_0 = 0,\ p_0' \neq 0$	$p_0'' = 0$	$\mathrm{t}_0' \neq 0$
$Y_1^{\pm 1}$	$p_0, \mathrm{t}_0 = 0,\ p_0' \neq 0$	$p_0, \mathrm{t}_0 = 0$	$p_0, \mathrm{t}_0, p_0'' = 0,\ p_0' \neq 0$	$p_0, \mathrm{t}_0, p_0'' = 0$
Y_2^0	$p_0, \mathrm{t}_0, p_0' = 0$	$p_0, p_0' = 0$	$p_0, \mathrm{t}_0, \mathrm{t}_0', p_0'' = 0$	$\mathrm{t}_0, \mathrm{t}_0' = 0$
$Y_2^{\pm 1}$	$p_0, \mathrm{t}_0, p_0' = 0$	$p_0, \mathrm{t}_0, p_0' = 0$	$p_0, \mathrm{t}_0, \mathrm{t}_0', p_0'' = 0$	$p_0, \mathrm{t}_0, \mathrm{t}_0', p_0'' = 0$
$Y_2^{\pm 2}$	$p_0, \mathrm{t}_0, p_0' = 0$	$p_0, \mathrm{t}_0, p_0' = 0$	$p_0, \mathrm{t}_0, \mathrm{t}_0', p_0'' = 0$	$\mathrm{t}_0, \mathrm{t}_0', p_0'' = 0$
Y_3^0	$p_0, \mathrm{t}_0, p_0' = 0$	$p_0, p_0' = 0$	$p_0, \mathrm{t}_0, \mathrm{t}_0', p_0'' = 0$	$\mathrm{t}_0, \mathrm{t}_0' = 0$
$Y_3^{\pm 1}$	$p_0, \mathrm{t}_0, p_0' = 0$	$p_0, \mathrm{t}_0, p_0' = 0$	$p_0, \mathrm{t}_0, \mathrm{t}_0', p_0'' = 0$	$p_0, \mathrm{t}_0, \mathrm{t}_0', p_0'' = 0$
$Y_3^{\pm 2}$	$p_0, \mathrm{t}_0, p_0' = 0$	$p_0, \mathrm{t}_0, p_0' = 0$	$p_0, \mathrm{t}_0, \mathrm{t}_0', p_0'' = 0$	$p_0, \mathrm{t}_0, \mathrm{t}_0', p_0'' = 0$
$Y_3^{\pm 3}$	$p_0, \mathrm{t}_0, p_0' = 0$	$p_0, \mathrm{t}_0, p_0' = 0$	$p_0, \mathrm{t}_0, \mathrm{t}_0', p_0'' = 0$	$p_0, \mathrm{t}_0, \mathrm{t}_0', p_0'' = 0$
Y_4^0	$p_0, \mathrm{t}_0, p_0' = 0$	$p_0, p_0' = 0$	$p_0, \mathrm{t}_0, \mathrm{t}_0', p_0'' = 0$	$\mathrm{t}_0, \mathrm{t}_0' = 0$
$Y_4^{\pm 1}$	$p_0, \mathrm{t}_0, p_0' = 0$	$p_0, \mathrm{t}_0, p_0' = 0$	$p_0, \mathrm{t}_0, \mathrm{t}_0', p_0'' = 0$	$p_0, \mathrm{t}_0, \mathrm{t}_0', p_0'' = 0$
$Y_4^{\pm 2}$	$p_0, \mathrm{t}_0, p_0' = 0$	$p_0, \mathrm{t}_0, p_0' = 0$	$p_0, \mathrm{t}_0, \mathrm{t}_0', p_0'' = 0$	$p_0, \mathrm{t}_0, \mathrm{t}_0', p_0'' = 0$
$Y_4^{\pm 3}$	$p_0, \mathrm{t}_0, p_0' = 0$	$p_0, \mathrm{t}_0, p_0' = 0$	$p_0, \mathrm{t}_0, \mathrm{t}_0', p_0'' = 0$	$p_0, \mathrm{t}_0, \mathrm{t}_0', p_0'' = 0$
$Y_4^{\pm 4}$	$p_0, \mathrm{t}_0, p_0' = 0$	$p_0, \mathrm{t}_0, p_0' = 0$	$p_0, \mathrm{t}_0, \mathrm{t}_0', p_0'' = 0$	$p_0, \mathrm{t}_0, \mathrm{t}_0', p_0'' = 0$
$Y_l^0, l \neq 1$	$p_0, \mathrm{t}_0, p_0' = 0$	$p_0, p_0' = 0$	$p_0, \mathrm{t}_0, \mathrm{t}_0', p_0'' = 0$	$\mathrm{t}_0, \mathrm{t}_0' = 0$
$Y_l^{\pm n}\ n, l \neq 1$	$p_0, \mathrm{t}_0, p_0' = 0$	$p_0, \mathrm{t}_0, p_0' = 0$	$p_0, \mathrm{t}_0, \mathrm{t}_0', p_0'' = 0$	$p_0, \mathrm{t}_0, \mathrm{t}_0', p_0'' = 0$

The above analysis shows the same boundary conditions can be used for all $l \neq 1$,

$$p_0,\ \mathrm{t}_0,\ p_0',\ \mathrm{t}_0',\ p_0'' \ = 0 \qquad for\ l\ \neq\ 1 \tag{C.21}$$

$$p_0,\ \mathrm{t}_0,\ \mathrm{t}_0',\ p_0'' \ = 0 \qquad for\ l\ =\ 1 \tag{C.22}$$

Appendix D: Calculating the Electric Potential and Field

The components of Ohm's law provide insight into the generation of turbulent EMF's, but the electric field and electrostatic potential must be computed from the evolved variables. This chapter discusses how the electric field and electric potential are calculated from the scalar functions used in the Bullard-Gellman representation. The gauge choice for the system is discussed as are the boundary conditions on the electrostatic potential.

To compute the electric field and the potential some discussion of gauge choice is warranted. In the Bullard-Gellman representation, the magnetic vector potential is:

$$\mathbf{A} = \boldsymbol{\nabla} \times P\vec{\boldsymbol{r}} + T\vec{\boldsymbol{r}} \tag{D.1}$$

However, $\mathbf{A}$ is not explicitly calculated, only its curl, by gauge invariance, the vector potential $\mathbf{A'}$ could be defined as:

$$\mathbf{A'} = \boldsymbol{\nabla} \times P\vec{\boldsymbol{r}} + T\hat{\boldsymbol{r}} - \boldsymbol{\nabla}\lambda \tag{D.2}$$

In this representation the Coulomb gauge could be chosen so that $\boldsymbol{\nabla} \cdot \mathbf{A}' = 0$ which would require

$$-\boldsymbol{\nabla}^2\lambda = \boldsymbol{\nabla} \cdot \mathbf{A} = \boldsymbol{\nabla} \cdot (T\vec{\boldsymbol{r}}) = 3T + \vec{\boldsymbol{r}} \cdot \boldsymbol{\nabla}T \tag{D.3}$$

This ensures that $\mathbf{A'}$ is divergence free, the computation of the electric field from $\mathbf{A}$, λ, and Φ would be complicated since $\lambda = [\nabla^2]^{-1}[\boldsymbol{\nabla} \cdot \mathbf{A}]$ and there are no clear boundary condition on λ.

Starting with Eq. A.22 the electric potential is computed by employing Helmholtz's theorum to express the electric field in terms of $\mathbf{A}$ and $\boldsymbol{\nabla}\Phi$:

$$\mathbf{E} = -\frac{\partial \mathbf{A}}{\partial t} - \boldsymbol{\nabla}\Phi = -Rm(\mathbf{v} \times \mathbf{B}) + \mathbf{J}. \tag{D.4}$$

Taking the divergence of Eq. D.4, noting $\boldsymbol{\nabla} \cdot \mathbf{J} = 0$:

$$\nabla^2\Phi = Rm\boldsymbol{\nabla} \cdot (\mathbf{v} \times \mathbf{B}) - \frac{\partial(\boldsymbol{\nabla} \cdot \mathbf{A})}{\partial t}. \tag{D.5}$$

The results of Eq. D.3 are substituted into Eq. D.5 so that

$$\nabla^2\Phi = Rm\boldsymbol{\nabla}\cdot(\mathbf{v}\times\mathbf{B}) - \frac{\partial(3T + rT')}{\partial t} \tag{D.6}$$

Letting $\mathbf{F} = \mathbf{v}\times\mathbf{B}$, and multiplying Eq. D.5 by r:

$$r\nabla^2\Phi = r\boldsymbol{\nabla}\cdot\mathbf{F} = \frac{1}{r}\frac{\partial}{\partial r}(r^2F_r) + \frac{1}{\sin\theta}\frac{\partial}{\partial\theta}(\sin\theta F_\theta) + \frac{1}{\sin\theta}\frac{\partial F_\phi}{\partial\phi} \tag{D.7}$$

Projecting, Eq. E.2 into spherical harmonics and using the following definitions for the components of $\mathbf{F}$ gives an expression for the scalar potential:

$$p*_{\ell m} = \frac{rF_{r,\ell m}}{\ell(\ell+1)} \tag{D.8}$$

$$\Xi_{lm} = -\frac{1}{\ell(\ell+1)}\left[\frac{1}{\sin\theta}\frac{\partial}{\partial\theta}(\sin\theta F_{\theta,\ell m}) + \frac{1}{\sin\theta}\frac{\partial F_{\phi,\ell m}}{\partial\phi}\right] \tag{D.9}$$

Using these definitions, the Poisson equation for the potential is

$$\nabla^2\Phi_{\ell,m} = \frac{\ell(\ell+1)}{r^2}\frac{\partial}{\partial r}\left(rp^*_{\ell,m}\right) - \frac{\ell(\ell+1)}{r}\Xi_{\ell,m} - \frac{\partial}{\partial t}\left(3T_{\ell,m} + rT'_{\ell,m}\right). \tag{D.10}$$

The code tracks all of the quantities in Eq. D.10 as part of the time-advance thus Eq. D.10 is the desirable expression for the electric potential. To invert this expression the radial boundary conditions on Φ are needed. Choosing the reference point for calculation of the potential to be at the origin of the sphere, let $\Phi(r=0) = 0$. Starting with Eq. A.22, and taking the divergence,

$$\boldsymbol{\nabla}\cdot\mathbf{E} = -Rm\boldsymbol{\nabla}\cdot(\mathbf{v}\times\mathbf{B}) + \boldsymbol{\nabla}\cdot\mathbf{J} = -Rm\boldsymbol{\nabla}\cdot(\mathbf{v}\times\mathbf{B}), \tag{D.11}$$

and integrating over the conducting region

$$\oint d\boldsymbol{\tau}\ \boldsymbol{\nabla}\cdot\mathbf{E} = -Rm\oint d\boldsymbol{\tau}\ \boldsymbol{\nabla}\cdot(\mathbf{v}\times\mathbf{B}). \tag{D.12}$$

Using divergence theorum, and substituting Helmholtz's theorum,

$$\oint d\Omega\ \boldsymbol{\nabla}\Phi\cdot\hat{\boldsymbol{r}} = \oint d\Omega\ \hat{\boldsymbol{r}}\cdot(\mathbf{v}\times\mathbf{B}) - \frac{\partial}{\partial t}\oint d\Omega\ \hat{\boldsymbol{r}}\cdot\mathbf{A}. \tag{D.13}$$

Equating the integrands noting that these terms are evaluated at the vacuum interface gives

$$\frac{\partial \Phi(r=a)}{\partial r} = \left[\mathbf{B}\cdot(\hat{\boldsymbol{r}}\times\mathbf{v})\right]_{r=a} - \hat{\boldsymbol{r}}\cdot\left[\boldsymbol{\nabla}\times \mathrm{S}\vec{\boldsymbol{r}} + \mathrm{T}\vec{\boldsymbol{r}}\right]_{r=a}. \tag{D.14}$$

The flow satisfies the no-slip, solid-wall boundary condition so that $\mathbf{v}=0$ at $r=a$. From Appendix C, $T(r=a)=0$ and $\boldsymbol{\nabla}\times P\vec{\boldsymbol{r}}$ is perpendicular to $\hat{\boldsymbol{r}}$ so the boundary condition on the electric potential is:

$$\frac{\partial \Phi(r=a)}{\partial r} = 0. \tag{D.15}$$

The potential is solved with

$$\begin{aligned} \Phi = \{\nabla^2\}^{-1}\left[Rm\boldsymbol{\nabla}\cdot(\mathbf{v}\times\mathbf{B}) - \frac{\partial(3T+rT')}{\partial t}\right] \text{ subject to} \\ \Phi(r=0)=0 \\ \Phi'(r=a)=0 \end{aligned} \tag{D.16}$$

The electric field is also straightforward to calculate using $\mathbf{A}$ from the field advance and Φ from the post-processing inversion.

Appendix E: Calculating the Vacuum Magnetic Field Contribution to Power Balance

Since the balance of power is computed to monitor the transfer of energy between the flow and the magnetic field. The contribution to the total magnetic energy density from the open magnetic field lines extending outside the conducting region is calculated. It is presented here to show that all magnetic energy density is accounted for in the power calculation.

In simply connected current free regions:

$$\mathbf{B} = -\nabla\Phi \tag{E.1}$$

where Φ can be expressed as:

$$\Phi \ = \sum_{\ell,m} \frac{A_{\ell,m}}{r^{\ell+1}} Y_{\ell,m}(\theta,\phi) + B_{\ell,m} Y_{\ell,m} r^{\ell} \tag{E.2}$$

since $\Phi \propto r^l$ terms diverge as $r \to \infty$

At the wall, imcompressibility requires $[\mathbf{B_r}] = \mathbf{0}$. Equating the potential, Eq. E.2 with the magnetic field at the wall:

$$B_r \Big|_{r=a} \ = \ -\frac{\partial \Phi}{\partial r} \Big|_{r=a}. \tag{E.3}$$

Since

$$B_r \ = \ \frac{\ell(\ell+1)}{r} \mathrm{S}(r) Y_{\ell,m}(\theta,\phi), \tag{E.4}$$

combining (E.2) and (E.4) at (r=a) yields:

$$-\frac{\partial}{\partial r} \sum_{\ell,m} \frac{A_{\ell,m}}{r^{\ell+1}} Y_{\ell,m}(\theta,\phi) \Big|_{r=a} \ = \ \sum_{\ell,m} \frac{\ell(\ell+1)}{r} \mathrm{S}(r) Y_{\ell,m}(\theta,\phi) \Big|_{r=a}. \tag{E.5}$$

With some reduction:

$$\sum_{\ell,m} \frac{A_{\ell,m}\ (\ell+1)}{a^{\ell+2}} Y_{\ell,m}(\theta,\phi) \ = \ \sum_{\ell,m} \frac{\ell(\ell+1)}{a} \mathrm{S}(a) Y_{\ell,m}(\theta,\phi) \tag{E.6}$$

Solving Eq. E.6,

$$A_{\ell,m} \ = \ \ell a^{\ell+1} \mathrm{S}(a). \tag{E.7}$$

From Eq. E.2,

$$\Phi \;=\; \sum_{\ell,m} \frac{\ell a^{\ell+1} \mathrm{S}(a)}{r^{\ell+1}} Y_{\ell,m}(\theta,\phi). \tag{E.8}$$

To calculate the vacuum energy, $1/2B^2$ for $r > a$ must be calculated which is,

$$\int_a^\infty \int_0^{2\pi} \int_0^{\frac{\pi}{2}} r^2 \sin\theta \; dr \; d\theta \; d\phi \; [\frac{1}{2}B^2] \;=\; \frac{1}{2} \int_a^\infty \int_0^{2\pi} \int_0^{\frac{\pi}{2}} \mathrm{d}\tau \; [-\nabla\Phi]^2. \tag{E.9}$$

Let

$$\frac{1}{r}\nabla^*\Phi \;\equiv\; \frac{1}{r}\frac{\partial\Phi}{\partial\theta}\hat{\theta} \;+\; \frac{1}{r\sin\theta}\frac{\partial\Phi}{\partial\phi}\hat{\phi} \tag{E.10}$$

and evaluate the LHS of Eq. E.9 :

$$LHS = \frac{1}{2} \int_a^\infty \int_0^{2\pi} \int_0^{\frac{\pi}{2}} \mathrm{d}\tau \big[-\frac{\partial\Phi}{\partial r}\big]^2 \;+\; \frac{1}{2} \int_a^\infty \int_0^{2\pi} \int_0^{\frac{\pi}{2}} \mathrm{d}\tau \; \big[-\frac{1}{r}\nabla^*\Phi\big]^2 \tag{E.11}$$

Chandrasekhar [63] derives the integral of $(\nabla^* Y_{\ell,m}) \cdot (\nabla^* Y_{\ell'}^{m'})$:

$$\int\int \sin\theta \; d\theta \; d\phi (\nabla^* Y_{\ell,m}) \cdot (\nabla^* Y_{\ell'}^{m'}) \;=\; \ell(\ell+1) N_{\ell,m} \delta_{\ell\ell'} \delta_{mm'} \tag{E.12}$$

where

$$N_\ell^m \;=\; (2\ell+1)\frac{(\ell+m)!}{(\ell-m)!} \; (\times\, 2 \text{ when } m \neq 0). \tag{E.13}$$

Using Eq. E.12

$$\int_a^\infty \int_0^{2\pi} \int_0^{\frac{\pi}{2}} \mathrm{d}\tau \; \big[-\frac{1}{r}\nabla^*\Phi\big]^2 = \sum_{\ell,m} \ell(\ell+1) A_{\ell,m}^2 N_{\ell,m} \int_a^\infty dr \frac{r^2}{(r^{\ell+2})^2} \tag{E.14}$$

The first term in Eq. E.11 is

$$\int_a^\infty \int_0^{2\pi} \int_0^{\frac{\pi}{2}} \mathrm{d}\tau \Big[-\frac{\partial\Phi}{\partial r}\Big]^2 = \sum_{\ell,m} \int_a^\infty \int_0^{2\pi} \int_0^{\frac{\pi}{2}} \mathrm{d}\tau \Big[-\frac{\partial}{\partial r}\Big(\frac{A_{\ell,m}}{r^{\ell+1}} Y_{\ell,m}(\theta,\phi)\Big)\Big]^2 \tag{E.15}$$

$$\int_a^\infty \int_0^{2\pi} \int_0^{\frac{\pi}{2}} \mathrm{d}\tau \Big[-\frac{\partial\Phi}{\partial r}\Big]^2 = \sum_{\ell,m} (\ell+1)^2 A_{\ell,m}^2 \int_a^\infty \frac{dr}{r^{2\ell+2}} \;=\; A_{\ell,m}^2 \frac{(\ell+1)^2}{(2\ell+1)a^{2\ell+1}} \tag{E.16}$$

Combining the results gives:

$$\int_a^\infty \int_0^{2\pi} \int_0^{\frac{\pi}{2}} \mathrm{d}\tau \big[\frac{1}{2}B^2\big] = \;\; \frac{A_{\ell,m}^2}{2} N_{\ell,m} \big[\frac{(\ell+1)^2}{(2\ell+1)a^{2\ell+1}} + \frac{\ell(\ell+1)}{(2\ell+1)\; a^{2\ell+1}}\Big] \tag{E.17}$$

Integrating over space, $1/2B^2$ in the vacuum is:

$$\frac{1}{2}B^2 \;=\; \frac{\ell^2(P(r=a))^2}{2\ell+1}\Big[(\ell+1)^2+\ell(\ell+1)\Big] \text{ where } a=1. \tag{E.18}$$

Simplifying Eq. E.18

$$\frac{1}{2}B^2 \;=\; [P(1)]^2\;\ell^2(\ell+1),\; \text{for } r\geq a \tag{E.19}$$

Appendix F: Decay Modes

A simple analytic result for the purposes of benchmarking the evolution of the diffusion equation for the magnetic spectral scalar functions used in the Bullard-Gellman representation is presented. The diffusion equation is solved in spherical coordinates using a product of coordinate-separated variables and the decay modes are given by applying the magnetic boundary conditions to the separated product.

The decay modes of the magnetic diffusion equations for the poloidal and toroidal flux functions are computed by solving

$$-\lambda_{\mathrm{S}}\mathrm{S}(r,\theta,\phi,t) = \nabla^2\mathrm{S}(r,\theta,\phi,t), \tag{F.1}$$

$$-\lambda_{\mathrm{T}}\mathrm{T}(r,\theta,\phi,t) = \nabla^2\mathrm{T}(r,\theta,\phi,t), \tag{F.2}$$

for λ_{S} and λ_{T}.

To find λ_{S}, let $\mathrm{S} = R_{\ell,m}(r)Y_{\ell,m}$, then Eq. F.1 is

$$\lambda_{\mathrm{S}}\mathrm{S} = \frac{1}{r}\frac{d^2}{dr^2}(rR_{\ell,m})Y_{\ell,m} - \frac{\ell(\ell+1)}{r^2}R_{\ell,m}Y_{\ell,m}. \tag{F.3}$$

Cancelling factors common to both sides of Eq. F.3, expanding the derivatives, and dropping the harmonic index, yields

$$-\lambda R = \frac{1}{r}\frac{d}{dr}(2R' + rR'') - \frac{\ell}{r^2}R. \tag{F.4}$$

Eq. F.4 is multiplied by r^2 so that

$$r^2\frac{d^2R}{dr^2} + 2\frac{dR}{dr} + (\lambda r^2 - \ell)R = 0. \tag{F.5}$$

Knowing that Bessel functions are the radial eigenfunctions of the diffusion operator the equation for $R(r)$ is expected to reduce to a Bessel function. Letting

$$x \equiv \sqrt{\lambda}r \;\rightarrow\; \frac{d}{dr} = \frac{dx}{dr}\frac{d}{dx}, \tag{F.6}$$

Eq. F.5 can be written as

$$x^2R'' + 2xR' + (x^2 - \ell(\ell+1))R = 0 \text{ where } ' \text{ denotes } \frac{d}{dx}. \tag{F.7}$$

Looking for solutions of the form $R(x) = \kappa(x)x^{-\frac{1}{2}}$ Eq. F.7 can be evaluated term by term:

$$R'(x) = \kappa' x^{-1/2} - \frac{1}{2}\kappa x^{-3/2} \tag{F.8}$$

$$R''(x) = \frac{d}{dx}\left(\kappa' x^{-1/2} - \frac{1}{2}\kappa x^{-3/2}\right) = \kappa'' x^{-1/2} - \kappa' x^{-3/2} + \frac{3}{4}\kappa x^{-5/2} \tag{F.9}$$

Substituting this result into Eq. F.7 gives

$$x^2\left[\kappa'' - \kappa' x^{-1} + \frac{3}{4}\kappa x^{-2}\right] + 2x\left[\kappa' - \frac{1}{2}\kappa x^{-1}\right] + \left[x^2 - \ell^2 - \ell\right]\kappa = 0. \tag{F.10}$$

This reduces to:

$$x^2\kappa'' + x\kappa' + \left(x^2 - (\ell + \frac{1}{2})^2\right)\kappa = 0 \tag{F.11}$$

Letting $\xi \equiv \ell + \frac{1}{2}$, Eq. F.11 becomes:

$$x^2\kappa'' + x\kappa' + (x - \xi^2)\kappa = 0 \tag{F.12}$$

The solutions of this equation define the Bessel functions [56] which are of the form:

$$\kappa = A_\xi \mathrm{J}_\xi(x) + B_\xi Y_\xi(x). \tag{F.13}$$

Using Eq. **??**,

$$R(x) = \frac{A_\xi \mathrm{J}_\xi(x)}{x^{1/2}} + \frac{B_\xi Y_\xi(x)}{x^{1/2}}. \tag{F.14}$$

The spherical Bessel functions of the first kind are defined by

$$\mathrm{j}_\ell \equiv \sqrt{\frac{\pi}{2}}\frac{\mathrm{J}_{\ell+\frac{1}{2}}(x)}{\sqrt{x}}, \tag{F.15}$$

$$n_\ell \equiv \sqrt{\frac{\pi}{2}}\frac{Y_{\ell+\frac{1}{2}}(x)}{\sqrt{x}}. \tag{F.16}$$

From the conditions derived in Appendix: C, the magnetic poloidal scalar as the origin is approached must be zero or at least finite. This requires $B_\xi = 0$ in Eq F.14 The boundary condition on S at the wall is

$$\left[\frac{dP}{dr} + \frac{\ell+1}{r}P\right]_{r=a} = 0. \tag{F.17}$$

Using the definition of $R(x)$, Eq. F.17 can then be recast as an expression for R so that

$$\sqrt{\lambda}\left(\frac{dR}{dx} + \frac{\ell+1}{x}R\right) = 0 \text{ where } R = A'_\xi\frac{\mathrm{J}_\xi(x)}{x^{1/2}}. \tag{F.18}$$

The boundary condition, Eq. F.18, reduces to

$$\mathrm{J}'_\xi(x) + \frac{\ell}{x}\mathrm{J}_\xi(x) + \frac{1}{2}\frac{\mathrm{J}_\xi(x)}{x} = 0. \tag{F.19}$$

Using a recursive identity for derivatives of the Bessel functions,

$$x\mathrm{J}'_{\ell+\frac{1}{2}}(x) = x\mathrm{J}_{\ell-\frac{1}{2}} - \left(\ell + \frac{1}{2}\right)\mathrm{J}_{\ell+\frac{1}{2}}(x), \tag{F.20}$$

gives

$$\mathrm{J}'_\xi(x) + \frac{\ell}{x}\mathrm{J}_\xi(x) + \frac{1}{2}\frac{\mathrm{J}_\xi(x)}{x} = x\mathrm{J}_{\ell-\frac{1}{2}}(x) - \frac{1}{2}\frac{\mathrm{J}_{\ell+\frac{1}{2}}(x)}{x} + \frac{1}{2}\frac{\mathrm{J}_{\ell-\frac{1}{2}}(x)}{x} = 0. \tag{F.21}$$

Provided that $\mathrm{J}_{\ell-\frac{1}{2}}(x) = 0$ the boundary condition Eq. F.18 is satisfied. Thus x must denote the zeros of the Bessel functions of half-integer order. Noting the definition of x the expression for the analytic decay rates of the poloidal field is

$$\lambda_\ell = \frac{x_\ell^2}{a^2}. \tag{F.22}$$

Solving Eq. F.2 for λ_T is straightforward using the same process as the poloidal field. The result is an equation whose solutions are spherical bessel functions multiplied by an exponentially decaying temporal factor:

$$\mathrm{T} = \mathrm{T}(r)Y_{\ell,m}e^{-\lambda t} \text{ where } T(r) = C'\frac{J_{\ell+1/2}(x)}{x^{1/2}} \tag{F.23}$$

The only difference is the application of the external toroidal boundary condition - $\mathrm{T}_{\ell,m} = 0$ implies that rather than $\mathrm{J}_{\ell-\frac{1}{2}}(x) = 0$ as for the poloidal field:

$$T(r) = C'\frac{J_{\ell+1/2}(x)}{x^{1/2}} = 0 \;\rightarrow\; J_{\ell+1/2}(x) = 0 \tag{F.24}$$

Since the toroidal flow scalar, from Appendix C must also be zero at the wall due to the no-slip boundary condition, its decay modes will also match the decay modes of the toroidal magnetic scalar.